Non-photochemical Laser-Induced Nucleation of KCl from Aqueous solutions in a Droplet-Based Microfluidic System

Vincent J. de Munck

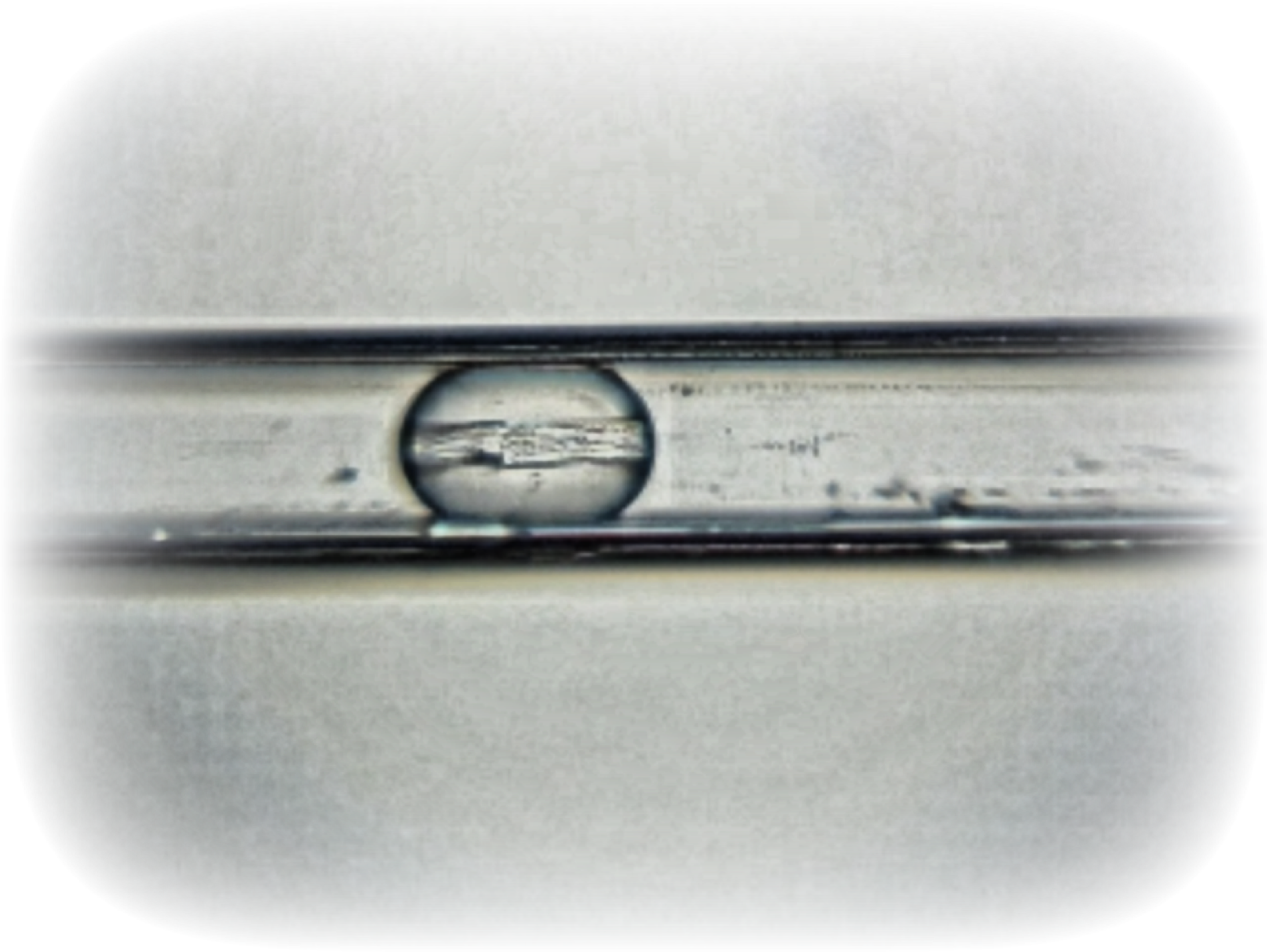

TU Delft
Delft University of Technology

Challenge the future

Non-Photochemical Laser-Induced Nucleation of KCl from Aqueous Solutions in a Droplet-Based Microfluidic System

Vincent J. de Munck
4490576

MSc Chemical Engineering
ChemE - Faculty of Applied Sciences & 3ME - Process & Energy Department
Delft University of Technology

In partial fulfillment of the requirements for the degree of
Master of Science
in Chemical Engineering

Author	Study nr.
Vincent J. de Munck	4490576
Supervisors	
Dr. H.B. Eral	Tu Delft
Dr. F. Marques Penha	KTH Royal Institute of Technology
Thesis commitee	
Dr. H.B. Eral	Tu Delft
Prof. Dr. A.E.D.M. van der Heijden	Tu Delft
Dr. Ir. G.M.H. Meesters	Tu Delft

Keywords: Non-Photochemical laser induced nucleation, NPLIN, Laser, Nucleation, Crystallization, Process intensification

Assignment issued: 07-09-2020
Report issued: 04-05-2021
Appraisal: 18-05-2021

Abstract

Crystallization is one of the most widely used purification and separation processes. Nevertheless, the initial step of the crystallization process, nucleation, is still poorly understood and highly stochastic. As a result, most crystallization processes lack fine control over the produced crystal properties. Non-photochemical Laser Induced Nucleation is seen as a promising technique to optimize crystallization processes, by decreasing the induction time and potentially offering more control over crystal size, amount and morphology. However, as its underlying mechanism has not yet been unveiled its application is still limited. Further study of the phenomenon is thus essential, yet limited by the stochastic nature of the process. Past research has been laborious and time-consuming, due to the substantial number of samples needed to attain statistical significance of the results. Microfluidics could offer a solution to this issue, since it allows for the study of copious amounts of independent samples in short time frames, whilst using less resources.

In this study, a microfluidic system previously designed and validated within Eral Lab was further improved. Once improved, the system was used to study the effects of common NPLIN parameters such as supersaturation, laser intensity and laser wavelength on the nucleation probability in thousands of independent micro droplets. The experiments were performed using KCl solutions of both 1.05 and 1.10 supersaturation index and irradiated with light of three different wavelengths and four different laser intensities. Control cooling experiments were conducted to serve as a reference and measure the effectiveness of irradiation.

Results indicated that, increasing the supersaturation increases the nucleation probability. However, small differences between both supersaturations were observed, potentially indicating a supersaturation dependent laser intensity threshold. A threshold possibly explained by the Nanoparticle Heating model used to describe Non-photochemical Laser Induced Nucleation. Laser irradiation of 1.05 supersaturated solutions was seen to be effective with light of all colours at higher laser intensities ($\geq$ 50 MW/cm^2). In contrast, for 1.10 supersaturated solutions irradiation was, in most cases, already effective at lower laser intensities ($\geq$ 25 MW/cm^2). No significant wavelength effect was observed, besides irradiation with 355 nm light at higher laser intensities ($\geq$ 50 MW/cm^2) to be more effective on 1.10 supersaturated solutions.

Further analysis of the data was done by investigating the ability of common nucleation models, such as the Classical Nucleation Theory and the Dielectric Polarization model, to describe the behaviour. Results of the Classical Nucleation Theory were highly uncertain due to a limited amount of data points at varying supersaturations. Yet, indicated a heterogeneous influence on the nucleation probability in both the control cooling and laser irradiation experiments. The Dielectric Polarization model was not able to properly describe the nucleation events observed in the experiments, as lability parameters calculated for the experiments were inconsistent with literature and suffered from significant errors.

Preface

The past months have been an interesting time for both me and the world. As we are still under the spell of Corona, not everything went as planned. Nevertheless, the past couple of months have taught me a great deal about crystallization, electronics, coding, lasers and the power of microfluidics. Slightly pushing me out of my comfort zone, as I had to work more with my hands than with chemicals.

I would like to express my gratitude towards my supervisor Dr. H.B. Eral for guiding me throughout this project and offering insight into the beauty of crystallization and NPLIN. My gratitude further goes out to all the other members of the Eral Lab and even more so the NPLIN group, who throughout all our meetings and encounters have supported this project, helped me grasp important concepts and shape this research into what it has become. A special mention to my daily supervisor Dr. F. Marques Penha who, throughout this thesis, has supported me both instrumental and emotional with all his knowledge and humour. It has been enjoyable working with you all.

Finally, I would like to thank my parents for all their support, the interesting discussions we have had and their willingness to read over and supply feedback to my work throughout the years. As well as my friends emotionally supporting me throughout my studies, if not in words than with all the fun we've had, and especially my girlfriend who supported me throughout my thesis.

I hope you enjoy reading this thesis, as I have enjoyed myself throughout this project.

Vincent J. de Munck

Contents

Appendices

List of Figures

List of Tables

List of symbols

Symbol	**Definition**	**Unit**
A_L	Converged laser beam Area	cm^2
Bo	Bode number	
c^*	Solute saturation concentration	g/Kg solvent
C_1	Protein concentration inside clusters	$mole/m^3$
c	Solute concentration	g/Kg solvent
Ca	Capillary number	
d	Capillary diameter	mm
ΔG_2	Activation barrier for nucleation inside a cluster	J/mole
ΔG_C^0	The standard free energy of protein molecules inside a cluster, referenced against protein molecules in the bulk	J/mole
ΔG_C	Free energy change of cluster formation	J/mole
$\Delta G^*_{Heterogeneous}$	Activation energy for heterogeneous nucleation	J/mole
$\Delta G^*_{Homogeneous}$	Activation energy for homogeneous nucleation	J/mole
$\Delta G_{Homogeneous}$	Change in chemical energy for homogeneous nucleation	J/mole
$\Delta\rho$	Density difference	g/mm^3
ΔG_v	Change in free energy change accompanied by a phase transition	J/m^3mole
ϵ_p	Relative permittivity of a homogeneous dielectric body (cluster)	F/m
ϵ_s	Relative permittivity of a homogeneous dielectric continuum in which the body is immersed (solution)	F/m
η	Viscosity inside a cluster	Pa·s
E	Electric field strength	V/m
F_+	Focal length convex lens	mm
F_-	Focal length concave lens	mm
f_{laser}	Laser frequency	Hz
FR	Focal length Ratio	
g	Gravity constant	m/s^2
I	Laser intensity	MW/cm^2
I_{th}	Laser intensity threshold	MW/cm^2
J	Steady-state rate of nucleation	$1/(\mu Lh)$
k_2	Crystal nucleation rate inside clusters	$1/(m^3s)$
k_B	Boltzmann constant	m^2kg/s^2K
LD_O	Original laser beam diameter	mm
LD_C	Converged beam diameter	mm
m	Lability parameter	cm^2/MW
m_V	Lability parameter corrected for the bulk volume used in literature	cm^2/MW
m_{VI}	Lability parameter corrected for both the bulk volume and laser intensity threshold	cm^2/MW
μ	Viscosity	g/mm·s
μ_c	Chemical potential of solute molecules in crystallized form	J/mole
μ_s	Chemical potential of molecules in solution	J/mole
N	Number of droplets	
$N_{Crystal}$	Number of crystals	
$N_{molecule}$	Number of molecules in a cluster	
v	Molecular (cluster) volume	m^3
$v_{average}$	Average velocity of all measurements	mm/s
$p_{nucleation}$	Nucleation probability	
r	Cluster radius	m
Re	Reynolds number	
ρ	Density	g/mm^3
$\rho_{KCl(aq)}$	Density of KCl in aqueous solutions	g/mm^3
ρ_{PFPE}	Density of PFPE	g/mm^3
$\rho_{Silicon\ Oil}$	Density of Silicon oil	g/mm^3
S	Supersaturation ratio	
$S(\theta)$	Shape parameter accounting for shape effects in heterogeneous nucleation	
θ	Contact Angle	°
T	Temperature	K
t	Induction time	s
t_{laser}	Laser pulse duration	s
U_0 and U_1	Effective rates of formation and decay of clusters at specified temperature	1/s
V	Volume	m^3
We	Weber number	
γ	Interfacial tension	J/m^2

Abbreviations

CNT Classical Nucleation Theory.
CP Circularly Polarized.

DP Dielectric Polarization.

HFE Hydrofluoroether oil.
HPLC High Performance Liquid Chromatography.

KCl Potassium Chloride.

LIN Laser Induced Nucleation.
LP Linearly Polarized.

MSZW Metastable Zone Width.

NaOH Sodium hydroxide.
NPLIN Non-Photochemical Laser-Induced Nucleation.

OKE Optical Kerr effect.

PFPE Perfluoropolyether oil.
PTFE Polytetrafluoroethylene.

TSN Two-step Nucleation Theory.

1

Introduction

Crystallization is one of the oldest used separation and purification techniques applied in a multitude of industries such as pharmaceuticals, food & beverage, agriculture, fine chemicals and many more [1–10]. Its value and wide applicability is in part due to its ability to separate and purify simultaneously. However, it is further increased by the fact that products obtained from crystallization are in general of high purity [3, 5]. The scale of application also rises from the milligram lab-scale to research newly synthesized products to the tonne scale of industrial crystallizers used to obtain for example sugar, making the process very versatile [5].

Crystallization exploits the interactions during first-order phase transition between solid and liquids, and is, even on the industrial scale, still largely a molecular-level process consisting of two steps [4, 11, 12]. The first step is nucleation, it is this initial step in the crystallization process that defines the structure of the crystals formed. In nucleation, molecules gather together and combine in clusters. Clusters that have exceeded a critical radius can grow further in a dynamic process of atoms, ions or molecules precipitating on this initial cluster and redissolving. This is the second step of the crystallization process called growth [3, 5].

The first step in the crystallization process is still not fully understood at a fundamental level. The initial formation of a small cluster occurs on sizes smaller than visible light and on extremely fast timescales in the order of picoseconds. Hence, it cannot be observed with conventional optical microscopes, and current technology simply lacks the appropriate tools to properly measure and monitor this stage of crystallization processes [13]. Therefore, studying the nucleation phenomenon will increase the understanding of the crystallization process, which could lead to more control over the crystallization process, allowing manufacturers to better control product properties such as crystal size, purity, polymorphism and number of crystals [14–16]. Better understanding and tighter control of the crystallization process will allow manufacturers to reduce resource usage and waste production [17].

The driving force for crystallization from solutions is supersaturation. In supersaturated solutions the solute concentration exceeds the saturation concentration, so that the solute molecules can reduce their chemical potential by crystallizing, bringing the supersaturated solution to a lower energy equilibrium state [18]. The degree of supersaturation is expressed as the ratio of the solute concentration to the solutes saturation concentration. So that a supersaturation larger than 1 corresponds to a supersaturated solution, a supersaturation of 1 to a saturated solution and a supersaturation smaller than 1 to an undersaturated solution [14]. Crystallization can only occur for solutions with a supersaturation larger than 1 [19].

The solubility and therefore the saturation concentration of a solute is specific for each solute/solvent combination but also depends on temperature resulting in three different regimes for every temperature (or concentration). Increasing the supersaturation of a solution, to induce nucleation, can be achieved by varying either of the two variables, solute concentration or temperature. The two most widely used crystallization techniques in industries, cooling crystallization and anti-solvent crystallization, rely on this principle [17, 20]. In cooling crystallization, the temperature of the solution is lowered in order to increase the supersaturation and induce nucleation. Whereas in anti-solvent crystallization, the supersaturation is increased by mixing the solution with an anti-solvent.

Further techniques researched to induce or gain control over nucleation and crystallization are seeding, sonocrystallization, microwave assisted crystallization, mechanical shock, photochemical nucleation or laser based techniques such as Laser-induced cavitation, laser trapping, Laser Induced Nucleation (LIN) or Non-Photochemical Laser-Induced Nucleation (NPLIN), which is the topic of this study [21–29].

Non-Photochemical Laser-Induced Nucleation was first reported in 1996 by Garetz et al., whilst trying to observe second harmonic generation of light in supersaturated aqueous urea solutions [28]. The authors observed the apparent induced nucleation of urea upon radiation by unfocused pulses from a Q-switched Nd:YAG laser, where, since the light was in the near infrared, it was improbable that the effects could be attributed to a photochemical mechanism. Based on the dependence of the orientation of the formed crystals on the plane of polarization of the incident light source, the authors put forward a first proposed mechanism of this phenomenon in the Optical Kerr effect (OKE). Since then numerous studies have been conducted on this phenomenon, gathering data on important NPLIN influencing parameters such as laser intensity, laser wavelength, solute supersaturation and filtration as well as putting forward new proposed mechanisms, such as the Dielectric Polarization (DP) model and the Nanoparticle Heating model, to describe the NPLIN phenomenon. So far, no clear mechanism can be definitively stated to model the NPLIN phenomenon, as all proposed mechanisms fail to completely describe all reported experimental results as a whole [13, 15]. Furthermore, it is believed that laser exposure cannot only induce nucleation, but also affect crystal size, amount, polymorph and morphology [30].

Current research of the phenomenon is largely hindered by the stochastic nature of the process, requiring a substantial number of data points to draw definitive conclusions. Therefore, past research often made use of numerous batch samples to reach a statistically significant number of data points [31]. In 2014, Clair et al. developed a first high throughput controlled set-up for NPLIN studies [32]. The set-up made use of an automatized carousel holding 90 High Performance Liquid Chromatography (HPLC) vials that could be irradiated by a laser from above. Even though this set-up takes away much of the manual labour, it still results in long processing times needed to obtain large data sets. Microfluidics offers a solution to this problem since it allows for the continuous study of solutions, requires less resources and has already proven its value in the investigation of crystal synthesis of pharmaceuticals, nanocrystals and proteins [33–40].

Only three studies on NPLIN in continuous systems have been reported thus far. The first study was published in 2017, and reported a continuous system of alternating supersaturated Potassium Chloride (KCl) solution slugs in a continuous phase fluid [13]. This study reported major problems such as 'spontaneous' nucleation throughout the system that hindered study of the phenomenon. The second study published in 2019 by Hua et al. presented a new microfluidic device that exposed a continuously moving supersaturated solution of KCl to pulsed laser beams [41]. This study was more successful and provided insight into the effects supersaturation, laser energy, pulse duration and number of pulses can have on the number of crystals and their size. The authors further expanded their work with this set-up in a second study published in 2020, where the previously designed microfluidic device was used to study NPLIN of supersaturated aqueous glycine solutions [42]. The study encountered a number of phenomenon previously discovered in batch studies of NPLIN on glycine, further validating the use of microfluidic set-ups to study NPLIN [43, 44].

Current research utilizes a droplet-based microfluidic set-up, to study the effects of laser irradiation on supersaturated aqueous KCl solutions and increase understanding of the underlying phenomena. KCl was chosen as a subject based on its affordability and fast acting kinetics, easing study of the phenomenon. The microfluidic device used in this study was previously designed to create volume-controlled, stable, supersaturated solution droplets, allowing each and every droplet to act as a separate micro-reactor [16]. Therefore, this device, in contrast with previous research, allows for the gathering of large amounts of completely independent data points, effectively addressing the stochastic nature of the crystallization process.

1.1. Research Objectives

The overarching goal of the project within Eral Lab is to increase understanding of the NPLIN phenomenon and eventually be able to tightly control (industrial) crystallization processes, focused on tuning crystal size, number of crystals and more importantly crystal polymorphism. Within this study, it is the goal to improve understanding of the NPLIN process and study the effect of well known NPLIN parameters such as supersaturation, laser intensity, laser wavelength on the nucleation probability. The developed system effectively addresses the stochastic nature of NPLIN, since each supersaturated droplet formed will function as its own separate micro-reactor. As a result the system is capable of gathering a large independent data set on each studied variable by performing a sizeable amount of identical experiments in a short amount of time when compared to conventional systems used to study NPLIN [32]. However, before study of the NPLIN phenomenon can take place a number of modifications to the system, stated below, were made to optimize the previously designed set-up [16]. Overall, the goal of these modifications was to minimise the amount of noise present in the data as to ease data analysis and thereby improve the reliability and quality of the gathered data.

Firstly, in the previous study it was proposed to alter the continuous phase in order to reduce the amount of solvent or air bubbles detected in the data and improve droplet shape. However, a change in solvent most probably has a direct effect on the tubing used in the droplet generation zone of the set-up, where it is key to minimize the interaction between solvent and tubing to avoid clogging, loss of solvent and control droplet spacing. Therefore, a number of continuous phase options were considered and simultaneously examined for their interaction with the available tubing options.

Secondly, in the previous study it was noted that the supersaturated droplets analyzed in crystal observation zone had thick, dark boundaries, which complicated crystal detection, both manually and via image analysis. It was proposed to improve the hydrophobicity of the used confinement material, to reduce the interaction between the solution droplets and their confinement material. Therefore, as to ease analysis of the data, a number of different hydrophobic coatings were examined in order to minimize the droplet interaction with the capillary, to ensure no points for heterogeneous nucleation arose and droplet boundary thickness decreases.

Thirdly, in the previous study an iris was used to decrease the width of the laser beam, but suffered from significant damage. Therefore, a number of small modifications were made to the laser directing set-up, to improve its durability, Additionally, this allows for the implementation of control over the amount of laser pulses each droplet is exposed to.

Finally, the previous study reported wide size distributions proposed to be caused by droplet coalescence within the system. In order to ensure the generation of independent volumes, and thereby truly independent samples, this study focused its efforts to eliminate the cause of droplet coalescence and improve droplet formation.

After adaptation and improvement of the system, it was used to study the effects of supersaturation, laser intensity and laser wavelength on the nucleation probability in NPLIN. However, before study of the NPLIN phenomenon the system was used to gather data in a number of cooling experiments, so called control experiments, to serve as a reference to the laser irradiation experiments.

1.2. Thesis Outline

The structure of this study follows the path of development followed during this project. First, an initial literature review to asses the current state of research on crystallization, Non-Photochemical Laser Induced Nucleation and microfluidic systems published to study this phenomenon is presented. The following chapter highlights what previous work has been done within Eral Lab on the development of a droplet based microfluidic system as well as modifications made to this design during the research at hand. Subsequently, the modified system was used to study the NPLIN phenomenon in so called laser irradiation experiments. The laser irradiation experiments study and test the influence of NPLIN parameters such as supersaturation, laser intensity, laser wavelength on the nucleation probability. The results of the laser irradiation experiments are presented and compared to control cooling experiments as well as data currently available in literature. Further analysis of the data is done by discussing the results in light of well known nucleation models and NPLIN mechanisms. The report is then concluded by a chapter summarizing its conclusions and recommendations for future research.

2

Literature Review

In this chapter, a general introduction to crystallization is given, followed by a more detailed description of the characteristics of nucleation, models describing nucleation behavior and factors affecting nucleation. Subsequently, a general introduction to NPLIN, factors affecting it and models proposed to describe NPLIN are presented. Followed by a small detailed section on microfluidic systems published to study NPLIN. The chapter is ended by a considerations section, summarizing the current state of research and the purpose of this study.

2.1. Crystallization

As mentioned in Chapter 1, crystallization has been used as a separation or purification step in a wide variety of industries. It is a molecular-level process that exploits the interactions during the first-order phase transition between liquids and solids consisting of two separate steps, nucleation and growth, where nucleation is described as the first ordering of small clusters in solution [3]. If a certain threshold size, known as the critical radius, has been exceeded by the clusters, crystal growth takes place and forms full sized crystals [3, 4]. It is the initial step of the crystallization process, nucleation, that determines the crystal structure. Therefore, it is of key importance to improve understanding of this initial step in order to gain control over the crystallization process, reduce waste production and minimize resource usage. Furthermore, improved control over the crystallization process can have great environmental and economical impact due to its widespread use.

2.1.1. Nucleation

Literature has reported two different mechanisms for nucleation, primary and secondary nucleation, in either mechanism the driving force is supersaturation. Primary nucleation occurs spontaneously without the new phase being present and can be further divided into homogeneous and heterogeneous nucleation [45]. Primary homogeneous nucleation occurs in the bulk of a solution without any preexisting solid structure to aid it. In practice, this means it only occurs in highly saturated ultra-pure systems [45]. Whereas primary heterogeneous nucleation occurs in the presence a solid inert surface, using this as a nucleation site for crystals to grow [15]. Effectively, this means crystals will grow on solid impurities present in the solution or the solid walls of the confinement vessel [45]. Secondary nucleation, in contrast to primary nucleation, utilizes a small amount of preexisting solid material as a nucleation site to grow, generally induced by seeding [15, 21].

Thermodynamics

The driving force of crystallization, supersaturation, is the result of an imbalance between the chemical potential of solute molecules in solution and crystallized form. In this imbalance, the chemical potential of molecules in solution (μ_s) is larger than the chemical potential of solute molecules in crystallized form (μ_c) [18]. Consequently, solutions can lower their overall chemical energy by facilitating the formation of crystals [18]. The change in this overall chemical energy can be described in light of the Classical Nucleation Theory (CNT) first reported on by Gibbs et al., further described in section 2.1.2, and its value can be estimated using Equation 2.1 [19, 46]. Where r is the cluster radius, $\Delta\ G_v$ is the free energy change accompanied by the phase transition, γ_{SL} is the interfacial tension between the newly formed solid and the liquid.

$$\Delta G_{Homogeneous} = \frac{4}{3}\pi r^3 \Delta G_v + 4\pi r^2 \gamma_{SL} \tag{2.1}$$

In this equation, it can be seen that the change in free energy for homogeneous crystallization is dependent on two terms, the first resembling the free energy change of the phase transition and the second resembling an energy change due to the newly formed interface between the solid and liquid solution. All phase transitions have an activation barrier, the size of which determines the amount of energy needed to be supplied for the transition to occur [19]. For homogeneous nucleation, the size of this barrier can be estimated using Equation 2.2 [19].

$$\Delta G^*_{Homogeneous} = \frac{16\pi\gamma_{SL}^3}{3(\Delta G_v)^2} \tag{2.2}$$

It is known that the activation energy of heterogeneous nucleation is smaller than that of homogeneous nucleation, as the transition makes use of a solid inert surface to serve as a nucleation site which lowers the solid-liquid interfacial energy [18]. It is noted that a further difference in the nucleation activation barrier between homogeneous and heterogeneous can be caused by the shape of the nucleus [18]. Thus, the change in free energy associated with the phase change, see Equation 2.1, is also dependent on the size of the surface of the newly formed solid. Similar to Equation 2.2, the size of the activation barrier for heterogeneous nucleation can be estimated using Equation 2.3. Where γ_{SL} is the interfacial tension between the newly formed solid and the liquid and a shape parameter S(θ) has been added to account for any shape effects.

Due to the lower activation barrier, heterogeneous nucleation is far more likely to occur than homogeneous nucleation. Therefore, care should be taken when conducting experiments to ensure formed crystals cannot be attributed to some sort of heterogeneous nucleation point.

$$\Delta G^*_{Heterogeneous} = \frac{16\pi\gamma_{SL}^3}{3(\Delta G_v)^2} S(\theta) \tag{2.3}$$

Supersaturation Ratio

At a macroscopic scale, the definition of supersaturation is formulated in several different ways and simplified to include directly measurable quantities. For the study at hand it is defined as the supersaturation ratio (Equation 2.4). The supersaturation ratio (S) is a dimensionless quantity defined as the ratio between the solute concentration (c) and its saturation concentration (c^*) at the specified temperature.

$$S(T) = \frac{c}{c^*(T)} \tag{2.4}$$

As a solute's saturation concentration is dependent on temperature, the supersaturation is also temperature dependent. The relation between saturation concentration and temperature is depicted in a solubility curve. An example for the solute studied in this study, KCl, has been included in Figure 2.1. This figure demarcates three different zones separated by the two solubility curves, the saturation and the supersaturation limits. The zone underneath the saturation curve, demarcates the stable zone, where the saturation ratio is smaller than 1. In this zone nucleation does not occur and existing crystals will dissolve. The second zone is labeled the metastable zone and can be found in between the two solubility curves. In the metastable zone, nucleation might not occur spontaneously but can be induced by any of the aforementioned techniques in Chapter 1. Crystals present in metastable solutions can grow until the saturation limit is reached. The Metastable Zone Width (MSZW), defined as the distance between the saturation and supersaturation limit curve, is not a fixed value and can only be empirically defined for each system as it is influenced by a number of experimental factors [13, 47]. Therefore, it is advisable to determine the MSZW, as to ensure operation of the studied system takes place within the boundaries of the metastable zone. The final zone can be found above the supersaturation limit curve, above this curve solutes will spontaneously nucleate and crystals can grow until the saturation limit is reached.

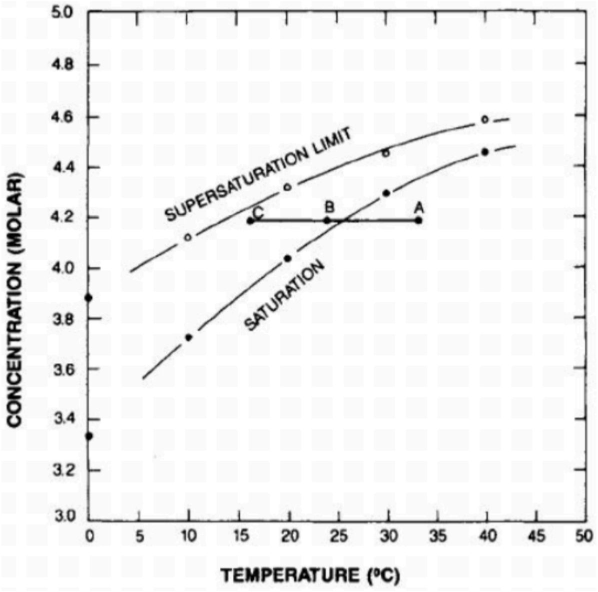

Figure 2.1: The solubility curve of KCl in water solutions. The region underneath the saturation curve is the stable zone, the region between the saturation and supersaturation limit curves is the metastable zone and the region above the supersaturation limit curve is the unstable zone [48].

2.1.2. Nucleation Models

Numerous models have been proposed to describe nucleation, but the two most widely accepted models are Classical Nucleation Theory (CNT) and Two-step Nucleation Theory (TSN) which are discussed in the following sections as well as factors found in literature to affect nucleation.

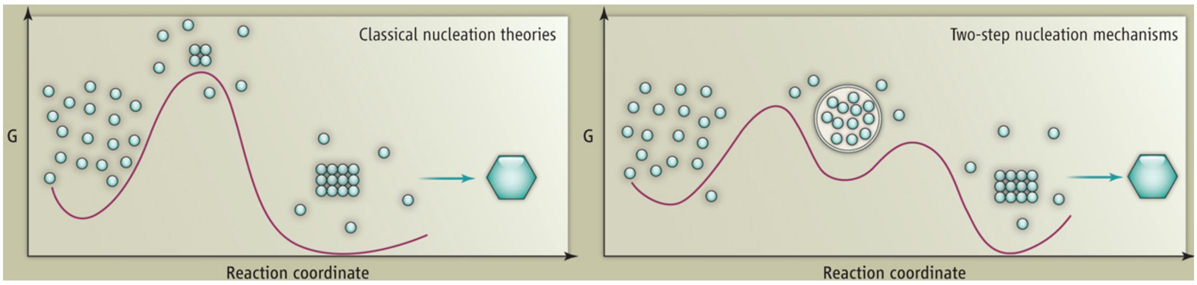

Figure 2.2: Free energy diagrams of the proposed pathways for the Classical Nucleation Theory (left) and Two-step nucleation theory (right) [49].

Classical Nucleation Theory (CNT)

The Classical Nucleation Theory is one of the oldest and simplest models put forward to describe nucleation and treats it as a first order, single step phase transition (See Figure 2.2). It was originally put forward by Gibbs et al. to describe condensation of a vapour into a liquid and extended to describe solid formation [15]. It describes solid formation to occur through the random aggregation of molecules governed by both the relative size of the free energy change of solid formation and interfacial energies, as seen in Equation 2.1 [13, 19, 50]. The two mechanisms are in competition with each other, since energetically it will be more favourable for ions to be in the bulk of a newly formed solid and unfavourable to be at the surface of this solid. Both mechanisms are dependent on the relative size of the cluster, the favourable free energy change of formation is proportional to r^3, whereas the unfavourable interfacial energy is proportional to r^2. Hence, there will be a relative cluster size at which the favourable phase transformation outweighs the unfavourable surface interactions, the so-called critical radius (r_c), and the transformation occurs.

Several assumptions underlay the CNT model [13, 19]:

- Clusters are assumed to be spherical and their molecular arrangement resembles that of the full grown crystals.
- Surface energies are temperature, curvature and size independent.
- Once the critical radius has been exceeded, crystal growth occurs in a step wise manner, one monomer at a time, into the crystal lattice with clusters at rest.
- Nucleation rate is time independent and perfectly distributed in space.
- Formation of clusters does not alter the vapour state and they are incompressible in ideal gas.

These assumptions simplify the model for ease of applicability, but as a result CNT frequently fails to correctly describe nucleation processes and is faced with a number of limitations [13, 19]:

- The predicted nucleation rates are 1-2 orders of magnitude higher than experimental nucleation rates.
- Temperature dependent corrections are required.
- It fails to describe binary systems with concentration gradients, since it assumes uniform composition.
- It cannot deal with small nuclei.
- Nuclei properties differ significantly from final crystal properties.
- Its single dependent variable, size, means the model does not provide information on the substructure of clusters or pathways leading from solution to solid state.
- It does not take into account molecular self assembly and cannot predict which polymorph will be formed.

However, due to its simplicity it is still a widely accepted and used model that allows the steady-state rate of nuclei formation to be described by an Arrhenius like equation (Equation 2.5) [13, 19, 50]. In which J is the steady-state rate of nucleation, γ is the interfacial tension, ν is the molecular volume, k_B the Boltzmann constant, T the temperature, S the supersaturation of the solution and A a pre-exponential factor.

$$J = A \exp\left(\frac{-16\pi\gamma^3\nu^2}{3k_B^3T^3(\ln S)^2}\right) \tag{2.5}$$

Despite the ease of usability of CNT, its limitations have lead to the proposition of numerous other models to describe nucleation such as the Two-step Nucleation Theory (TSN).

Two-step Nucleation Theory (TSN)

Two-Step nucleation theory has been developed from empirical evidence and, as its name already implies, assumes the transition from dissolved solute to solid crystal to take place in two steps (see Figure 2.2). In the first step, a highly disordered but dense liquid phase that approaches the density of a crystal is formed. In the second step these clusters can overcome a small energy barrier, smaller than in CNT, to form an ordered solid with similar density to the previous cluster which can than further progress towards a crystal [19, 50]. However, there is evidence to suggest the formed solid may still be (partially) amorphous and further (phase) transitions are needed to form a stable crystal structure [13, 51]. The first step in this process is mainly a growth step, growing the amorphous cluster to a certain size, whereas the second step is mainly a step to develop crystalline order within this amorphous cluster for the formation a crystalline solid [15]. A 2005 paper by Pan et al. on the crystallization of proteins via a dense liquid intermediate proposed a first expression (Equation 2.6) for the steady-state rate of nucleation described by the TSN model [13, 52].

In this expression, J is the steady-state rate of nucleation, k_2 the crystal nucleation rate inside clusters, C_1 the protein concentration inside clusters , ΔG_2 the barrier for nucleation inside the cluster, k_B the Boltzmann constant, T the temperature, η the viscosity inside the cluster, U_1 and U_0 the effective rates of formation and decay of clusters at temperature T and ΔG_C^0 the standard free energy of protein molecules inside the cluster, referenced against protein molecules in the bulk, which has been experimentally determined to be roughly 10 times $k_B T$ [13, 53].

$$J = \frac{k_2 C_1 T \exp(-\frac{\Delta G_2^*}{k_B T})}{\eta(C_1, T)[1 + \frac{U_1}{U_0}\exp(\frac{\Delta G_C^0}{k_B T})]} \tag{2.6}$$

The advantage of this proposed model is that it has more order parameters, allowing for a more detailed description of the process. However, the disadvantage is that these parameters, asides from temperature, do not offer external control and will therefore still require in-situ measurements of parameters to apply or validate it for a studied process.

2.1.3. Nucleation Affecting Factors

Literature has shown that a number of different factors can affect nucleation and a subset of them is presented in this section along with a small discussion how they influence nucleation.

Supersaturation

In general, solutions of higher supersaturation will exhibit a higher tendency to nucleate [18, 48, 54]. Simply because more solute molecules are available to form clusters and an increased chemical potential difference between solute molecules in solution and solid form. Once nuclei are formed in a supersaturated solution, they are able to grow until the saturation limit has been reached and the solution is no longer supersaturated.

Volume

Fang et al. showed that nucleation strongly depends on volume according to Equation 2.7, where J is the nucleation rate, V the volume and t the time for nucleation to be detected [55]. The main taking from their results was that at small volumes, supersaturation values much higher than expected, based on bulk volume experiments, where needed to induce nucleation. In their study effectively proving that the nucleation rate is directly proportional to volume. The explanation offered by Fang et al. for this phenomenon, is that in small volumes, but similar supersaturation, the absolute amount of molecules present is almost negligible. As a result, cluster formation has a direct and significant impact on the supersaturation of the bulk solution, thus increasing the barrier for nucleation.

$$J_1 V_1 t_1 = J_2 V_2 t_2 \tag{2.7}$$

Temperature

Temperature can affect the nucleation probability, where solutions of similar supersaturation seem to be significantly more likely to nucleate at higher temperatures than at lower temperatures [56]. An explanation for this phenomenon is offered by the fact that at similar supersaturation but higher temperatures the absolute concentration, and thereby number of solute molecules present, is larger. Thus, there will effectively be more solute molecules able to form clusters, and the formation of cluster sizes exceeding the critical radius will become more likely. However, this explanation fails to capture the behaviour seen for solutes for which the solubility decreases with temperature. Such that the increased likeliness to nucleate could be caused by the increased movement of molecules at higher temperatures, increasing the probability of cluster formation.

Impurities

Impurities can offer additional surfaces for nucleation to take place heterogeneously [57]. Furthermore, since the activation barrier for heterogeneous nucleation is lower than for homogeneous nucleation, the former is far more likely to occur. Thus, if the goal is to strictly study homogeneous nucleation, care should be taken to minimize impurities.

External Nucleation Surfaces

Similar to impurities, external surfaces, of e.g. syringes, tubes, capillaries or other equipment, can offer additional surfaces for nucleation to take place through material structure or surface imperfections. This was seen for example in the first study found to explore NPLIN in a microfluidic system, where the researcher encountered major undesired heterogeneous nucleation at joints used in the set-up [13].

Ideally, in a droplet-based microfluidic set-up the interaction between a solution and the micro channel confinement is minimized to ensure free flowing and undisturbed droplets [16, 58]. Therefore, effectively reducing the amount of interaction the droplets have with external surfaces and minimizing the chance of unwanted heterogeneous nucleation.

2.2. NPLIN

Upon its first discovery in 1996 its authors were surprised when, attempting to observe second harmonic generation in supersaturated solutions of urea in water, they noticed that the laser pulses seemed to induce nucleation in the irradiated solutions [28]. The incident light source used in their experiments was near infrared, little to no absorption by either solvent or solute was expected based on their absorption spectra, thereby effectively ruling out a mechanism of photochemical degradation [28, 59]. The incident light was also of an intensity and pulse width unable to induce absorption, cavitation or prolonged photon pressure [13, 15]. Further, the authors noted a preferred orientation of the formed nuclei, dependent on the plane of polarization of the incident radiation, suggesting an electric field induced effect. Based on this observation, the authors proposed a first mechanism to explain these effects based on the Optical Kerr Effect (OKE), which is elaborated on further in section 2.2.2 as well as the presentation of other mechanisms put forward since then.

Numerous studies have been put forward studying NPLIN, mainly focused on the underlying phenomena and factors affecting it. The phenomenon has been observed in aqueous solutions of for example, urea, glycine, alkali halides such as KCl or KBr, proteins, carbon dioxide bubbles or minerals such as ammonium chloride but also in mixed and organic solvent solutions of pharmaceuticals [13, 28, 30, 41, 55, 60–71]. But, at present the phenomenon and its underlying mechanism are still not unraveled. A recent review published by Alexander and Camp offers a great overview of the work carried out so far [15]. The review mentioned a number of advantages over other nucleation methods and also a number of limitations of NPLIN, which are listed below. Furthermore, it provides an overview of knowledge gained on NPLIN affecting factors and models put forward to describe it, which are presented in sections 2.2.2 and 2.2.1.

Advantages NPLIN offers [13]:

- Improved temporal control of nucleation through the time and duration of the laser pulse.
- Spatial control of nucleation through the shape, size and pathway of the laser beam.
- No photochemical damage to the system due the variability in laser wavelength and intensity that can be used.
- Application to closed systems from a distance.
- The alleged ability to alter morphology of the formed crystal

Limitations to NPLIN Application [13]:

- Components used must have low optical absorbance to avoid heating or photochemical damage to the system.
- Practical limitations to the volume of a system that can effectively be exposed to the laser light.
- Practical limitations to materials that are suitable to use.
- Some systems are simply not NPLIN active.

This shows that NPLIN offers significant advantages over currently used techniques, with little limitations and can thus have a considerable impact on the ability to control and steer crystallization processes. But, as will become more apparent in the following sections, its application is at present still limited in part due to the pure practical limitations mentioned above as well as a lack of understanding of the phenomenon itself.

2.2.1. NPLIN Affecting Factors

Despite the fact that the exact mechanism of NPLIN has not been unveiled yet, through all the research conducted, a better understanding of factors that can influence it has been collected. This section presents a short overview of phenomena encountered in NPLIN studies, NPLIN affecting factors and the remarkable results that support it.

Nucleation affecting factors

As NPLIN is solely a technique to induce nucleation, the process itself is still a nucleation process. Therefore, common nucleation affecting factors such as supersaturation, temperature and volume will still affect the nucleation process similarly as described in the previous section.

Impurities

A study conducted within Eral Lab as well as research published in literature, showed that upon filtration of supersaturated solutions, with a number of different pore sized filters, a significant decrease in nucleation probability was observed [15, 47, 62, 72]. Whereas intentional doping of the filtered solutions with iron-oxide nanoparticles resulted in reversal of the effect [62]. These studies once again highlighted the effects of (nano) impurities present in the solution. The proposed role of the (nano) impurities on the nucleation probability could be two-fold. Impurities present in solution could offer additional external surface area, thereby facilitating the nucleation process and reducing the energy barrier for nucleation, effectively making it a heterogeneous nucleation process. A second explanation for the effects of impurities present in solution is offered in the Nanoparticle heating mechanism, further elaborated on in section 2.2.2.

Laser Intensity

Studies published so far generally show that the nucleation probability is independent of the total laser energy, and more so dependent on the peak laser intensity of the incident laser light [15, 47, 56]. In general, it can be seen that the nucleation probability is strongly dependent on the peak laser intensity of the incident beam. The observed systems tend to show a threshold laser intensity below which no nucleation appears to take place and possibly a saturation peak intensity above which the probability of nucleation is always unity. Furthermore, it is generally seen that, for KCl, the nucleation probability varies linearly with laser intensity [15, 41, 64].

Laser Wavelength

Contradictory results on the effects of varying wavelengths have been obtained so far. Studies conducted by Matic et al. and Ward & Alexander have both observed a lower laser intensity threshold and increased nucleation probability when irradiating solutions with 532 nm pulses as compared to 1064 nm pulses in both urea and KCl solutions [56, 60]. Whereas a recent study carried out within Eral Lab reached a less clear conclusion. The study noted a slight improvement in nucleation probability of KCl upon irradiation with 355 and 532 nm pulses, as compared to 1064 nm pulses, which could be attributed to the slight absorption of water at this wavelength [47]. Consequently resulting in a slight local temperature increase, decreasing the local supersaturation. However, the small differences in observed nucleation probabilities could also be attributed to fluctuations in other experimental conditions such as temperature of the surroundings, lack of fine control over the laser power or curvature effects of the vials used in the experiments.

Laser Pulse Duration

Similar to the results on the effect of laser wavelength on the nucleation probability, there are contradictory statements made on the effects of laser pulse duration. Studies have been conducted using laser pulse duration's varying from femto to nano seconds [62, 63, 67]. In its studies, the group of Alexander has found that NPLIN is not observed for femto second duration laser pulses, whereas it is observed for nano second duration pulses at similar or lower peak power densities per pulse [62].

This paper suggests that the mechanism of NPLIN might be dependent on the heating of solid nanoparticles, which depends on the total energy density per pulse (J/ cm^2) and is significantly larger in the nanosecond case due to the longer pulse duration. However, in a study published by the same group, conducted in the nanosecond timescale, no significant differences in nucleation probability were observed upon irradiation with 6 or 200 nanosecond pulses with comparable peak power densities (MW/cm^2) [63]. Based on these results, the authors stated that the nucleation probability depends on the peak power density and not on the duration, and therefore the total energy, of the pulse.

Light Polarization

Early research by Garetz et al. on NPLIN focused on glycine as a solute molecule to study its behaviour and susceptibility to NPLIN [61]. These studies yielded a fascinating result, where it seemed that NPLIN favored nucleation of the γ polymorph whereas spontaneous nucleation under similar conditions tended to yield the α polymorph [73]. Further studies showed that this effect could be ascribed to the polarization of the light used, their results indicated that Linearly Polarized (LP) light yielded the γ polymorph and Circularly Polarized (CP) light yielded the α polymorph, a phenomenon coined polarization switching. Theses results indicated some form of crystal polymorphism control could be achieved by alternating the light polarization, without the need for seed crystals [74]. However, a study published since then by Sun et al., seemed to debate the degree of control that can be offered. As it found that polarization switching could only be achieved in a very narrow window of conditions [75]. Further studies since then have also been unable to successfully reproduce the previously found polarization switching effects [32, 72, 76].

Aging

The first studies conducted on NPLIN focused on solutes such as urea and glycine [28, 60, 61, 73]. In almost all experiments 'aging' of the solutions seemed to be a prerequisite for NPLIN, a phenomenon explained based on the required time to grow a population of large, sub-critical clusters that could nucleate upon irradiation. Later studies conducted using solutes such as KCl did not seem to require this aging time for NPLIN to occur [64]. Therefore, the requirement of aging seems to vary according to the solute and is not yet proven.

Number of laser pulses

The effect of the number of laser pulses supersaturated solutions are exposed to has been researched for multiple solutes, e.g. KCl and glycine, all reaching similar conclusions. Hua et all, in the first successful study of NPLIN in microfluidics, found no significant difference in the nucleation probability for exposure of the supersaturated KCl solution to either 6 or 1.2 pulses (6 nanosecond - 1064 nm) [41]. In agreement with results found previously by Alexander and Ward, who showed that exposure of a supersaturated solution to a single pulse (7 nanoseconds - 1064 nm) yielded a single crystal [64]. Similarly, a study conducted within Eral Lab by Irimia et all found no significant difference in the nucleation probability when exposing a supersaturated glycine solution to either 600 or 1 (7 nanosecond - 1064 nm) pulse [77]. Explanations for these observations where given based on the trade-off between increasing the amount of possible nucleation events and sample heating due to the slight absorbance of water at 1064 nm [77]. A further explanation was based on the Dielectric Polarization model, which will be described in the next section. In short, it proposes that the first pulse causes all the pre-critical clusters, slightly smaller than the critical radius, present within the irradiated volume to become critical and nucleate. The region irradiated by the first pulse is thus depleted of pre-critical clusters able to exceed the critical radius upon irradiation by any additional pulses [41].

2.2.2. NPLIN Mechanisms

Upon its first discovery the authors also attempted to put forward a mechanism, the OKE mechanism, to describe the observed phenomena, not ruling out any other mechanism that could potentially describe the observations [28]. Since then, multiple studies haven been published providing data that is inconsistent with the OKE mechanism, sparking other mechanisms such as the Dielectric Polarization (DP) and the Nanoparticle Heating to be put forward. This section describes each of them in limited detail.

Optical Kerr Effect (OKE)

The Optical Kerr Effect was initially put forward by the discoverers of NPLIN to explain the observed preference of crystal orientation in the direction of the incident laser light [28]. This preferred orientation was explained by the ability of the incident laser light to rearrange the solute molecules along its path. It was presumed that the molecules are aligned along the axis of the laser's electric field just as they are in the OKE. In the OKE, the incident electric field induces a temporary dipole moment in a molecule, and simultaneously interacts with this induced dipole moment. The incident electrical field applies a torque to the molecule and aligns it so that its most polarizable axis is parallel to the field [15, 28]. In supersaturated solutions, solute clusters are continuously assembling and separating. The explanation for the observed effect is that the applied electric field aids in the organizing and rearranging of cluster structures, increasing the chances of generating solid clusters exceeding the critical radius and nucleating [5, 28]. However, simulations have shown that, at the employed laser intensities, the torque created by the electric field is orders of magnitude too low to achieve significant alignment of the molecules [15, 47, 78]. This lack of strong physical foundation, as well as its failure to describe NPLIN of for example halide salts, lead to the development of other models proposed to describe NPLIN.

Dielectric Polarization (DP)

Observations of NPLIN effects in aqueous solutions of simple halide salts such as KCl that form cubic crystal structures, and therefore have no preferred axis of alignment, could not be explained using the previously discussed OKE mechanism [15]. Thus, an alternative mechanism operating within CNT based on the Dielectric Polarization (DP) of solute clusters was developed to describe these observations, without ruling out the OKE mechanism as an explanation for the before observed effects on organic molecules [15, 41, 64]. Similar to the OKE mechanism, the lasers electric field is assumed to play a significant role in polarizing the electrons of the constituent atoms of a cluster. It is proposed that the slight alteration of the electron cloud surrounding the nuclei can slightly lower the free energy of the solute clusters compared to the surrounding solution, effectively stabilizing the solute clusters. The lowered free energy and accompanying stability of the solute cluster, decreases the size of the critical radius needed to exceed for nucleation and subsequent growth to occur. At a constant cluster size distribution, but a smaller critical radius, a larger portion of clusters will exceed this threshold value and nucleate, therefore increasing the nucleation probability. Furthermore, it is also proposed that the lowered critical radius is accompanied by a subsequent lowering of the nucleation activation energy.

Based on the results from classical electromagnetism within the DP model, it is proposed that the cluster free energy change, under the action of the electric field, is proportional to $-\nu(\epsilon_p-\epsilon_s)E^2$, where ν is the volume of the affected region (in this case the cluster volume), ϵ_p is the relative permittivity of the homogeneous dielectric body (in this case the cluster), ϵ_s is the relative permittivity of the homogeneous dielectric continuum in which the body is immersed (in this case the bulk solution) and E is the electric field strength [15, 79, 80]. This model has been thoroughly tested and seems to fit most experimental results found and describe the encountered variations in nucleation probability ($p_{nucleation}$) with common NPLIN affecting factors such as temperature, supersaturation, solute and incident wavelength [15]. Furthermore, within this model, based on experimental observations which were elaborated on in Section 2.2.1, it is proposed that the number of crystals varies linearly with the laser intensity (see Equation 2.8) and the nucleation probability can be calculated assuming a Poisson distribution by the relation in Equation 2.9 [15]. In this expression $N_{Crystal}$ is the average number of crystals produced, *m* a 'lability' constant describing how susceptible a solution is to nucleation upon irradiation and I the incident laser intensity in MW/cm^2. The lability constant can be calculated using Equation 2.10 or determined by fitting of experimental data to Equation 2.9 [15].

$$N_{Crystal} = m \cdot I \tag{2.8}$$

$$p_{nucleation} = 1 - \exp(-N_{Crystal}) \tag{2.9}$$

$$m = \frac{3N_{molecule}\gamma a}{2\pi\rho^3(k_B T\ln(S))^2} \cdot \frac{\exp(-\Delta G_c(0)/k_B T)}{\int_0^{r_c(0)} r^3 \exp(-\Delta G(r,0)/k_B T)dr} \tag{2.10}$$

However, the aforementioned relationships fail to accurately describe a laser intensity threshold for NPLIN to occur encountered in experimental data. Therefore, the relationship in Equation 2.9 is generally adjusted to 2.11 where I_{th} is the laser intensity threshold, discussed in Section 2.2.1.

$$p_{nucleation} = 1 - \exp(-m(I - I_{th})) \tag{2.11}$$

Nanoparticle Heating

Both proposed mechanisms so far fail to accurately describe all experimental observations such as the mentioned laser intensity threshold, why some systems exhibit NPLIN and others do not and why in many cases filtration significantly reduces nucleation probabilities. The significant decrease in nucleation probability in filtered compared to unfiltered solutions were seen as a strong indication that small nano impurities had a role in activating NPLIN [15].

Several explanations for the role of solid nano impurities present in the solution have been proposed, all surrounding the rapid heating of these impurities to a high temperature (>2000 K) by the incident laser light, causing formation of a small vapor cavity [15]. One of the explanations stated that solute molecules near the interface of this vapor will be less well solvated, hence more likely to cluster and nucleate. A second explanation offered, is that the large temperature difference between the formed vapor phase and surrounding solution results in rapid heat transfer, causing the formation of pressure waves. The last explanation offered is that the formed vapor cavities will rapidly collapse resulting in the destruction of the nanoparticle, temporarily forming a plasma-like state or inducing nucleation at fresh solid-liquid interfaces.

The proposed Nanoparticle Heating mechanism seems to be able to explain several observations from previous studies that the two above-mentioned theories failed to describe, such as [15]:

- Threshold laser power intensities are observed because a threshold temperature is required for the formation of a vapor cavity.
- The varying composition and concentration of impurities of different solutions can explain the major differences encountered between different NPLIN experiments published.
- Aging effects encountered in some NPLIN experiments can be accounted to the time dependent aggregation of nanoparticle impurities.
- Filtration affects NPLIN due to the removal of active nano impurities from the studied solutions.
- Polarization switching can be explained by the polarization-dependent optical absorption of the nanoparticle impurities.

As might have been clear from their descriptions, each of the above mentioned mechanisms only partially explains the observations encountered during NPLIN experiments and it might well be possible that several mechanisms contribute to the phenomenon.

2.2.3. NPLIN in Microfluidics

Microfluidic set-ups have been used for quite some time already to study metastable zone widths, determine nucleation rates and for screening and optimizing of nucleation conditions [81–87]. The power of microfluidics in these experiments is its ability to conduct numerous experiments under identical conditions in a short amount of time with low resource usage [33–40, 81]. The advantage of those large amounts of identical experiments is the statistical significance of the obtained results, greatly improving their reliability as compared to batch experiments [31, 88]. Despite the substantial benefits and long term use of microfluidics in research, NPLIN in microfluidics is still relatively new with the first study only published in 2017 [13].

The first published study made use of a continuous system of alternating supersaturated solution slugs in a continuous phase fluid [13]. This study reported major problems with unwanted nucleation in joints between separate parts of the microfluidic device that hindered further study of the phenomenon. Furthermore, it reported undesired 'spontaneous' nucleation throughout the system that could not directly be attributed to the effect of the laser. The major problems encountered within this study prevented it from reaching a clear conclusion on the validation of the design and the effects of laser irradiation on nucleation rates.

The second study was published in 2019 by Hua et al., it presented a new microfluidic device that exposed a continuously moving supersaturated solution of KCl to pulsed laser beams [41]. In this device, the supersaturation is controlled by tight temperature control of the micro channel. Its tight temperature control allows for cooling of the solution to the desired temperature upon entry and heating of the solution near the exit to prevent formed crystals from clogging the channel. This study was more successful than the first, providing more insight into the effects of supersaturation, laser energy, pulse duration and number of pulses on the number of crystals and their size. They further expanded the knowledge base on NPLIN with a third paper published in 2020, where the previously designed set-up was used to study NPLIN of supersaturated aqueous glycine solutions [42].

The study attempted to induce nucleation in freshly prepared glycine solutions, with little to no observable effect. However, when the glycine solutions were left to 'age' for 24 hours in a sealed syringe, a significant increase in nucleation probability was observed upon irradiation. The 'need' to age the glycine solution had already been discovered previously in research on batch vials. Furthermore, the study, similar to batch studies previously performed, observed a change in crystal morphology with increasing supersaturation [43, 44]. The agreement between microfluidic and batch sample studies further validates the use of microfluidic devices to study NPLIN.

2.3. Considerations

As it stands, application of NPLIN is still limited mainly due to a lack of understanding of the phenomenon itself, as its mechanism has not yet been unveiled. Therefore, it requires further study of the phenomenon and more so the mechanism underlying it. However, study of the phenomenon is largely hindered by the stochastic nature of the process, which requires tedious work to obtain the sizeable amount of data points needed to draw definitive conclusions. Microfluidics offers a well proven solution to overcome this problem, whilst also reducing the resource usage.

Current research utilizes a droplet-based microfluidic system to study the phenomenon. The microfluidic system used in this study was designed to create volume-controlled, stable, supersaturated solution droplets, allowing each and every droplet to act as a separate micro-reactor. Therefore, this device, in contrast with previous research, allows for the gathering of substantial amounts of completely independent data points. Effectively addressing the stochastic nature of the crystallization process, offering a higher reliability of the data and more certainty to its conclusions than the previously published systems.

The goal of this research is to study the effect of laser irradiation on supersaturated aqueous KCl solutions. KCl was chosen based on its affordability and fast acting kinetics, easing study of the phenomenon. This study investigates the effect of well known NPLIN parameters such as supersaturation, laser intensity, laser wavelength on the nucleation probability, thereby aiding in improving understanding of the phenomenon. Furthermore, qualitative comparison of the the results obtained in this study with literature is used to validate the designed microfluidic system. Allowing the system to be used for future research into other NPLIN active compounds, such as glycine, or NPLIN parameters and factors, such as impurities, directly affecting the mechanism.

3

Droplet Based Microfluidic System

A droplet based microfluidic system to study the stochastic nature of NPLIN was developed in a previous study conducted within Eral Lab [16]. The goal of this study was to design a system capable of performing many identical experiments at once in order to generate large data sets for each studied parameter. The result of this study was an initial design of the microfluidic system, the working of which was validated by a number of initial tests. However, the initial tests also highlighted multiple issues and the study proposed a number of improvements in order to minimize the amount of noise, improve the quality and ease analysis of the gathered data. This chapter first highlights the previously designed microfluidic system after which the proposed improvements are presented, tested and discussed. The chapter is ended with a considerations section, offering an overview of the improved microfluidic system and a summary of the improvements.

3.1. Microfluidic System

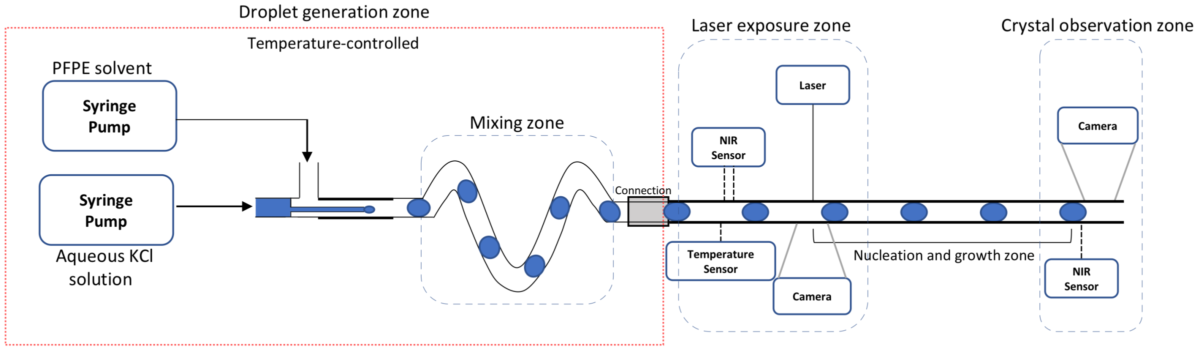

Figure 3.1: A schematic representation of the droplet-based microfluidic system designed in the previous study [16]. The system globally consist of three different zones, the droplet generation zone, the laser exposure zone and the crystal observation zone.

The previously designed droplet-based microfluidic system can be seen in Figure 3.1 and was designed to incorporate both a continuous (Perfluoropolyether oil) and a dispersed phase (aqueous KCl solution) at flow rates of respectively 100 μL/s and 10 μL/s. Both phases were fed into the system by use of syringe pumps connected to platinum-cured silicon tubing.

Each of the coming sections discuss and highlight a different part of the previously designed microfluidic system that can be seen in Figure 3.1. The discussion will go from the input to the output side of the system, first discussing the droplet generation zone and the mixing zone within it, followed by the laser exposure zone and ending with the crystal observation zone. The goals of these subsections is to give the reader a general overview of the system and the problems encountered during its initial testing, followed by the proposed improvements in the next section.

3.1.1. Droplet Generation Zone

The goal of the droplet generation zone is to continuously generate stable KCl solution droplets of constant volume and concentration within the continuous phase, since crystallization is highly dependent on both concentration and volume [16]. Cross-flow and coaxial droplet formation, both depicted in Figure 3.2, are droplet formation methods frequently used in microfluidic systems [89, 90].

Both methods are very similar, with the main difference being the inlet direction of the dispersed phase. In cross-flow droplet formation, the dispersed phase enters perpendicular to the flow whereas in the coaxial droplet formation method it enters in the direction of the flow through a small inner flow channel. The coaxial droplet formation method was implemented in the design, as it offers better visibility of the droplet formation area in comparison to cross-flow droplet formation.

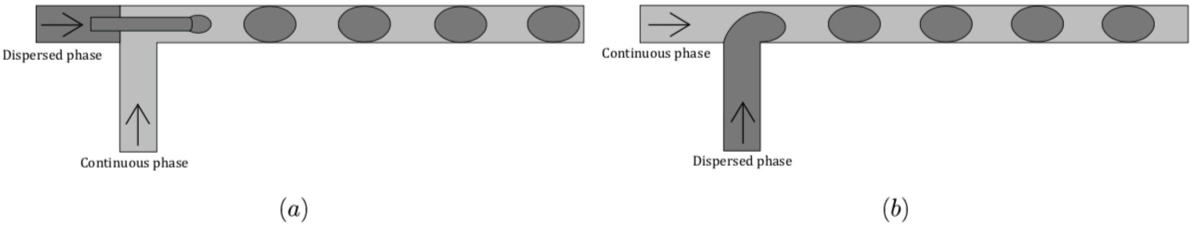

Figure 3.2: Schematic depiction of coaxial flow droplet formation (a) in which the dispersed phase enters in the direction of the flow and cross-flow droplet formation (b) in which the dispersed phase enters perpendicular to the flow [16, 89, 90].

In the designed system coaxial droplet formation is achieved by use of a spherical glass capillary and a T-junction (see Figure 3.3). The capillary was inserted into the tubing coming from the dispersed phase pump and, by use of a ferrule and a microfluidic fitting, secured in place and connected to the T-junction. The continuous phase, connected to the T-junction perpendicular to the inner capillary by use of a ferrule and a microfluidic fitting, flows around the inner capillary and evolves into the coaxial direction. The outlet flow was connected to the T-junction equivalent to both inlets, but the components were fixed by two component epoxy glue as to secure its placement. The adhesive should limit the insertion length of the ferrule into the T-junction, as to avoid compression of the tubing and to ensure the continuous phase can easily flow around the inner capillary.

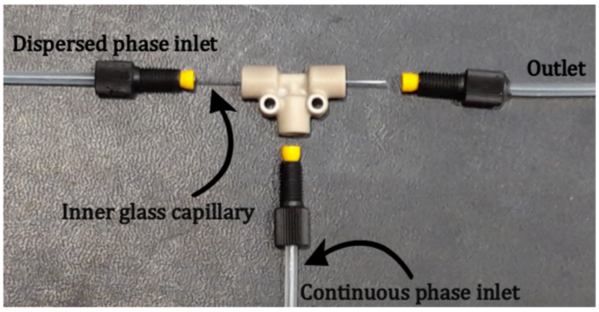

Figure 3.3: The droplet generation section of the previously designed system consisting of a t-junction, several microfluidic fittings (black) and ferrules (yellow), silicon tubing and a 700 μm inner capillary [16].

After the droplets left the T-junction they entered into a mixing zone. Fluid at the tubing wall experiences drag forces, which cause an imbalance in the fluid velocity between the different fluid layers within the droplet. When the droplets move in a straight direction these imbalances are symmetrical, resulting in poorly mixed solutions. Based on the work of Harshe et al., by introducing bends in the fluid direction this symmetry in the velocity field is broken and the fluid mixes [91]. Thus, variations in wall drag forces can be used to facilitate droplet mixing, to ensure the formation of homogeneously concentrated droplets and simultaneously break up any solute clusters potentially present in the droplet solution. Implementing multiple bends, causes the fluid to mix throughout the droplet and ensures a homogeneously concentrated droplet. Based on a study found in literature on the efficiency of droplet mixing, the minimum amount of bends needed to ensure complete mixing was five [16]. In order to compensate for any differences between the designed system and its conditions, the previous study implemented 10 bends. The bends in the system were achieved by fixating the tubing in a 3D printed holder to ensure constant positioning of the tubing and comparability of the results.

The outlet tubing from the mixing zone was connected to a 3D printed connection part required to facilitate a geometry transition of the flow into a square glass capillary before entering the laser exposure zone. This geometric transition was needed to ensure that the confinement material at the laser exposure zone adhered to two main requirements. Firstly, the confinement material cannot interact with the incident laser light. Secondly, the reflection and refraction of the confinement material should be minimized. Square borosilicate glass capillaries meet both these requirements.

The connection part was designed to ensure this geometry change occurred as smooth as possible, as not to disturb the solution and possibly induce nucleation. However, due to errors in the 3D printing process, small ridges on the internal surface of this connection part were present. The past study did not report any undesired nucleation within this connection piece. The lack of undesired nucleation was mainly ascribed to the fact that the droplets flowing through the conversion piece were either undersaturated or at a low supersaturation ratio, but the effects of these ridges are still unknown.

Low supersaturation ratios in the droplet generation zone are needed to avoid crystallization and subsequent clogging of the channel. The low supersaturation ratios were achieved by placing the entire droplet generation zone in a box and controlling its temperature by use of a temperature sensor, a relay, an Arduino Uno microcontroller and a hair dryer. Strict temperature control is not needed within this system, as long as at all locations within the droplet generation zone it is maintained well above room temperature (>35 °C). By altering the relay circuit and optimising the Arduino Uno control unit, it was shown that temperatures deviated from the set point (>40 °C), but throughout the droplet generation zone were maintained well above room temperature.

3.1.2. Laser Exposure Zone

After leaving the 3D printed connection part and entering the square glass capillary, a set of IR sensors as well as a temperature sensor were implemented in the first part of the laser exposure zone. These sensors measured important nucleation-influencing parameters such as droplet volume and temperature. IR sensors were used as a non-invasive measuring technique and combined with an Arduino microcontroller to detect interfaces between the continuous and the dispersed phase, making use of the refracting and reflecting nature of the curved interface between them [92]. Data from this set of IR sensors was used to identify droplets and measure droplet velocity and volume. Furthermore, the live data from the IR sensors, in combination with the Arduino microcontroller, could be used in a laser triggering mechanism to ensure only the droplets are irradiated.

The temperature sensor was used to measure the ambient temperature, which in turn is used to determine droplet supersaturation in the laser exposure zone. The system and control structure of both the IR and temperature sensor was implemented and optimized in the previous study. Furthermore, the ambient temperature measurements were combined with the temperature in the droplet generation zone and a number of aqueous KCl solution dependent parameters to estimate the cooling length of the droplets within the capillary. A key point of the assumptions underlying this estimation, is that they are all related to temperatures, dispersed phase properties and size of the confinement area. The previous study estimated the cooling length to be 12 mm [16]. Comparing the estimated cooling length to a system published in literature by Candida dos Santos et al., in which aqueous solution droplets of comparable sizes were estimated to cool down from 40 to 12.6 °C in less than 10 mm, validated the estimation [88].

After leaving this first part of the laser exposure zone, the droplets were irradiated, 14 cm into the capillary, by an unfocused laser beam from a class 4 Nd-YAG laser (neodymium-doped yttrium aluminum garnet, continuum powerlite DLS 8000). The beam was redirected towards the capillary by use of a number of mirrors, as can be seen in Figure 3.4. In order to prevent damage to the glass capillary or increases in ambient temperature, as well as to decrease the chances of excess heating of the droplets or the continuous phase, the laser beam diameter was decreased from 9 mm to 2 mm by use of an iris. The iris reduces the beam size by only letting through a small mid section of the laser beam, blocking and absorbing the rest of the energy. In the previous study it was found that at the applied laser energies and intensities, this blocking and absorption resulted in significant damage to the iris after already a small number of experiments.

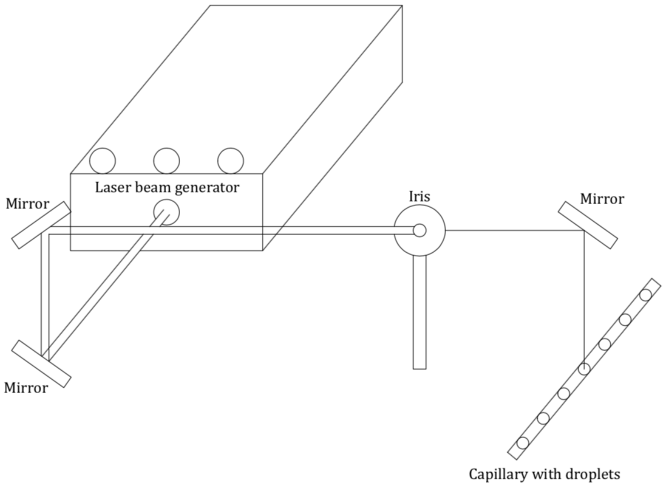

Figure 3.4: Schematic depiction of the laser set-up used in the previously designed system. The laser beam was redirected to the capillary by use of three mirrors and its size was reduced by use of an iris [16].

To further improve the set-up redirecting the laser light shown in Figure 3.4 and increase the degree of control over the system, it was proposed to incorporate a shutter which is further discussed in Section 3.2.4. Incorporation of a shutter combined with an Arduino microcontroller using the mean droplet velocities calculated from the previously mentioned IR sensors could allow the system to only hit the micro droplets and not the continuous phase surrounding it. Further, the shutter would allow control over the number of pulses per droplet. However, shutter and shutter control was difficult to implement due to the high laser powers used in the validation experiments, which would damage the shutter.

3.1.3. Crystal Observation Zone

After the droplets were irradiated by the laser beam in the laser exposure zone, they were monitored and analysed for nucleation and crystal growth in the following crystal observation zone. The crystal observation zone made use of a 4x objective lens and a microscopic camera. It was attempted to implement automated image analysis by use of a machine learning method, in which the first 75% of the data is used to train the algorithm and the last 25% to test the accuracy of the model. However, due to gravity and the forward motion of the droplets, crystals generally end up in the large, thick, dark and curved parts of the droplet interface complicating crystal detection (see Figure 3.5). The thickness of the droplet boundaries were largely accredited to the hydrophobic coating used in the hydrophilic square borosilicate glass capillary, where inconsistencies in the coating could lead to deformation of the droplet interface. As a result of these thick and dark boundaries the automated image analysis model failed to accurately detect the crystals, arriving at nucleation probabilities of roughly one third of those calculated based on manual detection. Therefore, the only method implemented to detect crystals was manual image analysis consisting of the operator manually counting the total number of droplets and number of droplets containing crystals in order to calculate nucleation probabilities.

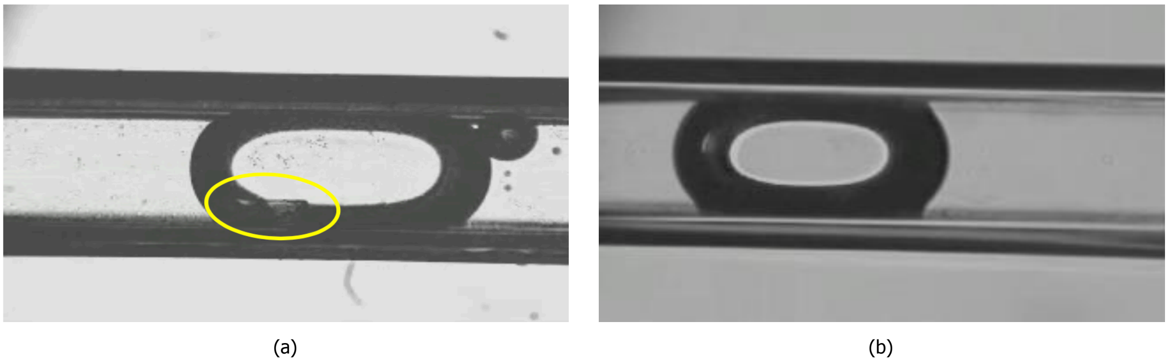
(a) (b)

Figure 3.5: Droplet images obtained from experiments in the previously designed set-up, displaying the thick, dark boundaries around the droplet complicating crystal detection as well as the air bubbles accompanying the solution droplets.

3.1.4. Dimensionless Numbers

The previous study calculated several important dimensionless numbers that can be used to describe the characteristics of droplet flow within the microfluidic system. These dimensionless numbers resemble ratios between the different forces at play and their relative sizes, as to conclude which of these forces significantly affect droplet formation and movement. Information on the relative importance of forces is essential, since the impact of forces in microfluidics, due to the small volumes and length scales, can be significantly different from the macroscopic scale [93]. Dominant forces in microfluidic multi-phase flow are generally viscosity and surface tension [94].

These forces can be characterized by a number of dimensionless numbers, the equations for which can be found in Appendix A.1. Firstly, the Reynolds number, defining the ratio between inertial and viscous forces. If this number is small (<2000), inertial forces dominate and the flow can be considered laminar [95]. Secondly, the capillary number, defining the ratio between the two most important forces in microfluidic flow, interfacial tension and viscosity. When the capillary number is low ($<10^{-5}$), interfacial tension forces were dominant and the droplet's surface area is minimized by forming circular boundaries [89]. In contrast, when the capillary number is high, viscous forces were dominant and droplet deformation can be observed [89]. Thirdly, the Bond number, defining the ratio between gravitational and surface tension effects, which for micro droplets is usually low («1), due to the large surface to volume ratio such that surface tension forces become more important [89, 94]. Finally, the Weber number, defining the ratio of inertia and interfacial tension effects. For micro droplets this number is usually low («1) due to the small size, unless high velocities are used [89].

All of the above-mentioned dimensionless numbers were calculated for the previously designed droplet-based microfluidic system (see Appendix A.1), compared to values expected for microfluidic systems and resulted in the following conclusions. Since the calculated Reynolds number is smaller than 2000, the flow was assumed to be laminar. The calculated Capillary number is small such that interfacial tension effects dominated over viscous effects, which is as expected based on the spherical shape of the formed droplets. The small calculated Bond number confirms that surface area forces dominated over volume forces such as gravity. Finally, the small Weber number indicated that inertial forces cannot be neglected compared to interfacial tension effects.

3.2. Improvements of the Microfluidic System

The system presented in the previous section served as the starting point for this study. Based on the problems encountered in the validation experiments of this system a number of improvements such as altering the continuous phase, altering the tubing used in the droplet formation zone, improving the hydrophobic coating of the capillaries and adjusting the laser directing set-up were put forward. Every section begins with a short paragraph discussing the issues encountered in the previous study, followed by what has been done within this study to solve the issue.

3.2.1. Continuous Phase

The previous study mentioned severe difficulties with vapour bubbles in the continuous phase adhering to the droplets, interfering in the detection and volume estimation of the liquid droplets. After a process of elimination, ruling out the possibility of air entering the system, it was proposed the vapour bubbles in the continuous phase were most likely caused by the continuous Perfluoropolyether oil (PFPE) phase itself. PFPE has a relatively low volatility at room temperature but, at the slightly elevated temperatures in the droplet formation zone, it could still cause the formation of vapour bubbles [96]. A second possible explanation could be the slight dissolving of air in the continuous PFPE phase, resulting in air bubble formation. Therefore, the previous study proposed to alter the continuous phase [16].

The first option considered in this study was silicone oil with a viscosity of 10 cSt, since this closely matches the viscosity of the previously used PFPE oil. The application of silicone oil in microfluidic systems is somewhat limited due to its incompatibility with PDMS, a material commonly used in the fabrication of microfluidic systems [97]. Despite that, numerous example studies of microfluidic systems with water based droplets in silicon oil have shown to be successful [39, 88, 97–99].

The second option considered in this study was Hydrofluoroether oil (HFE), which was previously used within Eral Lab in a study on kidney stones in μ-Reactors [100]. In this study HFE was combined with a surfactant, effectively separating the solution droplets from the continuous phase, minimizing its interaction with the walls of the flow channel. However, the use of a surfactant also offers additional external surface area upon which heterogeneous nucleation could occur [101, 102]. Therefore, the use of HFE would be undesirable, unless it is shown to offer significant benefits. Based on the aforementioned, it was decided to replace the previously used PFPE oil by silicon oil, to avoid the introduction of additional unknown parameters that could affect nucleation.

3.2.2. Droplet Generation Zone Tubing

Alteration of the continuous phase had the indirect consequence that the platinum-cured silicon tubing used in the previous study needed to be altered, since it is commonly known that silicon tubing significantly interacts with silicon oils, causing swelling and clogging of the flow channel [103–105]. Therefore, this study proposed to alter the tubing used in the droplet formation zone to Polytetrafluoroethylene (PTFE) tubing, since it offers superior chemical resistivity and its non-stick proprieties result in a low friction coefficient, allowing the fluid to be transported with minimal resistance [106, 107].

An experiment to test the compatibility of the PTFE tubing with the two newly proposed continuous phase fluids, silicon oil and HFE, and the previously used continuous phase PFPE was performed. For each continuous phase option, six small similarly sized pieces of PTFE tubing were cut, weighed and placed in 1.5 mL glass vials. The vials were filled with the respective continuous phase, closed off using a screw top cap and Parafilm and placed in a 40 °C oven. The first half of the vials was removed after 3 hours and the second half was removed after 24 hours.

Once the vials were removed from the oven, they were opened and the tubing was taken out of the vials. The tubing was wiped with a paper towel, flushed with pressurized nitrogen gas and wiped once more to ensure all solvent was removed from the surface. Afterwards, the tubing was weighed again to determine if any of the continuous phases solubilize in the polymeric matrix of the PTFE tubing. The results can be found in Appendix A.2 and a summary is shown below in Table 3.1. These results show that none of the pieces of tubing have significantly changed in weight, indicating that none of the continuous phase options solubilize the tubing. It can be seen in Table 3.1 that the mass increase for the pieces of tubing soaked in silicon oil for 24 hours is smaller than those soaked in silicon oil for 3 hours, an inconsistency possibly caused by the tarring of the weighing scale in between the different measurements. However, since for all solvent options the results after 3 hours are comparable to those after 24 hours, it was concluded that the PTFE tubing was compatible with all solvent options and it can be assumed that no problems are foreseen with using the tubing for multiple experiments.

Table 3.1: Results of the experiment testing the compatibility of the PTFE tubing with three different solvents, PFPE, silicon oil and HFE, displaying the average mass increase (%) of all pieces of tubing after 3 and 24 hours.

Solvent	**Mass increase after 3 hours (%)**	**Mass increase after 24 hours (%)**
PFPE	0.3686	0.9340
Silicon Oil	0.2221	0.1587
HFE	0.2925	0.9944

3.2.3. Hydrophobization of the Square Capillary

The previously designed system made use of a square 0.9 mm inner diameter borosilicate glass capillary in the laser exposure and crystal observation zone, known to be hydrophilic. In order to minimize the interaction between the droplet and the square capillary, its inner surface was hydrophobically coated. However, as mentioned in Section 3.1.3, data analysis was complicated due to the presence of thick dark boundaries surrounding the droplets. Especially since crystals formed within the droplets would often be located within these dark boundaries. The previous study proposed that the hydrophobic coating (in part) affects the thickness of these boundaries. Furthermore, quality of the hydrophobic coating has been shown to affect droplet stability, spacing between droplets and nucleation probabilities [16]. An improved hydrophobic coating of the capillary could ease crystal detection and improve the quality and reliability of data analysis.

Therefore in this study, two newly found protocols to hydrophobize glass surfaces, which can be found in Appendix A.3, were used to coat the square capillaries and compared to the protocol used in the previous study. The hydrophobization protocol used in the previous study, using trichloro(1H,1H,2H,2H-perfluoroctyl)-silane to hydrophobize the capillaries, serves as a reference point. The second protocol was proposed as an improvement in the previous study and uses a mixture named Aquapell, commonly used to hydrophobically coat car windows [108, 109]. The last protocol was proposed by a fellow Eral Lab member and makes use of a compound similar to the first protocol namely trimethoxy(octadecyl)silane. Trimethoxy(octadecyl)silane has been used before for the coating of superhydrophobic (contact angle > 150 °) textiles and in combination with perylene-diimide to create superhydrophobic, self-cleaning NIR-reflective silica nanoparticles [110, 111]. All three protocols were followed and used to hydrophobically coat three separate capillaries per protocol. To assess the hydrophobicity of the applied coatings and compare amongst the different protocols contact angle measurements were performed as follows.

Each of the capillaries was connected to the droplet generation zone of the previously designed system to generate five completely separated water droplets within it. Subsequently, the capillaries were placed in a Goniometer and graphic analysis of the gathered data yielded contact angle values. Figure 3.6 displays a contact angle measurement performed within the Goniometer controller software. The contact angle is measured by first setting a baseline (green line) for the liquid-solid interface and secondly placing two points in the liquid-gas interface which generates a tangent to the interface (blue line) and allows for calculation of the contact angle between the liquid and the solid phase (red line). In each of the capillaries 5 droplets were generated, for which the contact angle of both interfaces of the droplet were determined, yielding 30 data points per hydrophobization protocol. The averages of the overall data set for all hydrophobization protocols as well as a set of uncoated commercial capillaries can be found in Table 3.2, all detailed measurements can be found in Appendix A.4.2.

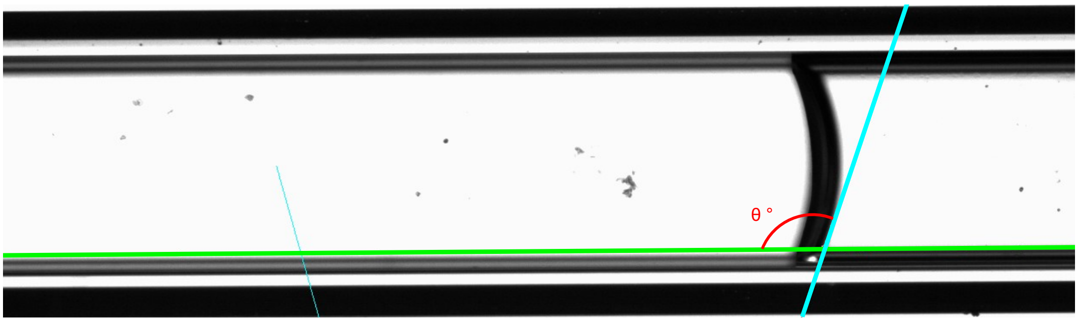

Figure 3.6: Contact angle measurement performed on a capillary coated with 'fresh' Aquapell using a Contact Angle Measurement device. The green line constitutes the base line and the blue line intersecting it is the line adjacent to the liquid-gas interface. The contact angle was measured by determining the angle to the left of the blue interface line (red line).

Table 3.2: Experimentally determined contact angles (in degrees) for different hydrophobisation protocols.

Capillary	**Average Contact Angle (°)**	**Standard deviation (°)**
Unhydrophobized	46.0	8.5
Trichloro-silane	101.6	4.5
Aquapell	104.8	4.1
Trimethoxy-silane	76.1	6.0
Aquapell - Fresh	105.2	4.4

Analysing the results from Table 3.2 shows that the contact angle of an unhydrophobized commercially available capillary is less than 90°, indicating a hydrophilic surface, which is as expected. Contact angles determined from capillaries coated using trichloro(1H,1H,2H,2H-perfluoroctyl)-silane, similar to the previous study, were around 101.6°. Literature on hydrophobic surfaces indicates that in general a surface with a contact angle of around 110° can be considered very hydrophobic [112]. Based on this data, it can be stated that the protocol used in the previous study already shows satisfactory results.

Capillaries coated using Aquapell yielded a slightly higher contact angle, thus potentially improving the hydrophobicity of the capillaries used in the experiment. However, when taking into account the standard deviation of both data sets (entries 2 and 3 of Table 3.2), it can be seen that no definitive distinction between the two protocols can be made. Finally, it is clear that capillaries coated using trimethoxy(octadecyl)silane offer some improvement when compared to unhydrophobized commercially available capillaries. Yet, do not offer comparable or improved performance when compared to the previously used trichloro(1H,1H,2H,2H-perfluoroctyl)-silane.

During preparation of the capillaries it was noted that due to the unavailability of 'fresh' Aquapell, the capillaries used to gather the data for Table 3.2 had to be coated using a previously used Aquapell solution. The previously used solution was stored in a vial sealed under nitrogen, since literature on the use of Aquapell stresses the instability of Aquapell under air [108, 109]. Therefore, it was decided to perform a second set of experiments using a 'fresh' unused Aquapell solution and remeasure the contact angles as described above. The results from this second measurement can be found in the last entry of Table 3.2, but yielded a similar result as the previous measurement. Thus, no clear distinction between capillaries coated with trichloro(1H,1H,2H,2H-perfluoroctyl)-silane and Aquapell could be made.

A number of preliminary measurements were ran for the newly 'improved' system in which both capillaries coated using trichloro(1H,1H,2H,2H-perfluoroctyl)-silane and Aquapell were used. During these preliminary measurements it could be seen that capillaries coated using Aquapell did not offer improved imaging of the droplets or stability of the system. On the contrary, capillaries coated using Aquapell would frequently complicate imaging of the system due to uneven surface coatings. Based on these preliminary measurements, it was decided to not alter the hydrophobic coating of the glass capillaries and use trichloro(1H,1H,2H,2H-perfluoroctyl)-silane in all further measurements.

Hydrophobization equipment - Desiccator

Hydrophobizing capillaries using trichloro(1H,1H,2H,2H-perfluoroctyl)-silane requires a desiccator, which due to the large size of the capillaries was not commercially available and had to be tailored (see Appendix A.5) The previous study reported issues with this improvised desiccator, proposed to affect the quality of the hydrophobic coating. The desiccator was vacuumed and sealed by use of thin rubber tubing (Figure 3.7a), which in the process of vacuuming would, in part due to the 'stickiness' of the trichloro(1H,1H,2H,2H-perfluoroctyl)-silane, collapse and stick together. This prevented the desiccator from reaching its target pressure, which resulted in non- optimal flow of the trichloro(1H,1H,2H,2H-perfluoroctyl)-silane vapour through the capillaries, causing an unequal or imperfect surface coating of the capillaries.

Therefore, within this study the desiccator was further improved by implementation of a microfluidic valve (Figure 3.7b) to regulate the pressure within the desiccator. The valve was combined with tubing connectors and enrolled in Teflon tape to fit within the improvised desiccator outlet. After which all connection points were coated with a black silicone sealant, to ensure sealing of all seems. Overall, this resulted in the improved desiccator to easily reach pressures below 30 mbar and remain at vacuum for over 12 hours. An overall image of the improved desiccator can be found in Appendix A.5.

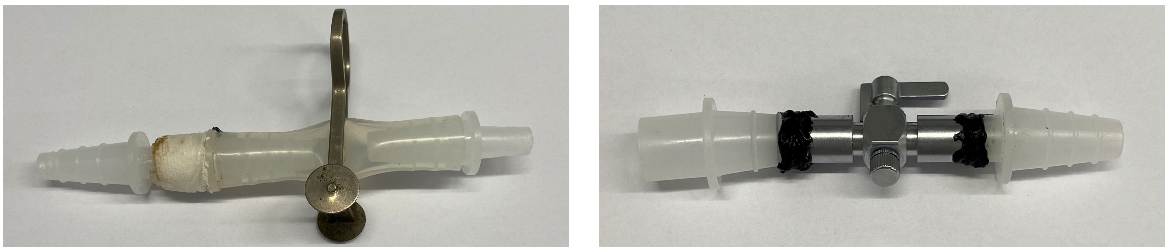

(a) (b)

Figure 3.7: (a) Rubber tubing connection used as a valve system in the improvised desiccator. (b) Microfluidic valve implemented to improve the valve system of the improvised desiccator.

3.2.4. Laser directing system & Shutter Control

The laser used in this study (Nd-YAG,Continuum Powerlite DLS 8000) produces a pulsed laser beam at 10 Hz with a diameter of 9 mm. The laser beam size is considerably larger than the diameter of the square capillary (0.9 mm), yielding the need to reduce its diameter to ensure only one droplet at a time is exposed. The previous study used a system as shown in Figure 3.4, reducing the beam size to 2 mm by use of an iris. An iris reduces the beam size by only letting through a small mid section of the laser beam, blocking and absorbing the rest of the energy. In the previous study it was found that at the applied laser energies and intensities, this blocking and absorption resulted in significant damage to the iris after already a small number of experiments. Therefore, it was proposed to replace the iris by a set of lenses in a telescopic fashion, simultaneously reducing the beam size and intensifying the laser beam. Furthermore, the previous study proposed implementation of a shutter controlled by the IR sensors Arduino, to offer control over the amount of pulses a droplet is exposed to.

A sketch of the new laser directing set-up can be found in Figure 3.8. In this set-up the laser light is redirected towards a set of two lenses by use of a first mirror. The lenses are positioned in a telescopic fashion. In this telescope arrangement reduction of the beam size and intensification of the laser intensity is achieved by converging the light by use of a convex lens. The concave lens is then placed reversely and slightly before the focal point of the convex lens, in order to stop the light from further converging and recreate a parallel beam. The ratio of the focal lengths of the set of lenses will be the intensification factor of the laser beam. Intensifying the laser intensity in the set of lenses allows the laser itself to operate at lower laser powers, thereby reducing the damage incurred by the equipment. Additionally, the new laser set-up offers the ability, for future experiments, to implement a shutter to achieve control over the amount of pulses droplets are exposed to.

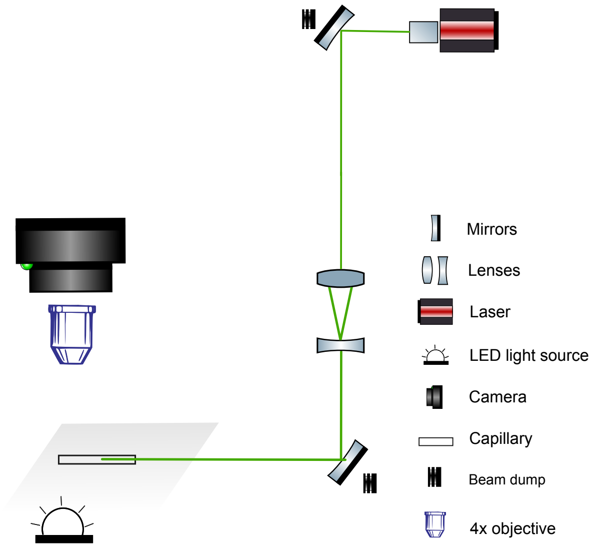

Figure 3.8: Schematic representation of the system used to redirect and intensify the laser beam. The laser is redirect by a first mirror to a set convex and concave lenses which converge and intensify the laser beam. The parallel intensified laser beam is than redirected to the capillary by use of a second mirror.

3.2.5. Droplet Imaging

After changing the continuous phase from PFPE to silicon oil, the thick and dark droplet boundaries seen in the previous study (see Figure 3.9a) had already slightly improved. However, it was desirable to further decrease the thickness of these boundaries, to ease data analysis and increase the chances of success for automated image analysis. It was proposed that the dark boundaries could, in part, be attributed to the light source that was used opposite the microscopic camera to illuminate the droplets. The light acts as a point source which, due to refraction and diffraction from interaction with the capillary glass, could cause these dark boundaries. Thus, it was proposed to implement a light diffuser, as to reduce the amount of refractive and diffractive interaction of the light with the capillary. Implementation of this light diffuser combined with positioning the microscopic camera and 4x objective slightly further from the capillary, had a positive effect on the boundaries (see Figure 3.9b).

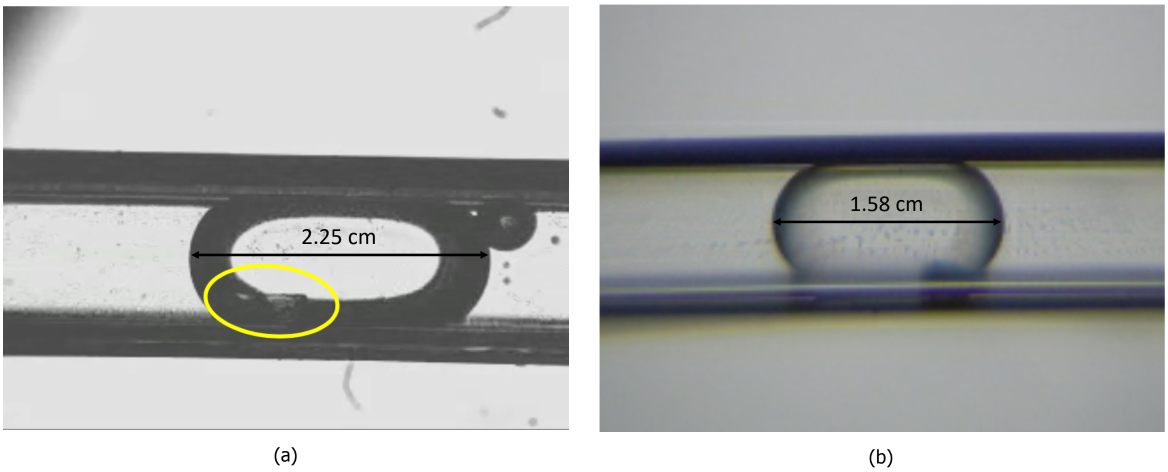

(a) (b)

Figure 3.9: (a) Droplet images obtained from experiments ran with the previously designed set-up, showing thick, dark boundaries around the droplet [16]. (b) Droplet images obtained from experiments ran with the improved system with the altered continuous phase and light diffuser in place, highlighting the lack of thick, dark boundaries around the droplet and thus improved droplet imaging.

3.2.6. Droplet Formation

The droplet volume distribution in the previous study was quite broad, and suffered from a great deal of outliers on both ends of the spectrum. The broad volume distribution was proposed to be caused by droplet coalescence mainly at the transition location between the geometric conversion piece and the square capillary. As a first solution, to reduce the amount of droplets coalescing, the previous study also hydrophobically coated the geometric conversion piece.

In this study, preliminary tests of the improved system, with the new tubing, continuous phase and coating of both the capillary and conversion piece, still encountered the issue of droplet coalescence. Droplets formed at the inner capillary were seen to enter and stick to the geometric conversion piece until a second or third droplet adjoined, after which the combined droplet moved further through the system. Coalescence of droplets after the point of formation is undesired, since it combines separate droplet volumes and therefore inhibits the generation of truly independent samples. However, the preliminary tests also encountered a new issue in the form of severe leakage around geometric conversion piece, an issue proposed to be caused by the change of continuous phase.

Based on the issues encountered in the preliminary tests, it was proposed to completely eliminate the geometric conversion piece from the system. As to reduce the amount of droplet coalescence and eliminate its unknown effects on the nucleation probability. Instead, the system would generate the droplets directly within the square capillary, similar to a study previously conducted within Eral Lab [113]. A schematic depiction of this droplet formation method can can be seen in Figure 3.10. The tip of the square capillary is coated with a small piece of silicon tubing and directly connected to the T-junction, by use of a ferule and a microfluidic fitting. The small inner capillary is directly inserted into the square capillary, such that the droplets are still generated according to the coaxial droplet formation method. Generation of droplets using this formation method would have the added benefit of almost completely removing the chance of droplet coalescence. Hopefully, narrowing the droplet volume distribution and minimizing outliers. Furthermore, it would allow for the generation of truly independent droplet volumes and thus samples, eliminate the unknown effect of the geometric conversion piece on the nucleation probability and improve the reliability of the system by reducing the risk of leakages throughout the system but mainly at the geometric conversion piece.

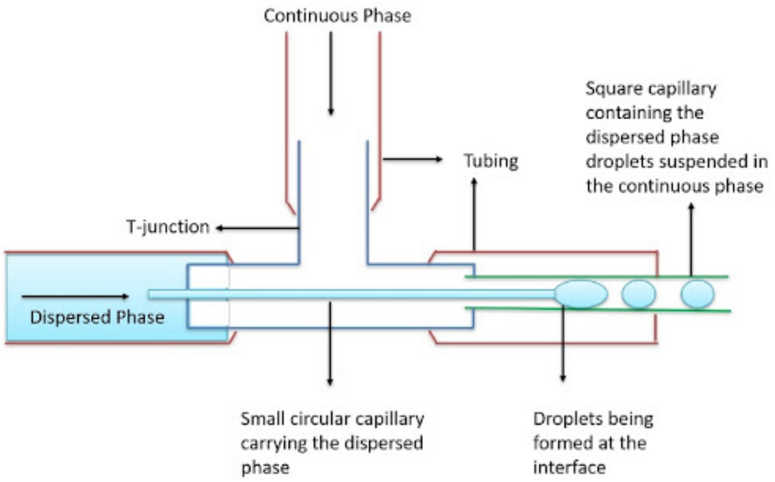

Figure 3.10: Schematic depiction of the co-axial droplet formation within the glass capillary [113]. This droplet formation method directly joins the square glass capillary in the T-junction used for co-axial droplet formation by use of a small piece of flexible tubing, removing the need for any other geometric conversion connections.

Mixing Zone

Implementation of the above-mentioned new droplet formation method would mean droplets are no longer mixed after generation. Mixing is essential to homogenize solute concentration throughout the droplet and break up any potential solute clusters present within the droplet that could affect nucleation [19, 49]. It was proposed to implement the same mixing zone, consisting of the static bends, in the improved system by directly connecting it to the dispersed phase syringe and mixing the dispersed phase solution before droplet generation within the capillary. The working of such passive mixing in a serpentine micro channel for laminar flows has been demonstrated in a number of studies, but had not been proven for the system at hand [114–116].

In order to demonstrate the working of the mixing zone it was decided to directly join two aqueous streams, one consisting of pure water and one of water mixed with a dye, in a Y-junction by use of a ferule and a microfluidic fitting, and monitor the output of the system. In the control experiment, the output of the Y-junction was directly imaged (Figure 3.11a). It displayed a clear two layer system, indicating that no mixing was achieved in the Y-junction. In the second experiment, the output of the Y-junction was connected to the mixing zone and the output of the mixing zone was imaged (Figure 3.11b). A clear two layer system is no longer visible but a uniform light blue stream was formed, indicating that the mixing zone is working effectively and joining both input streams.

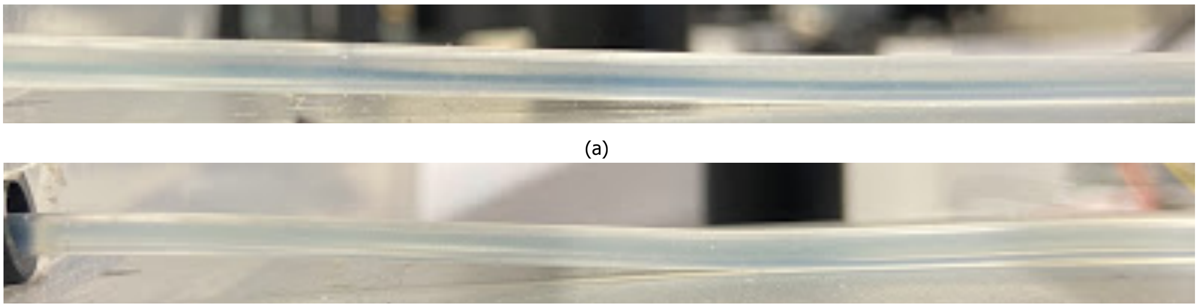

(a)

(b)

Figure 3.11: (a) Output stream of two streams, one consisting of pure water and one consisting of water with a dye, joined in a Y-junction without mixing. A clear two layer system is visible in the output stream, indicating no significant mixing has taken place. (b) Output stream of the mixing zone after receiving the input from the two aqueous solutions seen in Figure 3.11a. A clear two layer system between the two joined solutions can no longer be seen

In case of the adjusted microfluidic system, this would mean that the aqueous KCl solution that is fed to the mixing zone is properly mixed, and any solute clusters potentially present within it are broken up, before the solution reaches the T-junction and droplet formation takes place. Thus, each and every droplet generated should be properly homogenized. Furthermore, it is essential to ensure that any disturbance caused by the sudden geometric conversion of the dispersed phase, from the circular inner capillary to the square outer capillary, that could potentially induce nucleation is minimized in the systems output. This is accomplished by placing the point of droplet generation 3-4 cm into the temperature controlled environment, which ensures the droplet solution remains undersaturated at the point of droplet formation so that no nucleation is induced.

Droplet Size Distribution

Droplet size distributions obtained from experiments conducted using the newly proposed droplet formation method can be seen in Figure 3.12. It can be seen that the size distributions are narrower than in the previous system and suffer less from outliers. The decreased presence of outliers is most probably caused by the reduced presence of droplet coalescence within the system. The reduced presence of coalesced droplets was confirmed by visual inspection of the system during the experiments, observing no significant droplet coalescence taking place within the capillary. The overall narrower droplet size distribution introduces less variability within the system, improving comparability between measurements and reducing the effect of volume variations on nucleation probability. Furthermore, the droplet size distributions also show that the droplets formed in the new improved system are of a significantly smaller size, roughly 40 - 60 % of the size in the previous system. The reduced size will have a significant effect on the nucleation probability observed within the system, since it is known that the (laser exposed) volume has a significant effect on nucleation probability [55].

Based on the narrower droplet size distribution, reduced chances of droplet coalescence and possibility to remove the unknown effect of the geometric conversion piece on nucleation probability it was decided to implement the new droplet formation method.

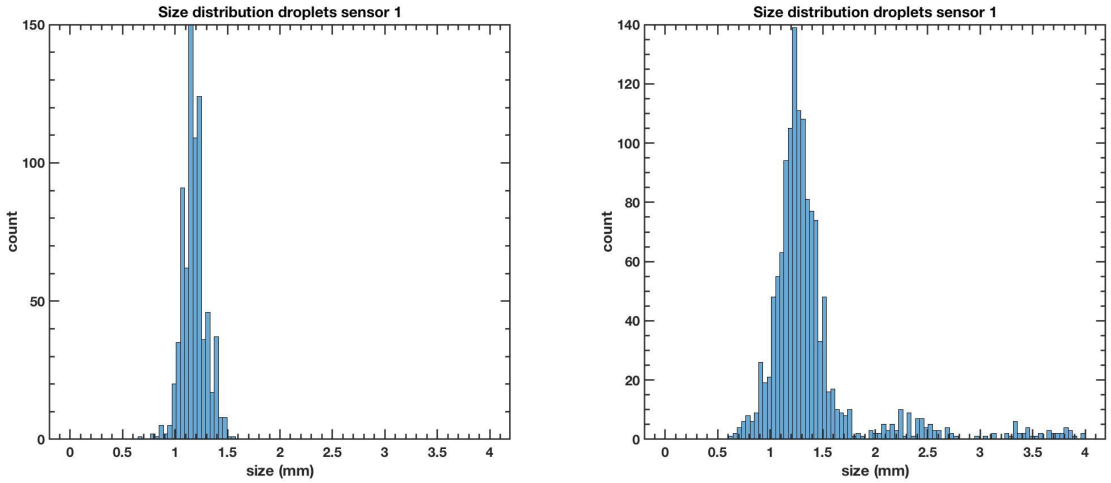

(a) (b)

Figure 3.12: Droplet size distributions obtained from IR sensor data in the improved microfluidic system using the new droplet formation method during (a) a laser irradiation experiment and (b) a control experiment.

3.3. Considerations

This section presents a schematic overview of the improved droplet based microfluidic system (Figure 3.13) that was used for the experiments presented and discussed in the following chapters. Followed by a small summary of changes made to the original system. An image of the overall microfluidic system can also be found in Appendix A.6.

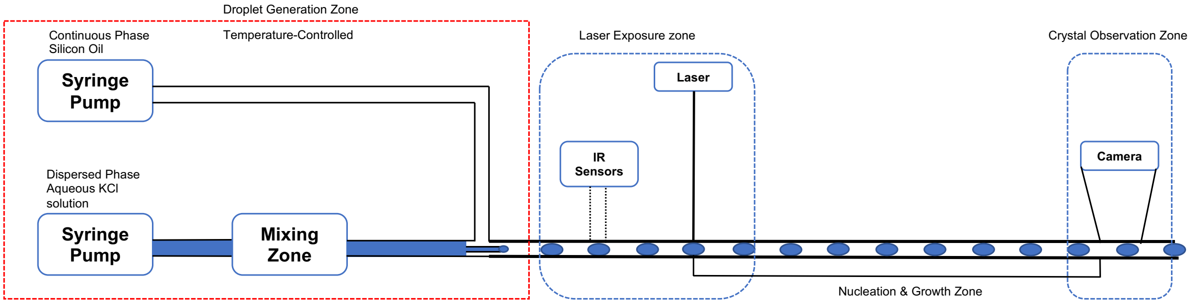

Figure 3.13: A schematic representation of the improved droplet-based microfluidic system after implementation of the improvements presented in this chapter using Figure 3.1 as a basis. The system consists of three different zones, the droplet generation zone, the laser exposure zone and the crystal observation zone, however the system of the droplet generation zone and its components have changed as compared to Figure 3.1.

3.3.1. Droplet Generation Zone

Optimization of the droplet volume distribution was achieved by alteration of the continuous phase, the tubing and the droplet formation method. Droplet formation now takes place directly within the square capillary, with reduced droplet coalescence within the system as a direct effect. Droplet formation takes place 3-4 cm from the wall of the temperature controlled environment, to ensure undersaturation at the point of droplet formation as to avoid inducing nucleation. The dispersed KCl solution is mixed before droplet generation, to ensure the solution is properly homogenized.

3.3.2. Laser Exposure Zone

In the laser directing set-up (Figure 3.8), the iris was replaced by a set of lenses positioned in a telescopic fashion. The set of lenses simultaneously reduce the beam size and intensify the laser intensity, allowing the laser to operate at lower laser powers. The result of this, is a reduction in the amount of damage incurred by the laser directing equipment and the possibility to implement control over the amount of pulses droplets are exposed to.

3.3.3. Crystal Observation Zone

Implementation of the new continuous phase already showed an improvement in the droplet imaging. Nevertheless, the quality of the droplet images in the crystal observation zone was further improved by implementation of a light diffuser in between the white led light and the camera combined with a slight re-positioning of the microscopic camera and 4x objective.

Additionally, equipment used to hydrophobically coat the square glass capillaries was improved, which resulted in a more consistent and higher quality of coating.

3.3.4. Dimensionless Numbers & Cooling Length

The dimensionless numbers for the improved system were calculated (see Appendix A.1 for the results). Despite all changes made to the system throughout this study, the dimensionless numbers remain unaltered. This is as expected based on the fact that almost all dimensionless numbers used to characterize the microfluidic system are only dependent on dispersed phase parameters or mean droplet velocities, neither of which have been significantly altered by the changes made.

A similar conclusion was reached for the cooling length, since none of the parameters used in and assumptions underlying the calculation have been significantly altered by the improvements, the cooling length is proposed to remain unaltered. For a detailed calculation the reader is directed to the previous study [16].

4

Laser Irradiation Experiments

The microfluidic system described and improved in the previous chapter was used to study NPLIN as a function of its affecting parameters, supersaturation, laser wavelength and laser intensity, and determine their effects on the nucleation probability. Table 4.1 offers an overview of the experimental conditions for all experiments. The microfluidic system used either a 1.05 or 1.10 supersaturated aqueous KCl solution as the dispersed phase fluid to test the effects of the laser, as well as supersaturation, on the nucleation probability. The preparation and storage procedure for the supersaturated solutions together with the KCl and water quantities used to prepare the supersaturated solutions can be found in Appendix B.1.1. For each of these supersaturated solutions control cooling experiments were performed to serve as a reference for the laser irradiation experiments. The experimental protocol for starting and running the microfluidic system in all experiments can be found in Appendix B.1.2. In the laser irradiation experiments the solutions were irradiated with a laser beam 8 cm after droplet generation in the temperature controlled environment. Commonly used laser wavelengths for NPLIN are 1064, 532 and 355 nm and each of them was used to investigate the effects of laser wavelength on the nucleation probability. Four different laser intensities (10, 25, 50 and 100 MW/cm^2) were tested at each wavelength. However, for the 355 nm wavelength performing measurements at 100 MW/cm^2 proved to be impossible, due to severe damage to the capillary. Therefore the maximum applied laser intensity for the 355 nm wavelength was 70 MW/cm^2, further elaborated on in Section 4.1.4. Calculations for the laser intensities can be found in Appendix B.2.

After the droplets were irradiated they were allowed to travel in the capillary for 16 cm, where they were then imaged. Images taken during all experiments were analyzed by manual image analysis to determine the number of droplets and calculate the nucleation probability. In this chapter, first the effect of laser intensity on nucleation probability is discussed, displaying the observed nucleation probabilities at each of the laser wavelengths separately. Second, a discussion on the influence of laser wavelength on the nucleation probability is presented, displaying a combined figure of the nucleation probability (-) vs laser intensity (MW/cm^2) for all wavelengths, to determine if the values are comparable. Third, the effect of supersaturation on the nucleation probability is inspected by comparing the nucleation probabilities observed for both S = 1.05 and S = 1.10 amongst each other. Fourth, a comparative analysis for the results with studies found in literature is offered. Fifth, the chapter is ended with a considerations section summarizing the results.

Table 4.1: Overview of experimental conditions used during laser irradiation experiments varying supersaturation, laser wavelength and laser intensity.

Experimental condition	Value	Unit
Dispersed phase fluid	Aqueous KCL solutions	
Dispersed phase flow rate	10	μL/min
Continuous phase fluid	10 cSt Silicone oil	
Continuous phase flow rate	100	μL/min
Supersaturation ratios (S)	1.05, 1.10	
Laser wavelengths	1064, 532, 355	nm
Laser diameter	1.35	mm
Laser intensity	0, 10, 25, 50, 70, 100	MW/cm^2
Laser frequency	10	Hz

Normalization of the Data

As the data obtained in both the control cooling and laser irradiation experiments has shown, most parameters (directly) influencing nucleation probability, supersaturation and induction time, remained relatively constant between measurements. However, major variations of volume were observed, with the smallest average volume equal to approximately 52% of the largest average volume. As nucleation probability is known to be highly dependent on volume [41, 55], it was decided that, to ensure comparability between different measurements, corrections for these volume differences needed to be performed. Fortunately, both nucleation models predict a directly proportional relationship between nucleation probability and volume. Some studies show this directly proportional relationship to fail for small volumes (pL) [18]. Explanations offered for this observation were that in small volumes, cluster formation can have a significant impact on the bulk solute concentration, and thus the bulk supersaturation. Therefore, inhibiting the growth of clusters beyond the critical radius. Nevertheless, as the volumes used in this study are orders of magnitude larger (μL), and studies by Fang et al. have shown the validity of this relationship [55], it was decided to normalize the observed nucleation probabilities for volume differences by use of this directly proportional relationship to the largest observed volume.

4.1. Effect of Laser Intensity on Nucleation Probability

The coming sections present a small subset of all parameters characterizing the experiments, a complete overview of all data can be found in Appendix B.3 for the control cooling experiments and Appendix B.4 for the laser irradiation experiments. First the results obtained in control cooling experiments are presented, followed by the results of laser irradiation with 1064 nm, than with 532 nm and ending with the results of irradiation with 355 nm. The results of irradiation experiments show the volume distribution and pulses per droplet distribution of the different measurements, paired with a graphic display of nucleation probability, both observed and normalized, (-) vs laser intensity (MW/cm^2).

4.1.1. Control Cooling Experiments

In Table 4.2 the average results of all control cooling experiments are presented. The values are based on an average of three separately performed cooling experiments, detailed data of these measurements can be found in Appendix B.3. It can be seen that the average supersaturations are centered around the target values with a relatively small standard deviation, thus implying the values did not vary significantly between measurements. Similarly, the mean velocities, directly impacting the detection time, have a small standard deviation. In addition, the mean volume did not significantly differ between the separate cooling experiments and was used to normalize the observed nucleation probabilities.

The number of droplets (N) in each experiment is of essential use, since it is directly related to the error in the observed nucleation probability. As it is known that, according to statistics, the error in the data set is inversely proportional to $\sqrt{N}$. Therefore, it was desired to ensure all data sets consisted of over a thousand droplets to achieve statistical significance of the results. Finally, the nucleation probabilities shown in Table 4.2, both observed and normalized for volume, are included as a fixed line in the graphic displays of nucleation probability (-) vs laser intensity (MW/cm^2) in the coming sections. They will serve as a reference for the laser irradiation experiments.

The average nucleation probability obtained in cooling experiments is displayed as a fixed blue line. Whereas a fixed red line is used to display the average nucleation probability obtained in cooling experiments after normalizing the volume. The errors in these nucleation probabilities have also been taken into account by portraying them as dashed blue and red lines. The dashed lines mark the upper and lower bound of the probabilities obtained in cooling experiments. However, in almost all displays the dashed blue lines, portraying the upper and lowers bounds of the nucleation probability directly observed in cooling experiments, are practically none observable. As the error in these observation are virtually none existent due to the large employed data set. In the coming sections, the effectiveness of laser irradiation is measured by its ability to increase the nucleation probability as compared to the value obtained in the control cooling experiments.

Table 4.2: Average results of control cooling experiments conducted on droplets of S = 1.05 & 1.10 KCl solutions.

Supersaturation	**Mean velocity (mm/s)**	**Mean Volume (μL)**	**Number of droplets**	**Nucleation probability**	**Nucleation probability normalized volume**
1.0534 ± 0.0011	2.4230 ± 0.0881	0.9299 ± 0.0807	1417	0.00924 ± 0.00001	0.01570 ± 0.00134
1.1046 ± 0.0017	2.3947 ± 0.1011	1.0089 ± 0.1068	1241	0.02551 ± 0.00001	0.04054 ± 0.00477

4.1.2. 1064 nM

1.05 Supersaturated Solutions

In Figure 4.1a the volume distribution for S = 1.05 droplets irradiated by 1064 nm light is displayed. It can be seen that, except for the volume in the 25 MW/cm^2 experiment, the volumes are comparable and all error bars overlap. However, as the difference is small, it is not expected that volume had a significant effect on the nucleation probabilities observed, such that the trend in normalized probabilities should be equivalent to the trend in the observed nucleation probabilities. A trend similar to that seen in the volume distribution can be observed in Figure 4.1b for the number of laser pulses per droplet. Although literature has shown that the amount of laser pulses per sample does not have a significant effect on the observed nucleation probability, ensuring its comparability between measurements ensures that the observed effect can be fully ascribed to the applied variation in laser intensity [41, 64, 77].

The nucleation probability (-) vs laser intensity (MW/cm^2) is displayed in Figure 4.1c. Inspecting the observed nucleation probability, it can be seen that laser irradiation at 10 MW/cm^2 initially results in a small decrease in the nucleation probability. The decrease is followed by significant increases in the nucleation probability upon further increasing the laser intensity. Therefore, laser irradiation with intensities higher than 25 MW/cm^2 seems to have a positive effect on nucleation probability, since the observed probabilities exceed the nucleation probability obtained in control cooling experiments. A similar trend is seen for the normalized nucleation probability, which was expected since all measurements made use of relatively comparable volumes.

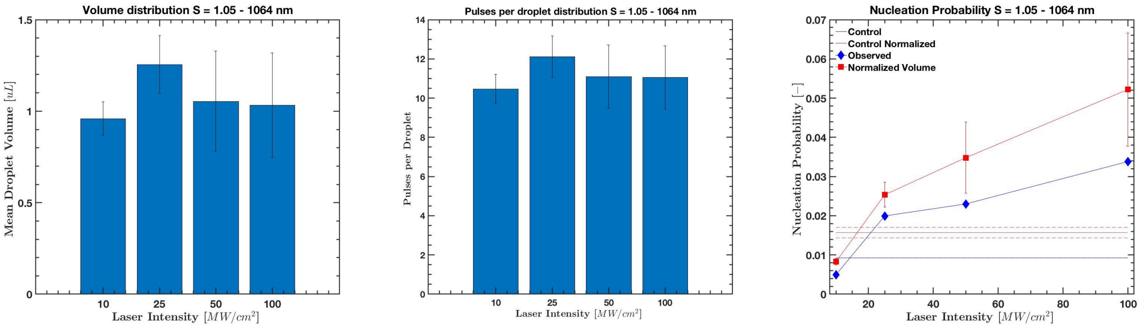

(a) (b) (c)

Figure 4.1: (a) Droplet volumes, (b) Laser pulses per droplet and (c) Nucleation probability (-) vs laser intensity (MW/cm^2) for S = 1.05 droplets irradiated by 1064 nm light as well as the average nucleation probability from the control cooling experiments.

The initial decrease in nucleation probability upon irradiation by 1064 nm light at 10 MW/cm^2 could be explained by partial heating of the solution, and the accompanying reduction in supersaturation, by the light. As it is known, water has a slight absorption band at 1064 nm [117]. However, research previously performed within Eral Lab by Irimia et al. and Dhingra on batch samples have shown these temperature effects to be minimal [47, 77]. Therefore, partial heating of the solution due to absorption of the light is most probably not the cause of this observation. A more likely explanation might be found in the Nanoparticle Heating model. The model is based around the rapid heating of nanoparticles, presumably causing the formation of a small vapour cavity, analogue to laser induced cavitation, around which the solute might be less well solvated [118]. Nevertheless, as the nanoparticles absorb the energy, it results in a rapid temperature increase in the surrounding solution, temporarily reducing the local supersaturation. In the 10 MW/cm^2 measurement, the applied energy could not be large enough so that the dynamics might stop here, before the solution temperature reaches its vaporization temperature and causes the formation of a vapour cavity [62, 70, 118].

Within this study the entire solution is irradiated, therefore nanoparticles throughout the entire droplet are heated. The result of which could be the significantly lower nucleation probability observed at 10 MW/cm^2. As the effect is not observed upon irradiation at higher laser intensities, it might imply irradiation at 10 MW/cm^2 occurred below a laser intensity threshold for NPLIN to be effective. Previous research by Alexander et al. on batch samples found the existence of such a threshold and indicated its value to be practically supersaturation independent at 6.4 ± 0.5 MW/cm^2 [64]. Nevertheless, upon closer inspection of their data it can be seen that these values could, when taking the errors of the separate measurements into account, vary between 2 and 12 MW/cm^2. This observation might offer some support for the explanation that the 10 MW/cm^2 experiment was performed below the laser intensity threshold. Though, this would be in contrast with previous studies performed within Eral Lab on batch irradiation of S = 1.035, 1.049 and 1.055 KCl solutions [30, 47]. These studies found the threshold value to be around 0.5 MW/cm^2 and observed 100 % nucleation at laser intensity values above 5 MW/cm^2. However, it must be noted that the dynamics in a batch scale experiment might differ significantly from the effects observed on the microfluidic scale. As the microfluidic scale employs much smaller volumes and detection times and deals with irradiation of the entire solution volume as opposed to irradiation of partial volumes in batch experiments.

1.10 Supersaturated Solutions

The volume distribution for S = 1.10 droplets irradiated by 1064 nm light is displayed in Figure 4.2a. The distribution shows that even though the volumes vary, all error bars overlap. Therefore, all volumes were relatively comparable such that they should not have had a significant effect on the trend observed in the nucleation probability vs laser intensity display, but could offer explanation for small differences observed. Notable is the large volume deviation in the 10 MW/cm^2 experiment, which will strongly propagate into the error observed in the normalized nucleation probability. A similar trend is observed in Figure 4.2b for the number of laser pulses per droplet. Hence, the number of laser pulses per droplet was considered comparable for all measurements.

Analyzing the observed nucleation probability in Figure 4.2c, it can be seen that laser irradiation at all intensities seems to have been beneficial for the nucleation probability. Irradiation at all laser intensities offered an increased nucleation probability, in comparison to the control cooling experiments. However, the increase in nucleation probability between irradiation with laser intensities of 25, 50 and 100 MW/cm^2 seemed to have been small, possibly indicating a saturation intensity above which increasing the laser intensity no longer has a direct effect on the nucleation probability.

The normalized nucleation probability in Figure 4.2c suggests similar trends. Yet, it can no longer be said with certainty that irradiation at 10 MW/cm^2 offered an increased nucleation probability, in comparison to the control experiments, since these values now overlap due to the large error in this observation. Further, even though the increases in nucleation probability between 25, 50 and 100 MW/cm^2 now seem larger, the shape of the peak still strongly suggests some form of saturation effect. These observations are in agreement with previous research conducted on batch samples within Eral Lab on S = 1.035, 1.049 and 1.055 KCl solutions, which observed a saturation effect for the nucleation probability at applied laser intensities above 5 MW/cm^2 [30, 47].

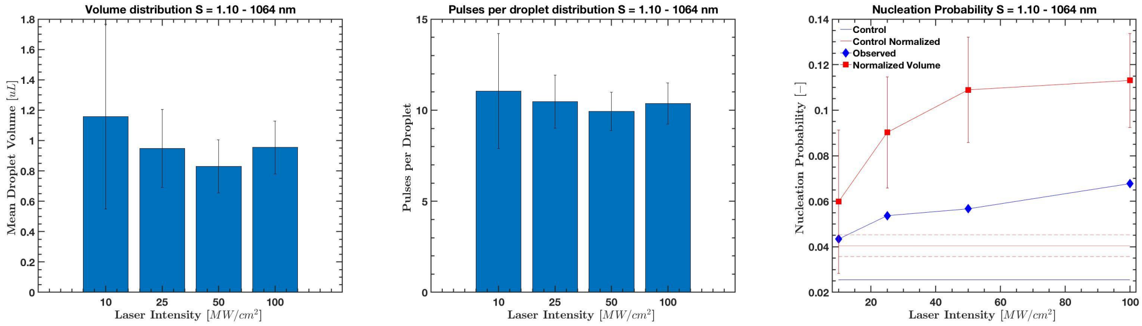

(a) (b) (c)

Figure 4.2: (a) Droplet volumes, (b) Laser pulses per droplet and (c) Nucleation probability (-) vs laser intensity (MW/cm^2) for S = 1.10 droplets irradiated by 1064 nm light as well as the average nucleation probability from the control cooling experiments.

4.1.3. 532 nM

1.05 Supersaturated Solutions

In Figure 4.3a, the volume can be seen to vary considerably between measurements as not all error bars overlap. Hence, volume effects are expected to affect the observed nucleation probability. Notable is the large volume volume observed in the 50 MW/cm^2 measurement, constituting the largest observed volume amongst all measurements. All nucleation probabilities are normalized to this volume, consequently its normalized nucleation probability does not differ from the observed nucleation probability. A similar trend is observed in Figure 4.3b for the number of laser pulses per droplet. The measurements can not be considered comparable, as not all error bars overlap.

In Figure 4.3c the nucleation probability vs laser intensity is displayed. For the observed nucleation probability, it can be seen that laser irradiation at 10 MW/cm^2 initially results in a small decrease in the nucleation probability. The initial decrease was followed by a significant increase in the nucleation probability upon irradiation at 25 MW/cm^2, offering a slight improvement over the cooling experiment. When the laser intensity was further increased to 50 MW/cm^2, the beneficial effect on the nucleation probability was more apparent. Unexpectedly, the nucleation probability seems to decrease upon further increasing the laser intensity, possibly indicating an adverse effect of increasing the laser intensity.

However, when analyzing the normalized nucleation probability it becomes apparent that volume effects could have played a role in these observations. On the lower end of the laser intensity spectrum, the nucleation probability can still be seen to decrease upon irradiation and the slight increase in nucleation probability at 25 MW/cm^2 can no longer be ascribed with certainty to laser irradiation. Additionally, the nucleation probability can now be seen to increase when increasing the laser intensity from 50 to 100 MW/cm^2. Yet, there is no clear distinction between these values as their error bars overlap. Overall, irradiation at higher laser intensities is seen to increase the nucleation probability.

The initial decrease in nucleation probability upon irradiation with 532 nm is slightly more apparent than at 1064 nm. Yet, at this wavelength it can not be ascribed to temperature increases caused by the absorption of light, since it is known that water is little to none absorbent at this wavelength [117]. Results for 532 nm at 10 MW/cm^2 corroborate with the observations seen for 1064 nm, which further support the nanoparticle heating explanation put forward in Section 4.1.2. Still, the none observed NPLIN effect at 25 MW/cm^2 fails to be fully encompassed by that explanation, since all previous studies posted in literature have demonstrated threshold intensities far below this value [30, 41, 47, 64]. A discrepancy possibly explained by the much smaller volumes employed in this study [55].

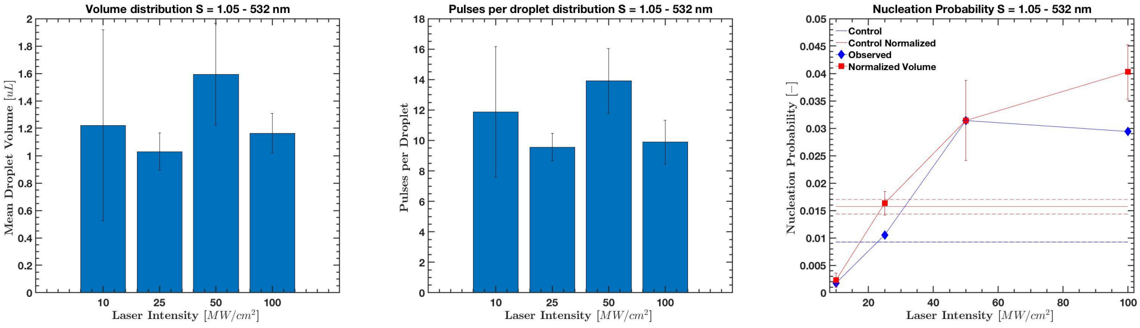

(a) (b) (c)

Figure 4.3: (a) Droplet volumes, (b) Laser pulses per droplet and (c) Nucleation probability (-) vs laser intensity (MW/cm^2) for S = 1.05 droplets irradiated by 532 nm light as well as the average nucleation probability from the control cooling experiments.

1.10 Supersaturated Solutions

The volume distribution for S = 1.10 droplets irradiated by 532 nm light in Figure 4.4a displays significant variations in volume, as most of the error bars do not overlap. Especially the volume from the 25 MW/cm^2 measurement differs significantly from the others. Hence, volume is expected to affect the nucleation probabilities directly observed within the system. The variations observed in the number of laser pulses per droplet (Figure 4.4b), are smaller than those observed in the volume distribution and, as nearly all error bars touch, can be considered comparable.

Analyzing the observed nucleation probability in Figure 4.4c, it is clear that laser irradiation at all intensities offered an increased nucleation probability, as compared to the control cooling experiments. The apparent decrease in nucleation probability when increasing the laser intensity from 25 to 50 MW/cm^2 is noteworthy, since nucleation probability is expected to increase with increasing laser intensity. The decrease was followed by an increase in nucleation probability as the laser intensity was further increased to 100 MW/cm^2. Yet, these observations could have been caused by volume differences, since the volumes seen in Figure 4.4a were deemed incomparable.

When inspecting the normalized nucleation probability, the reduction in nucleation probability upon irradiation with 50 MW/cm^2 can be seen to vanish. At all intensities, nucleation probability is still enhanced when compared to the control cooling experiment. In contrast to the directly observed nucleation probabilities, a decrease in nucleation probability is no longer seen upon increasing the laser intensity from 25 to 50 MW/cm^2. Consequently, the proposition that the previous observation was caused by volume effects seems correct. However, a clear distinction between the nucleation probabilities obtained at 50 and 100 MW/cm^2 can no longer be made, as the error bar in the latter is substantially larger. Overall, the normalized data suggests a linear relationship between nucleation probability and laser intensity, an observation in line with literature [15, 41, 64].

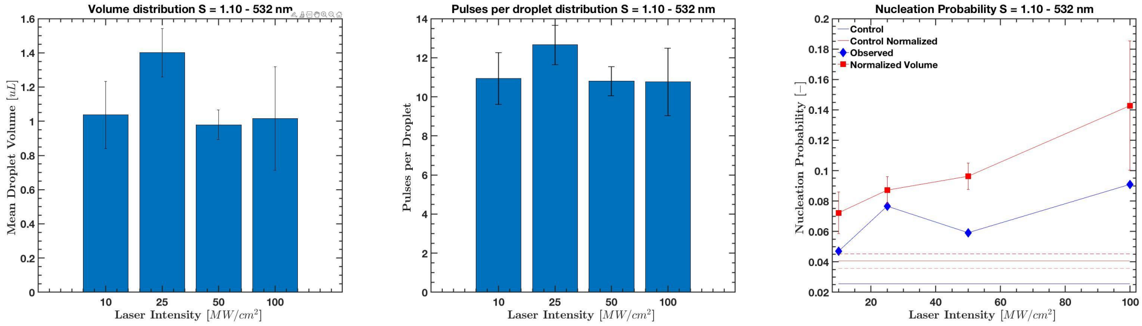

(a) (b) (c)

Figure 4.4: (a) Droplet volumes, (b) Laser pulses per droplet and (c) Nucleation probability (-) vs laser intensity (MW/cm^2) for S = 1.10 droplets irradiated by 532 nm light as well as the average nucleation probability from the control cooling experiments.

4.1.4. 355 nM

Irradiation with 355 nm proved to be less straightforward than with 1064 and 532 nm. Whereas with 1064 and 532 nm it was possible to irradiate the square borosilicate capillaries with laser intensities up to 100 MW/cm^2 for a prolonged period of time (up to 2 - 2.5 hours generally). At 355 nm, irradiation above 70 MW/cm^2 resulted in pierced and broken capillaries within 10 - 20 minutes. Even at 50 and 70 MW/cm^2 capillaries would sometimes only withstand irradiation for 1 - 1.5 hours. These observations severely complicated data collection at these higher laser intensity values, resulting in the highest applied laser intensity for 355 nm to be 70 MW/cm^2.

Explanations for these observations were sought in the (slight) absorption of the 355 nm light by the square borosilicate capillary. Support for this was found by the visual inspection of the glass capillaries during measurements, where the laser spot was relatively visible on the capillary as well as the borosilicate lenses used in the laser directing set-up. A transmission spectrum for the capillaries was obtained from the manufacturer (See Appendix B.5). Although the data provided was for a capillary with a thicker (1 mm vs 0.180 mm) wall, it was seen that the transmission did not vary strongly with wall thickness. The spectrum indicated that the material is highly transparent to both 1064 and 532 nm, but this transparency starts to drop around 350 nm. Therefore, the 355 nm wavelength is on the edge of transparency and partial absorption and reflections could thus explain these observations. Further explanations were offered in the higher individual photon energy of 355 nm damaging the capillary, multi-photon absorption or non-linear absorption of the capillary at this wavelength.

The remainder of this section first presents the results of laser irradiation experiments conducted on 1.05 supersaturated solutions with 355 nm, followed by the results obtained upon irradiation of 1.10 supersaturated solutions with 355 nm.

1.05 Supersaturated Solutions

The volume distribution for S = 1.05 droplets irradiated by 355 nm light in Figure 4.5a, shows that the volumes of all measurements were not comparable, as not all error bars overlap. Hence, slight volume effects could play a role in the observed nucleation probability. The relatively large volume deviation in the 70 MW/cm^2 measurement is noteworthy, since it will strongly propagate into the error observed in the normalized nucleation probability. The number of laser pulses per droplet distribution in Figure 4.5b shows that all error bars overlap, thus all measurements can be considered comparable.

Figure 4.5c displays the nucleation probability vs laser intensity. Inspecting the observed nucleation probability, it can be seen that laser irradiation at 10 MW/cm^2 initially results in a small decrease in the nucleation probability. The initial decrease in nucleation probability was followed by significant increases in nucleation probability as the applied laser intensity was increased. As expected, due to the minimal volume differences between measurements, the normalized nucleation probability follows a similar trend. However, the slight increase in nucleation probability at 25 MW/cm^2 can no longer be ascribed with certainty to laser irradiation. A similar statement can be made on the nucleation probability obtained at 70 MW/cm^2, as the large error in this observation, caused by the large deviation in volume, complicates definitive statements. Overall the nucleation probability, as expected based on literature, can be seen to linearly increase with the laser intensity [15, 30, 41, 64].

Similar to data obtained before at 1064 and 532 nm, the nucleation probability initially decreases upon irradiating the solution with laser light. As literature also shows no known absorption band for water at this wavelength, it once more seems to provide support for the observation being ascribed to the Nanoparticle Heating effects mentioned in Section 4.1.2 [117].

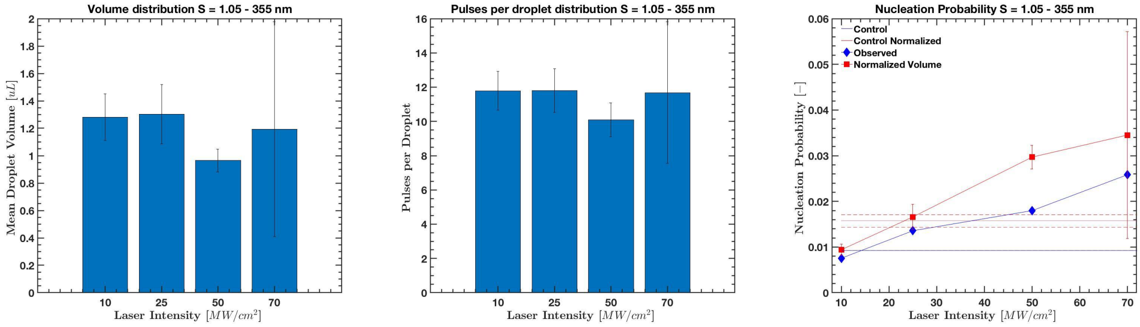

(a) (b) (c)

Figure 4.5: (a) Droplet volumes, (b) Laser pulses per droplet and (c) Nucleation probability (-) vs laser intensity (MW/cm^2) for S = 1.05 droplets irradiated by 355 nm light as well as the average nucleation probability from the control cooling experiments.

1.10 Supersaturated Solutions

The data in Figure 4.6a shows no significant volume differences between the measurements. Hence, no significant effects of volume are expected. However, the volume deviations in the lower laser intensity measurements (10 and 25 MW/cm^2) are substantially larger than in the higher intensity measurements (50 and 70 MW/cm^2), which will propagate into the normalized nucleation probability error. Analysis of Figure 4.6b results in similar observations, such that the number of pulses per droplet does not significantly differ between measurements.

From Figure 4.4c it is evident that laser irradiation at all intensities offered an increased nucleation probability, in comparison to the control experiments. In this sense, the rapid increase in nucleation probability when increasing the laser intensity from 25 to 50 or 70 MW/cm^2 is both remarkable and unexpected since it was not observed in measurements at 1064 and 532 nm before and no volume effects were to be expected between measurements. The lack of volume effects becomes clear when inspecting the normalized probability and the rapid increase in nucleation probability is seen to remain. Therefore, it is not caused by volume effects and can be ascribed to laser irradiation at these intensities. On the contrary, irradiation at 10 and 25 MW/cm^2 can no longer with certainty be considered to increase the nucleation probability, as their error bars now overlap with the control cooling experiment.

Slightly higher nucleation probabilities upon irradiation of KCl solutions with 355 nm as compared to irradiation with 1064 and 532 nm have been observed before in studies conducted within Eral Lab [30, 47]. However, within these studies this was seen for all applied laser intensities whereas here it is only observed for the higher laser intensities. Explanations for these observations were offered in the form of the slight absorption of the borosilicate confinement material inducing a pressure wave. However, at the applied intensities the pressure wave alone was incapable of inducing nucleation. A more likely explanation was offered in the non-linear absorption of 355 nm light by either the KCl solution or (nano) impurities present within it [47, 119]. If e.g. the impurities non-linearly absorb the 355 nm light, it can cause more rapid heating of the impurities. As a result, it might (positively) alter the heat and mass dynamics surrounding the impurity, or induce a so called thermo-elastic mechanism in which absorption causes fast thermal expansion and compression possibly inducing nucleation. These observations might thus once more provide some support for the Nanoparticle Heating model of NPLIN.

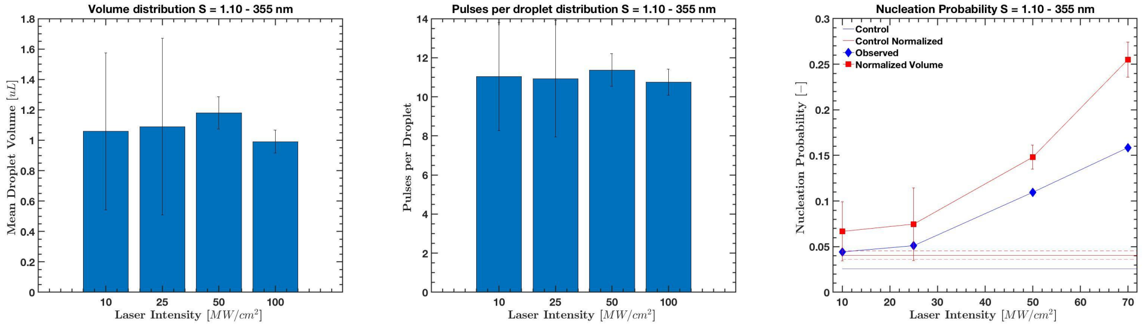

(a) (b) (c)

Figure 4.6: (a) Droplet volumes, (b) Laser pulses per droplet and (c) Nucleation probability (-) vs laser intensity (MW/cm^2) for S = 1.10 droplets irradiated by 355 nm light as well as the average nucleation probability from the control cooling experiments.

4.2. Influence of Laser Wavelength on Nucleation Probability

This section examines the influence of laser wavelength on the nucleation probability. First the results of laser irradiation experiments conducted on 1.05 supersaturated solutions are examined for this influence, followed by examination of the results obtained for 1.10 supersaturated solutions.

1.05 Supersaturated Solutions

In Figure 4.7a the volume distributions for S = 1.05 droplets irradiated with all wavelengths are displayed. At each wavelength, the measurements are portrayed in order of increasing laser intensity and show a similar trend as in the previous sections. As not all the error bars overlap, not all volumes can be considered comparable. Hence, volume effects are expected to play a role in the observed nucleation probabilities. Therefore, it was decided to only inspect the volume normalized nucleation probabilities for all wavelengths, as to ensure only the effect of irradiation at different wavelengths is visible in the data. The pulses per droplet distribution for all wavelengths in Figure 4.7b is, similar to the volume distribution in Figure 4.7a, portrayed in order of increasing intensity. It is clear that almost all error bars overlap and in the cases they do not the differences are small. As literature has shown the effect of pulses per sample to be negligible, it is not expected to significantly influence the observed nucleation probabilities.

The normalized nucleation probabilities (-) for the control cooling and irradiation experiments at all wavelengths vs the laser intensity (MW/cm^2) are displayed in Figure 4.7c. It can clearly be seen that at all wavelengths the nucleation probabilities follow similar trends. Not only does the data follow a similar trend for all wavelengths, the error bars of all points, except for two outliers at 10 MW/cm^2 and 25 MW/cm^2, also overlap. Overlap of these error bars indicates these points can be considered comparable, suggesting there is little to none wavelength effect observable. It should be noted that the effective reduction of the nucleation probability upon irradiation with 10 MW/cm^2 is visible for all wavelengths. Similarly, besides for 1064 nm, irradiation at 25 MW/cm^2 is ineffective. Overall, for S = 1.05, laser irradiation at all wavelengths is only proven to be effective at higher ($\geq$ 50 MW/cm^2) laser intensities.

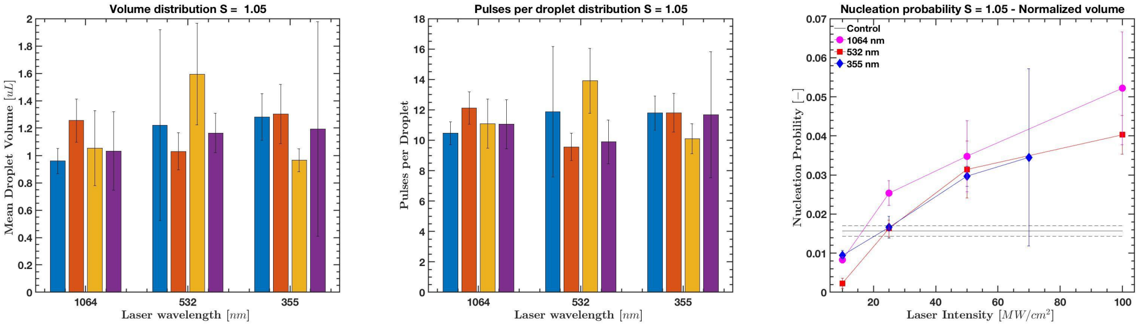

(a) (b) (c)

Figure 4.7: (a) Droplet volumes, (b) Laser pulses per droplets and (c) Nucleation probability normalized for volume (-) vs laser intensity (MW/cm^2) for S = 1.05 droplets irradiated by 1064, 532 & 355 nm light as well as the control cooling experiments.

1.10 Supersaturated Solutions

In Figure 4.8a the volume distributions for S = 1.10 droplets at all wavelengths is displayed. Similar as for the S = 1.05 data, not all volumes can be considered comparable as the error bars do not overlap. Hence, volume effects are expected to have played a role in the observed nucleation probability. Therefore, it was again decided to only inspect the normalized nucleation probabilities for all wavelengths. The pulses per droplet distribution for all wavelengths in Figure 4.8b shows only small differences between measurements, not expected to have significantly influenced the observed nucleation probability.

In Figure 4.8c it is evident that at the lower end of the applied laser intensities all obtained nucleation probabilities are relatively comparable. It is only at the higher laser intensities, the nucleation probabilities start to differ. Nucleation probabilities obtained by irradiation of the solution with 1064 & 532 nm at 50 and 100 MW/cm^2 can still be considered comparable. However, it is evident that the values obtained by irradiation with 355 nm at these higher intensities can not be considered comparable to the values obtained at 1064 & 532 nm. Therefore, for S = 1.10 some form of wavelength effect is visible upon irradiation with 355 nm at higher laser intensities ($\geq$ 50 MW/cm^2).

The observed wavelength effect might be explained by non-linear absorption of the solution or impurities within it. Non-linear absorption of the specific wavelength could explain both the observed difference between wavelengths as well as the observed difference between irradiation with lower vs higher laser intensities. It is proposed that, non-linear absorption of the light by impurities can cause more rapid heating of the solution surrounding these impurities. Rapid heating of the solution surrounding the impurities could either affect the heat and mass transfer dynamics surrounding them or cause the formation of a plasma, both are thought to induce nucleation [30, 47]. These observations might therefore provide further support for the Nanoparticle Heating model of NPLIN.

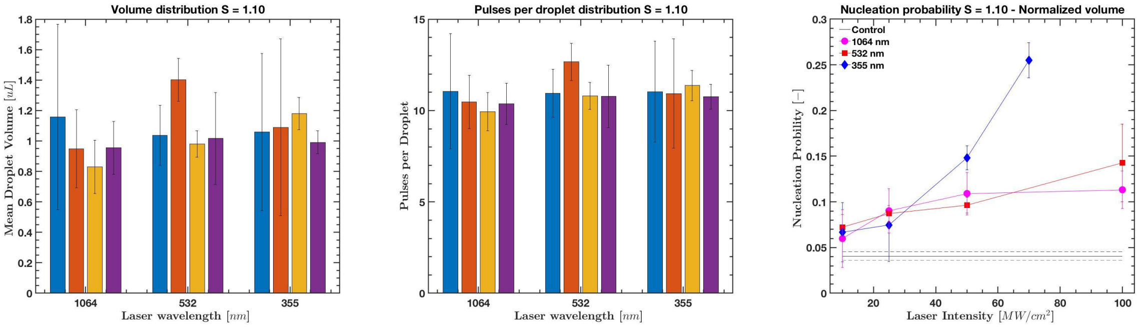

(a) (b) (c)

Figure 4.8: (a) Droplet volumes, (b) Laser pulses per droplets and (c) Nucleation probability normalized for volume (-) vs laser intensity (MW/cm^2) for S = 1.10 droplets irradiated by 1064, 532 & 355 nm light as well as the control cooling experiments.

4.3. Effect of Supersaturation on Nucleation Probability

In this section the effect of supersaturation on the nucleation probability is examined. Although supersaturation is essentially a nucleation affecting factor and not a NPLIN affecting factor, its variation still affects the nucleation probabilities observed within the system. Figure 4.9 displays the nucleation probabilities normalized for volume (-) vs laser intensity (MW/cm^2) at all wavelengths for S = 1.05 (Figure 4.9a) and S = 1.10 (Figure 4.9b). Interestingly enough, besides its expected effect of resulting in a higher nucleation probability, other effects can also be observed within the data.

For S = 1.10, irradiation with 25 MW/cm^2 of 1064 and 532 nm was already seen to be beneficial for inducing nucleation. Whereas for S = 1.05, irradiation at these intensities offered nucleation probabilities comparable to cooling experiments and higher intensities ($\geq$ 50 MW/cm^2) were needed to induce nucleation. The significant reduction in nucleation probability upon irradiation of S = 1.05 with laser intensities of 10 MW/cm^2 was not seen for S = 1.10. Thus, some supersaturation dependent effect could be observed, possibly explained by a supersaturation dependent intensity threshold. Furthermore, whereas for S = 1.05 a similar trend in nucleation probability was seen at all wavelengths, for S = 1.10 irradiation at higher laser intensities ($\geq$ 50 MW/cm^2) with 355 nm proved to be more effective.

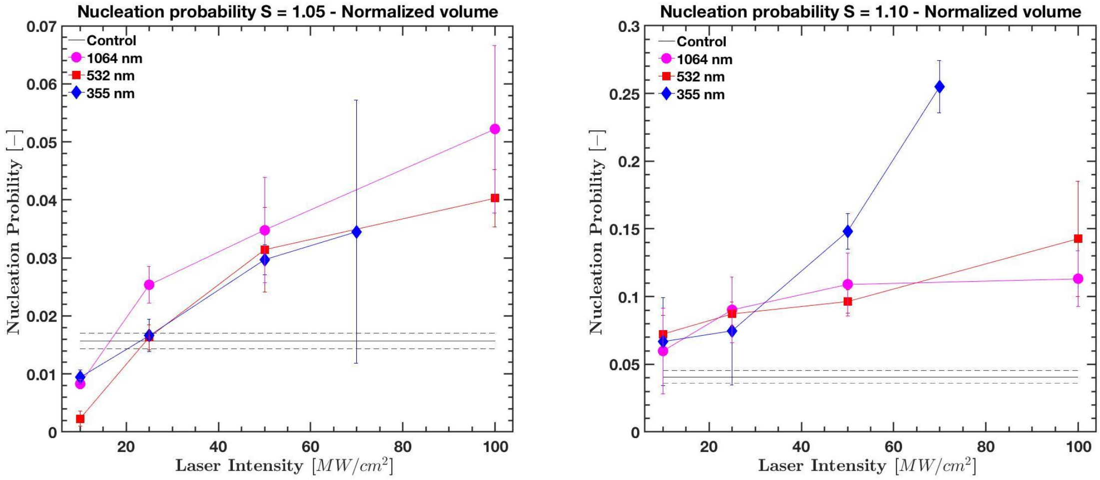

(a) (b)

Figure 4.9: Nucleation probability normalized for volume (-) vs laser intensity (MW/cm^2) for (a) S = 1.05 droplets and (b) S = 1.10 droplets irradiated by 1064, 532 & 355 nm light as well as the nucleation probability from control cooling experiments.

4.4. Comparative Analysis

Attempting to compare the work within this study to studies performed with at least moderately comparable volumes proved difficult, since most previous research has been conducted on batch samples of significantly larger (two orders of magnitude) volume. Therefore, results posted in literature will most probably not (directly) correspond with the results found in this study and only offer a qualitative comparison.

A more suitable comparison might be found in the previous study, on which the improved microfluidic system is based [16]. Upon comparison of their results, it is clear that the nucleation probabilities obtained within this study are significantly lower, e.g., the previous study reported a nucleation probability of 0.37 upon irradiation of S = 1.10 droplets with 50 MW/cm^2 as compared to values between 0.10 and 0.15 in this study. Explanations for this observation are found in the removal of the conversion piece in which droplet coalescence took place, the significantly smaller volumes studied in this study, improved coating of the capillary and possibly even the change of continuous phase [81].

Experiments under similar conditions to the previous study have been repeated. Unexpectedly, nucleation probabilities comparable to the previous study were initially obtained, i.e., much higher than found in the first set of experiments. After a process of elimination in which the capillaries were re-coated and new supersaturated solutions were prepared, the most likely cause was found to be reusing the square borosilicate capillaries. It was noted that all previous experiments were performed using brand new capillaries.

Upon inspection of a set of brand new uncoated capillaries, brand new coated capillaries and previously used coated capillaries, it was visible that the surface coating of the previously used capillaries was significantly worse than the brand new coated capillaries. As the effect was visible throughout the entire capillary, it was most likely not a direct effect of laser irradiation but a result of an apparent limited lifespan of the capillary under either the compound used to hydrophobically coat the surface or liquid flow. Therefore, it seemed essential to use brand new capillaries for each measurement, as to ensure the capillary does not disturb the flow and induce nucleation in the supersaturated solution.

Comparing this work to other studies conducted on batch samples within Eral Lab by Kacker et al. and Dhingra [30, 47], it is evident that the nucleation probabilities obtained within this system at higher applied laser intensities are still considerably lower. However, discrepancies are to be expected as the investigated volumes differ by two orders of magnitude. A further difference in the observed nucleation probabilities is caused by their substantially larger detection times. Kacker et al. and Dhingra used a detection time of 60 minutes, to ensure nuclei had sufficient time to grow to a detectable size, even though after 20 minutes the authors observed no significant change in the nucleation probability. In comparison, even the 20 minute detection time is considerably larger than the average 1 minute detection time employed in this study. Nevertheless, since these studies utilized a similar research framework, they can offer a valuable comparative reference for the observed trends.

Comparing the effect of laser intensity on the nucleation probability, Kacker et al. and Dhingra [30, 47] observed a laser intensity threshold around 0.5 MW/cm^2 and observed 100 % nucleation at laser intensity values above 5 MW/cm^2 for KCl solutions of S = 1.035, 1.049 and 1.055. These values are in ill contrast with the current study, as for S = 1.05 a significant decrease in nucleation probability was seen upon irradiation with 10 MW/cm^2 and much higher intensities ($\geq$ 50 MW/cm^2) were needed to offer improved nucleation probabilities. Similarly, for S = 1.10 laser intensities of $\geq$ 25 MW/cm^2 were needed to increase the nucleation probability. In addition, no clear saturation intensity, above which nucleation probability no longer increases with laser intensity, was observed within this study. Furthermore, as for the influence of laser wavelength on nucleation probability, Kacker et al. and Dhingra observed no significant laser wavelength effect [30, 47]. Nevertheless, the studies also encountered slightly higher nucleation probabilities upon irradiation with 355 nm light. However, here it was observed for all applied laser intensities and not only at higher laser intensities. Similar explanations were offered in the form of an induced pressure wave aiding nucleation or non-linear absorption of the solution or impurities present within it. Finally, as for the effect of supersaturation, the studies observed higher nucleation probabilities for solutions of higher supersaturation. These observations are partially in agreement with the results found within this study, where it is seen that S = 1.10 offers a higher nucleation probability than S = 1.05. However, some slight differences in the trends have been observed in this study between irradiated S = 1.05 and S = 1.10 solutions.

Further comparison of this work to other studies found within the literature [41, 64]. A study published by Alexander et al. [64] on the nucleation of a single KCl crystal upon exposure to a single laser pulse can offer some more insight. Although direct comparison with this study will face similar difficulty as the comparison with Kacker et al. and Dhingra due to the large difference in volume, it might offer some more insight into the laser intensity threshold. The study stated this threshold value to be practically supersaturation independent at 6.4 $\pm$ 0.5 MW/cm^2. Yet, closer inspection of their data reveals otherwise. The laser intensity threshold values, when taking the errors of the separate measurements into account, can be seen to vary between as much as 2 and 12 MW/cm^2. This observation offers some support for the explanation that irradiation of S = 1.05 with 10 MW/cm^2 might have been performed below the laser intensity threshold, explaining why no improved nucleation probability was observed.

Finally, comparing the work within this study to the only other successful study published on NPLIN of KCl in microfluidics by Hua et al. [41]. This study irradiates a continuous phase supersaturated solution, thus not irradiating samples of a fixed volume. In addition, due to the fact that it does not irradiated fixed sample sets, it is unable to post a (cumulative) nucleation probability. Instead, the study posts results normalized to 1 minute of flow. As direct comparison of the nucleation probabilities obtained within this study to the number of crystals per minute is disputable, it was decided to only qualitatively compare the trends and the adherence to known nucleation models in Chapter 5.

4.5. Considerations

The improved microfluidic system was used to perform control cooling experiments and research the effects of supersaturation, laser wavelength and laser intensity on the nucleation probability. Cooling experiments were ran as a reference for the laser irradiation experiments such that the effectiveness of irradiation can be determined. Increasing the supersaturation was found to increase the nucleation probability in both the control cooling as well as the laser irradiation experiments. However, for the lower supersaturation ($S = 1.05$) irradiation at a lower laser intensity (10 MW/cm^2) had an adverse effect and actually reduced the nucleation probability as compared to the control cooling experiment. As this effect was not observed at the higher supersaturation ($S = 1.10$), it might suggest some sort of supersaturation dependent effect, possibly explained by a supersaturation dependent laser intensity threshold. This hypothesis is further supported by the fact that for $S = 1.05$ irradiation at 25 MW/cm^2 did not offer increased nucleation probabilities at all wavelengths and irradiation at higher laser intensities was needed to increase the nucleation probability in comparison to the cooling experiments. In contrast, at $S = 1.10$, except for 355 nm, the nucleation probability increased for applied laser intensities above 25 MW/cm^2. Furthermore, irradiation of $S = 1.10$ by 355 nm light with laser intensities $\geq$ 50 MW/cm^2 offered significantly higher nucleation probabilities in comparison to the other two wavelengths. Therefore, a significant wavelength effect was only observed upon irradiation of $S = 1.10$ droplets with 355 nm light at higher laser intensities ($\geq$ 50 MW/cm^2).

Comparison of these results to studies published in literature proved difficult, due to a lack of experiments performed on samples of comparable volume. In general, it could be seen that the results found within this study did not strongly agree with values posted in literature. In order to offer a more reasonable comparison, it was decided to further analyze the data in common nucleation models and qualitatively compare the trends and adherence to these models in the next chapter.

5

Nucleation Models

In this chapter the data obtained in cooling and laser irradiation experiments is fitted to commonly used nucleation models such as Classical Nucleation Theory (CNT) and Dielectric Polarization (DP) model. Although the DP model is strictly speaking an adaption of CNT to describe NPLIN, both will be referred to as a nucleation model. First, the ability of CNT to describe the observations is investigated combined with a comparison of the obtained parameters with studies found in literature. Then, the ability of DP to model the observed behaviour is investigated and a comparison with the previous study as well as two studies found in literature is offered. Finally, the chapter is ended with a considerations section.

5.1. Classical Nucleation Theory

The Classical Nucleation Theory is a simplified model which describes the nucleation rate by an Arrhenius like equation (See Equation 2.5), accompanied by an equation relating the (cumulative) nucleation probability to the nucleation rate (Equation 5.1), a relation which can be inverted to Equation 5.2 [13, 19, 50]. The nucleation probabilities presented in Chapter 4 are fitted to the expression in Equation 5.2 for an estimation of the nucleation rates. As the nucleation probability is determined at a single location, accurate estimations of the induction time are unavailable. Hence, it was decided to approximate the induction time by the average time it took droplets to travel from the laser irradiation point to the observation point, otherwise known as the detection time.

In the following sections, nucleation rate estimations from both the control cooling and the irradiation experiments are presented and compared to two studies previously conducted within Eral Lab [16, 120]. Volume independent comparison with these studies is now possible, since the nucleation rate constitutes a measure of nucleation likeliness per unit volume and time [16]. The calculated nucleation rates are further analyzed for their fit with the CNT model, by determining a number of fitting parameters describing the CNT model, which will be compared with studies found in literature [56, 64, 121].

$$p_{nucleation} = 1 - \exp(-J \cdot V \cdot t) \tag{5.1}$$

$$J = \frac{-\ln(1 - p_{nucleation})}{V \cdot t} \tag{5.2}$$

1.05 supersaturated solutions

Nucleation rates calculated for S = 1.05 are presented in Table 5.1. The average nucleation rate of all control cooling experiments is included in each column to serve as a reference, detailed data on the separate measurements can be found in Appendix C.1. Inspecting these values, it can be seen that, besides the values obtained for 532 nm - 10 MW/cm^2 and 1064 nm - 25 MW/cm^2, all nucleation rates under comparable conditions can be considered equal. The slight lowering of the nucleation probability upon irradiation with 10 MW/cm^2 is still visible in these rates, thus implying it was not caused by a volume or (detection) time dependent effect. Similar conclusions were reached in Section 4.2.

Direct comparison for this supersaturation with nucleation rates calculated in the previous study (see Table 5.3) is complicated, since the lowest supersaturation studied there was 1.09. However, it is evident that all values, even upon irradiation with 70 or 100 MW/cm^2, are significantly lower than in the previous study. Additionally, the errors observed in the nucleation rates are considerably smaller, thus implying that the adjustments made to the microfluidic system in Chapter 3 have been beneficial.

Table 5.1: Nucleation rate (*J*) values for S = 1.05 calculated from the nucleation probabilities determined in the NPLIN experiments listed in Appendix B.4 for 1.05 supersaturated solutions.

Laser intensity (MW/cm^2)	**Nucleation rate (μL^{-1} h^{-1})**		
	1064 nm	**532 nm**	**355 nm**
Cooled	0.5441 ± 0.0507	0.5441 ± 0.0507	0.5441 ± 0.0507
10	0.2020 ± 0.0224	0.0781 ± 0.0472	0.2943 ± 0.0434
25	0.8644 ± 0.1189	0.6346 ± 0.0944	0.5912 ± 0.1044
50	1.1880 ± 0.3194	1.0740 ± 0.2597	1.0864 ± 0.1415
100 & 70	1.7802 ± 0.5061	1.6265 ± 0.2937	1.1932 ± 0.7903

1.10 supersaturated solutions

In Table 5.2 the nucleation rates for S = 1.10 are presented. As expected, S = 1.10 offered higher nucleation rates than S = 1.05. In general, at intensities ≥ 25 MW/cm^2 nucleation rates are significantly higher than in cooling experiments. Overall, except for the higher laser intensities of 355 nm, the nucleation rates are comparable. Additionally, the errors are considerably smaller than in the previous study. These results lead to similar conclusions as the previous chapter. It must be noted, that even under comparable conditions the nucleation rates are still significantly lower than in the previous study (see Table 5.3). Consequently, the higher nucleation probabilities observed in the previous study were not solely an effect of volume but also caused by other disturbances present within that system.

Table 5.2: Nucleation rate (*J*) values for S = 1.10 calculated from the nucleation probabilities determined in the NPLIN experiments listed in Appendix B.4 for 1.10 supersaturated solutions.

Laser intensity (MW/cm^2)	**Nucleation rate (μL^{-1} h^{-1})**		
	1064 nm	**532 nm**	**355 nm**
Cooled	1.3867 ± 0.1736	1.3867 ± 0.1736	1.3867 ± 0.1736
10	2.2729 ± 1.2145	2.5111 ± 0.5151	2.4854 ± 1.2256
25	3.2318 ± 0.8949	3.1130 ± 0.3596	2.7060 ± 1.4533
50	3.7810 ± 0.8255	3.3707 ± 0.3508	5.4650 ± 0.5770
100 & 70	4.1896 ± 0.8153	5.1538 ± 1.5793	9.3857 ± 0.8612

Further comparing the values for S = 1.10 with a study performed by Shingte, who studied both stagnant and moving droplets of ± 1 μL and S = 1.10, 1.12 and 1.15 [120]. Research conducted by Shingte on stagnant droplets revealed that, as the supersaturation was lowered, the dominating nucleation mechanism might have shifted from a bulk mechanism to a surface assisted mechanism. Based on this assumption, it was decided to conduct a smaller set of experiments comparing stagnant with moving and continuously mixing droplets. In these experiments, the nucleation rate was found to be higher in stagnant than in moving droplets. These observations offered support for the surface assisted mechanism aiding nucleation in stagnant droplets, as the wall interactions in the moving droplets were much lower. Comparing the results in Tables 5.2 and 5.3, it is clear that, under comparable conditions, the nucleation rates calculated in this study are significantly higher than Shingte determined for moving droplets. The calculated nucleation rates are much closer to the value determined by Shingte in stagnant droplets. Resulting in the assumption that a surface mechanism might be aiding nucleation in the improved microfluidic system employed in this study.

Table 5.3: Nucleation rates determined at varying supersaturation in the previous study for cooling and irradiation experiments (532 nm - 50 MW/cm^2) and by Shingte for both stagnant and moving droplets [16, 120].

	Nucleation rate (μL^{-1} h^{-1})			
Supersaturation	**Previous Study - Cooled**	**Previous Study - Irradiated**	**Shingte - Stagnant**	**Shingte - Moving**
1.09	0.6016 ± 1.0137	16.7072 ± 2.4782		
1.10	2.6247 ± 1.2357	20.2333 ± 6.3702	1.035 ± 0.472	0.506 ± 0.066
1.11	0.6977 ± 1.1745	18.8794 ± 5.2045		
1.12	2.4674 ± 1.4311	155.0668 ±68.4169	5.601 ± 1.668	
1.15			0.884 ± 0.133	

Fitting of the Experimental Data

The calculated nucleation rates can be further processed to assess whether CNT is able to describe the observed nucleation behaviour. The relation in Equation 2.5 is generally simplified and stated as Equation 5.3 where B is defined as Equation 5.4. The relationship in Equation 5.3 can be linearized to Equation 5.5 and used to determine the unknown coefficients A and B.

$$J = A \cdot S \cdot \exp\left(\frac{-B}{(\ln(S))^2}\right) \tag{5.3}$$

$$B = \frac{16\pi\gamma^3 v^2}{3(k_B T)^3} \tag{5.4}$$

$$\ln\left(\frac{J}{S}\right) = \ln(A) - \frac{B}{(\ln(S))^2} \tag{5.5}$$

The nucleation rates in Table 5.1 and 5.2 were fitted to the linear expression in Equation 5.5 using Matlab. Nucleation rates found at equal laser intensity for both S = 1.05 and 1.10 were correlated and Matlab calculated a best fit value of the coefficients to describe the overall data set at a specific wavelength. However, this relates only two data points at a time, and a straight line can be drawn between any two points, such that the outcomes of these estimations are highly ambiguous. Therefore, the results of this analysis can only provide weak approximations and should be approached with caution.

Table 5.4 displays the outcomes of this analysis as well as a further processing of the parameter B to calculate γ, the interfacial tension between the nucleus and the solution. Inspection of the values obtained for A, show that the parameter was estimated to be slightly smaller in cooling experiments than in laser irradiation experiments. The values obtained in the laser irradiation experiments are relatively comparable for 532 and 355 nm, whilst a substantially higher value is found for 1064 nm.

The previous study obtained values for A of $1.09 \cdot 10^6$ m^{-3} s^{-1} and $1.38 \cdot 10^8$ m^{-3} s^{-1} in cooling and irradiation experiments. It is evident that the parameters obtained in this study are orders of magnitude lower, and the difference between the cooling and irradiation experiments is much smaller. However, it is important to stress that the previous study based its estimations on 4 (cooling) and 5 (irradiation) data points, hence they may offer a considerably more accurate estimation. A study by Laval et al. concluded that values of A between 10^1 and 10^7 are typical for heterogeneous nucleation [121]. Comparison of the values in Table 5.4 with Laval et al., leads to to the conclusion that the crystals formed in both the control cooling and the laser irradiation experiments were likely formed due to heterogeneous nucleation. Crystal formation due to heterogeneous nucleation corresponds with the above-mentioned possible surface aided mechanism and, as the effect is present in both the control cooling and the irradiation experiments, can not be directly ascribed to the effect of the laser.

Table 5.4 further displays the parameter B, which can be used to calculate γ, the interfacial tension between the nucleus and the solution, by use of Equation 5.4 and the parameters in Appendix C.1.2 [121]. The results of these calculations are presented in Table 5.4. The previous study obtained values of 2.39 mN m^{-1} and 3.13 mN m^{-1} for γ, relatively comparable to values posted in literature [16]. In a first experiment Alexander et al. found a value of 5.283 mN m^{-1} for γ, whereas in later experiments it was estimated to be 2.19 mN m^{-1} [56, 64]. It is evident that the values obtained in this study fall below these estimations, possibly owing to the small data set used to determine them. Yet, a study by Ildefonso et al. proposed the nucleation rate, A and γ to be influenced by the chemical nature of the water-oil interface. Even though the studied nucleation events differ, the effect of the altered nature of the droplet interface on nucleation might still be present in the system at hand. Therefore, the lower estimations of A and γ might be (in part) due to the change of continuous phase [81].

Table 5.4: Results of fitting the calculated nucleation flux's to the Classical nucleation theory expression in Equation 5.3, with A (m^{-3} s^{-1}) and B the unknown fitting parameters and γ (mN m^{-1}) the interfacial tension between the nucleus and the solution.

Parameter	**Cooling**	**1064 nm**	**532 nm**	**355 nm**
A (m^{-3} s^{-1})	$4.27 \cdot 10^5$	$13.7 \cdot 10^5$	$9.1 \cdot 10^5$	$9.5 \cdot 10^5$
B	0.0027	0.0048	0.0033	0.0025
γ (mN m^{-1})	1.4202	1.7273	1.5243	1.3921

5.2. Dielectric Polarization Model

Nucleation probabilities obtained in the laser irradiation experiments can be further analyzed by use of the DP model. The DP model describes the number of crystals to be directly proportional to the applied laser intensity (Equation 2.8), where the nucleation probability is then expressed as Equation 2.9. However, the relationships in Equations 2.8 and 2.9 fail to accurately describe a laser intensity threshold for NPLIN to occur, encountered in experimental data. Therefore, they are generally adjusted to Equations 5.6 and 5.7, where I_{th} is the laser intensity threshold and m a lability factor. The lability factor describes the ease with which a system nucleates, and is thought to be specific for each solute. Analysis of the data in the DP model thus requires determination of the lability factor.

$$N_{Crystal} = m \cdot (I - I_{th}) \tag{5.6}$$

$$p_{nucleation} = 1 - \exp(-m(I - I_{th})) \tag{5.7}$$

The data obtained in the irradiation experiments was fitted to the expression in equation 5.7 by use of the Matlab curve fitting tool. However, first an estimation of the laser intensity threshold needed to be obtained from literature, since accurate data on the intensity threshold was not procured in this study. The data presented in Chapter 4 indicated the intensity threshold of the system to be over 10 MW/cm^2, in contrast with values found in literature. Kacker et al. and Dhingra found the threshold to be around 0.5 MW/cm^2, whereas Alexander et al. reported a supersaturation independent threshold at 6.4 ± 0.5 MW/cm^2 [30, 47, 64]. However, upon closer inspection of the data from Alexander, the threshold could be seen to vary between 2 and 12 MW/cm^2 and differed slightly between supersaturations. Therefore, it was decided to use the intensity threshold values found by Alexander et al. at their respective supersaturation, since the reported values of the intensity threshold were closer to that expected for this system and slight supersaturation dependent effects were observed within this study.

The results of the Matlab fitting, adjusted for the bulk volume (0.35 mL) employed in the study by Alexander et al., are presented in Table 5.5, detailed information on all the separately determined lability parameter values can be found in Appendix C.2. The factor is labeled m_{VI} as to stress the adjustment for the volume from the directly determined values.

Analyzing the results for S = 1.05 in Table 5.5, it is clear that the lability factor is virtually the same for all wavelengths. Indicating that the irradiated solutions had similar ease to nucleate. However, when the lability factor for S = 1.10 is examined, substantial differences can be seen between the factor determined for 1064 & 532 nm and for 355 nm. This difference could be explained based on the significantly higher nucleation probabilities observed for irradiation with 355 nm at the higher laser intensities. Nevertheless, it was also noted that the parameters describing the quality of the fit (see Appendix C.2.2) were considerably worse for the 1064 and 532 nm fittings. Therefore, a better approximation of the lability factor could be to take the average of the lability factor determined at each individual point. The results of which are also displayed in Table 5.5 and are much more comparable between the wavelengths.

Table 5.5: Lability parameter (m_{VI}) values for S = 1.05 & 1.10 corrected for both the bulk volume and laser intensity threshold encountered in the literature [64], determined by use of the Matlab curve fitting toolbox and calculation of the average.

	Lability Parameter (cm^2/MW)		
Supersaturation	**1064 nm**	**532 nm**	**355 nm**
1.05	0.1427 ± 0.0759	0.1120 ± 0.0689	0.1374 ± 0.0649
1.10	0.3747 ± 0.4255	0.4245 ± 0.3987	0.9488 ± 0.4409
1.10 - Averaged	1.2773 ± 0.5712	1.3920 ± 0.2392	1.5626 ± 0.6145

Table 5.6 displays all lability factors of KCl systems posted in literature so far. Comparing the lability factors in Table 5.5 with the previous study, we observe that at equal supersaturation the lability factors determined within this study were considerably lower at all wavelengths. However, when taking the errors into account the estimation of the averaged lability factor can be considered comparable. Further comparing the lability factors determined for S = 1.05 with the values obtained for S = 1.06 by Hua et al. and Alexander et al., it is evident that the lability factors for S = 1.05 are substantially larger.

Analyzing the results for S = 1.10 it is clear that the values determined with the Matlab curve fitting tool, especially at 355 nm, are comparable to the value obtained by Hua et al. as the error bars overlap. Yet, this is mainly due to the large error in these estimations, thereby lacking any real substantiation. The averaged lability factors are much further from the value obtained by Hua et al. and still suffer from significant errors. Thus, overall no strong agreement with values obtained in literature is found.

Table 5.6: Lability parameter (m_{VI}) values presented in the previous study conducted within this group, single-phase microfluidic NPLIN experiments (Hua et al.) and bulk experiments (Alexander et al.)[16, 41, 56].

	Lability Parameter (cm^2/MW)		
Supersaturation	**Previous Study**	**Hua et al.**	**Alexander et al.**
1.06		0.064 ± 0.010	0.057 ± 0.004
1.08	0.2968 ± 0.1759	0.459 ± 0.026	
1.09	1.7533 ± 0.2371		
1.10	2.0683 ± 0.5951	0.730 ± 0.093	
1.11	1.8497 ± 0.4528		
1.12	13.918 ± 5.7694		

5.3. Considerations

Nucleation rates calculated for the control cooling experiments by use of the Classical Nucleation Theory were comparable to those found in stagnant micro droplets, where nucleation is proposed to be aided by a surface mechanism. Nucleation rates calculated for laser irradiation experiments displayed similar trends as in Section 4.2 and were found to be considerably lower than in the previous study. It resulted in the conclusion that the lower observed nucleation probabilities were not (solely) an effect of volume, since volume and detection time independent comparison with this study was now possible. The observations were most likely caused by other disturbances present in that system and potentially also (in part) explained by the change of continuous phase. Furthermore, the reduced errors in the computed nucleation rates indicated that the improvements of the microfluidic system employed in this study have been beneficial.

Further examining the data for its fit with the CNT model was complicated, due to the small amount of data points at varying supersaturations, resulting in a large uncertainty as to the validity of the outcomes. The coefficients obtained for the CNT model from the laser irradiated data had a similar implication as the control cooling experiments, as they were found to be in a region typical for heterogeneous nucleation. However, as the effect was both present in the control cooling as well as the irradiation experiments, it could not be ascribed to laser irradiation with certainty.

Lability parameters were determined for the laser irradiation experiments by fitting the data to the DP model. For S = 1.10 the lability parameters were found to be comparable with literature, as the error bars in these values overlap. However, this is mainly due to the large error in these estimations. For S = 1.05 no direct comparison was available in literature, but the determined lability parameters were much larger than values previously found for S = 1.06. Thus, overall no strong agreement with lability parameters in literature was found.

Some observations suggest a heterogeneous effect to play a part in the induction of nucleation within the system. The effect can not be ascribed to a nanoparticle model with certainty, since it is also visible in the control cooling experiments. Therefore, it is most likely, at least in part, caused by the surface of the square glass capillary aiding the nucleation process. Furthermore, as no particular experimental parameters have been varied to investigate the effect of impurities present within the solution, it is difficult to make bold statements as to the validity of this model explaining the observed heterogeneous effects. However, as the examination of the experimental data in Chapter 4 pointed out that the Nanoparticle Heating model might be the explanation for the reduction in nucleation probability observed upon irradiation of S = 1.05 with 10 MW/cm^2 and the non-linear absorption of 355 nm by S = 1.10 at higher laser intensities, some evidence was thought to be found for this model. Therefore, a more elaborate study into the effects of impurities within this system inducing nucleation is needed to draw a conclusion.

6
Conclusion

6.1. Conclusion

Within this study, a microfluidic system previously designed within Eral Lab was altered and improved. Alterations encompassed a change in continuous phase, new droplet generation zone tubing, a change of droplet formation method, an improved imaging set-up, a new laser directing set-up and an update of equipment used to hydrophobize components of the system. As a result, droplet formation was considerably more consistent and droplet coalescence was removed from the system. Further, the improved imaging set-up combined with the reduction of noise in the system eased data analysis. Whereas the new laser directing set-up decreased the amount of damage incurred by the equipment. Once improved, the system was used to study the NPLIN phenomenon in aqueous KCl solutions and determine the effects of supersaturation, laser intensity and laser wavelength on the nucleation probability. The effectiveness of laser irradiation was measured in comparison to control cooling experiments.

With respect to the effect of laser intensity, for S = 1.05, laser irradiation was only proven to be more effective at laser intensities $\geq$ 50 MW/cm^2. Unexpectedly, a significantly lower nucleation probability was observed upon irradiation with 10 MW/cm^2, possibly indicating a supersaturation dependent laser intensity threshold exceeding this value. The observation could potentially be explained based on the Nanoparticle Heating model for NPLIN. For S = 1.10 irradiation was already seen to be effective at laser intensities $\geq$ 25 MW/cm^2.

As for the influence of laser wavelength, besides irradiation of S = 1.10 with 355 nm at laser intensities $\geq$ 50 MW/cm^2 to be more effective, no significant wavelength effect was observed. These observations were proposed to be caused by non-linear absorption of the light by either the solution itself or impurities within it.

Finally, concerning the effect of supersaturation, it was evident that a higher supersaturation resulted in a higher nucleation probability. Accompanied by this observation were the differences, for the effect of laser intensity and the influence of laser wavelength, mentioned within this paragraph.

Further analysis of the data was done by investigating the ability of common nucleation models to describe the observations and resulted in the following conclusions. Nucleation rates calculated in control cooling experiments using the Classical Nucleation Model were higher than expected and, based on data found in the literature, indicated a possible surface mechanism to aid nucleation. Fitting parameters determined in this model yielded a similar suggestion, as they are in ranges typical for heterogeneous nucleation. By use of this model, estimations for the interfacial tension between the nucleus and the solution were obtained. The estimated interfacial tensions were lower than values previously presented in literature, possibly (at least in part) caused by the altered continuous phase. Nevertheless, it must be noted these estimations are highly ambiguous as they are merely based on two data points, such that they can only serve to indicate some trends.

Further analyzing the data in the Dielectric Polarization model, lability parameters were determined for the irradiation experiments. Values found for S = 1.05 were significantly higher than values found in literature. For S = 1.10, the lability parameters, when taking the error bars into account, could be considered comparable with values found in literature. However, due to the large error in these estimations, this lacked any real substantiation.

Finally, some support for the nanoparticle heating model was found, based on the lowered nucleation probability upon irradiation of S = 1.05 with 10 MW/cm^2 and the non-linear absorption of 355 nm by S = 1.10. Yet, as this has not been thoroughly researched, it would require further study to deliver a definitive statement on the role (nano) impurities played in the induction of nucleation in this study.

6.2. Recommendations

This section first presents a number of suggestions to further improve the microfluidic system used to study the NPLIN effect, followed by a small set of suggestions for future study.

6.2.1. Microfluidic System

The improvements implemented throughout this study solved most issues encountered in the design and validation phase of the system. However, to maximize the value of this system and to ensure it achieves its full potential, the system can still be further improved. Experiments conducted within this study led to the proposition of the following improvements:

- **Improved control over the droplet volume:** As most of the uncertainty within the system is still caused by volume fluctuations, resulting in the need to normalize the obtained nucleation probabilities, gaining more control over the volume and a more consistent droplet volume would be preferable. Improved control over the droplet volume could, in part, be achieved by using a inner capillary of consistent inner diameter with a smooth tip. As in the current system the inner capillary is shaved to a usable size by the naked eye, resulting in inner capillaries with an inconsistent inner diameter size and rough uneven edges around their opening. Nevertheless, a larger influence seems to be the environment in which the droplets are generated, such that a more consistent or more hydrophobic coating could improve the consistency of droplet formation. Additionally, this would have the added benefit of further reducing the surface interaction between the droplet and the capillary, decreasing its likelihood of inducing nucleation.

- **Tighter temperature control of the system and the solution:** Tighter temperature control of the solution would give the system the ability to tighter control the droplet supersaturation. To this end, a Peltier cooler could be implemented in the laser irradiation and crystal observation zones, to directly control and keep constant the solution temperature. As the solution volumes are small and the thickness of the confinement material is not substantial, heat transfer is expected to be fast. Besides this, directly measuring the solution temperature by use of IR temperature sensors, before and after irradiation, could give a better estimation of the solution supersaturation and potential heating effects of irradiation. Similarly, improved heating equipment for the temperature controlled environment could reduce the error proneness of the system. Currently, the temperature controlled environment consists of a box, which is heated by use of a hairdryer and a microcontroller. It was found during this study that upon fixating the box’s lid, flow within the droplet generation zone seemed to be disturbed. This observation seemed to be caused by vibration of the box, resulting in movement of the capillary. Therefore, implementing an improved heating system, by use of for example a temperature bath and silicone tubing, reduces this susceptibility to error.

- **Improved imaging set-up:** To gain more insight into the induction time of KCl crystals, as to yield a more accurate estimation of the nucleation rate, and direct effect of laser irradiation. The system could implement an imaging set-up capable of monitoring the droplets throughout the capillary by use of multiple cameras along the capillary or implement a second camera imaging the droplets upon and shortly after irradiation. Additionally, adjustment of the system would allow it to be used for induction time measurements in future experiments.

6.2.2. Future research

Future research should first and foremost ensure that the combination of droplet volume, supersaturation and detection time results in crystals of a significant enough size, as to ease manual and even more so automated crystal detection. As in the S = 1.05 experiments crystal detection was often times complicated, even in the improved system, due to the relatively small size of the crystals caused by the low supersaturation in combination with the small volume. The most straightforward way to achieve crystals of significant enough size for automated detection would be to increase the supersaturation. Furthermore, within this study the following recommendations were found for further study:

- **Research the effects of impurities:** Additional research is required to deliver a definitive statement on the role (nano) impurities played in the induction of nucleation in this study. It would require a systematic study into the effects of (nano) impurities on the nucleation probability, by for example filtration of the impurities and subsequent reversal of the effect upon doping of the solution. Concurrently, the study could focus on determining the exact composition of the (nano) impurities believed to induce nucleation. Furthermore, the study could focus on studying the effects of the nanoparticle concentration on both the laser intensity threshold as well as the nucleation probability. A previous study performed by Ward et al.[71] on the laser induced nucleation of carbon dioxide found that the laser intensity threshold of unfiltered samples was slightly lower than filtered samples and lability was seen to increase when increasing the amount of impurities. However, as no elaborate systematic study of the effect of varying the nanoparticle concentration on the laser intensity threshold and nucleation probabilities was performed, it might yield more insight into the mechanism and intricacies of NPLIN.

- **Investigate the effect of detection time on the nucleation probability:** To understand the effect of detection time on the nucleation probability and possibly yield a more accurate estimation of the nucleation probability upon irradiation. Future research could slightly adapt the system and study the effect of irradiation in 60 cm square borosilicate capillaries, which would triple the detection time.

- **Study the effect of pulses per droplets:** Although literature has shown the effect of number of laser pulses per sample to be negligible, future research could compare the nucleation probability obtained under continuous exposure with exposure by a single laser pulse. Specifically, future research could perform a systematic study of the effect of number of laser pulses per sample at varying wavelengths. However, it would first need to improve shutter control, since it has proven difficult for the IR sensors to properly detect the droplets and subsequently send a detectable trigger signal to the shutter. Improvements in the shutter control loop were seen by implementation of a (digital delay) pulse generator to detect and 'amplify' the droplet signal.

- **Characterize the crystal size and size distribution:** Images captured during experiments can be analyzed by use of ImageJ to characterize the crystal size and its distribution. This would allow the system to determine an effect of the laser on the obtained crystal size distribution in comparison to cooling crystallization. Further, it could allow the system to study the effect of varying laser intensity on the crystal size distribution. If image analysis fails, the crystals could be separated from the supersaturated solution at the capillary outlet for subsequent study by use of static light scattering. However, continuous separation of the supersaturated phase and the crystals might prove complicated and, if failed, could bias the crystal size distribution when crystals continue to grow before analysis.

- **Research the polymorphic control ability of NPLIN:** The system could be used to gain more understanding on the abilities of NPLIN to offer polymorphic control. Future research could for example study glycine, which with its 'shown' need for aging could offer additional parameters to be studied [61, 73, 75]. Other compounds shown to exhibit polymorphic control upon irradiation are L-histidine, Carbamazepine and Sulfathiozole [68, 69, 122]. Besides compounds known to exhibit polymorphic control, future research could also focus on compounds shown to be NPLIN active but for which polymorphic control was not yet achieved, such as Adipic Acid, Succinic Acid or L-Glutamic acid [73]. However, it must be noted that study of these specific compounds will yield knowledge on the ability of NPLIN to offer polymorphic control in these specific systems, but might not yield deeper knowledge on the underlying NPLIN mechanism.

Reference list

[1] Z. Gao, S. Rohani, J. Gong, and J. Wang, *Recent developments in the crystallization process: Toward the pharmaceutical industry,* Engineering **3**, 343 (2017).

[2] J. A. Dirksen and T. A. Ring, *Fundamentals of crystallization: Kinetic effects on particle size morphology,* Chemical Engineering Science **46**, 2389 (1991).

[3] Syrris, *Crystallization,* (2020), retrieved from `https://www.syrris.com/applications/what-is-crystallization-and-what-are-the-methods-of-crystallization/`.

[4] J. H. ter Horst, C. Schmidt, and J. Ulrich, *32 - fundamentals of industrial crystallization,* in *Handbook of Crystal Growth (Second Edition)*, Handbook of Crystal Growth, edited by P. Rudolph (Elsevier, Boston, 2015) second edition ed., pp. 1317–1349.

[5] W. Beckman, *Crystallization - Basic Concepts and Industrial Applications* (Wiley-VCH, 2013) pp. 1–14.

[6] W. Moerman, M. Carballa, A. Vandekerckhove, D. Derycke, and W. Verstraete, *Phosphate removal in agro-industry: Pilot- and full-scale operational considerations of struvite crystallization,* Water Research **43**, 1887 (2009).

[7] M. L. Ovecoglu, B. Kuban, and H. Ozer, *Characterization and crystallization kinetics of a diopside-based glass-ceramic developed from glassindustry raw materials,* Journal of European Ceramic Society **7**, 957 (1997).

[8] C. D. Doan, I. Tavernier, P. K. Okuro, and K. Dewettinck, *Internal and external factors affecting the crystallization, gelation and applicability of wax-based oleogels in food industry,* Innovative food science & Emerging Technologies **45**, 42 (2018).

[9] M. Giulietti, M. M. Seckler, S. Derenzo, M. I. Ré, and E. Cekinsk, *Industrial crystallization and precipitation from solutions: State of the technique,* Brazilian Journal of Chemical Engineering **18**, 423 (2001).

[10] A. El-Zhry El-Yafi and H. El-Zein, *Technical crystallization for application in pharmaceutical material engineering: Review article,* Asian Journal of Pharmaceutical sciences **10**, 283 (2015).

[11] J. Seader and E. Henley, *Separation Process Principles*, Vol. 2 (John Wiley & Sons, Inc., 2006) pp. 644–689.

[12] A. B. de Haan and H. Bosch, *Industrial Separation Processess*, Vol. 1 (De Gruyter, 2013) pp. 207–233.

[13] A. M. Mackenzie, *Investigating Nucleation Control in Batch and Flow using Non-Photochemical Laser-Induced Nucleation*, Ph.D. thesis, The university of edinburgh (2017).

[14] R. D. Braatz, *Advanced control of crystallization processes,* Annual Reviews in Control **26**, 87 (2002).

[15] A. J. Alexander and P. J. Camp, *Non-photochemical laser-induced nucleation,* The Journal of Chemical Physics **150**, 040901 (2019).

[16] L. Stam, *Desgin and Validation of a Droplet-Based Microfluidic System to Study Non-Photochemical Laser-Induced Nucleation*, Master's thesis, Delft University of Technology (2020).

[17] Z. K. Nagy, M. Fujiwara, and R. D. Braatz, *Modelling and control of combined cooling and antisolvent crystallization processes,* Journal of Process Control **18**, 856 (2008).

[18] R. Grossier and S. Veesler, *Reaching one single and stable critical cluster through finite-sized systems,* Crystal Growth & Design **9**, 1917 (2009).

[19] D. Erdemir, A. Y. Lee, and A. S. Myerson, *Nucleation of crystals from solution: Classical and two-step models,* Accounts of Chemical Research **42**, 621 (2009).

[20] S. M. Nowee, A. Abbas, and J. A. Romagnoli, *Antisolvent crystallization: Model identification, experimental validation and dynamic simulation,* Chemical Engineering Science **63**, 5457 (2008).

[21] N. Kubota, N. Doki, M. Yokota, and A. Sato, *Seeding policy in batch cooling crystallization,* Powder Technology **121**, 31 (2001).

[22] J. Ferreira, J. Opsteyn, F. Rocha, F. Castro, and S. Kuhn, *Ultrasonic protein crystallization: Promoting nucleation in microdroplets through pulsed sonication,* Chemical Engineering Reserach and Design **162**, 249 (2020).

[23] R. Kacker, P. M. Salvador, G. S. J. Sturm, G. D. Stefanidis, R. Lakerveld, Z. K. Nagy, and H. J. M. Kramer, *Microwave assisted direct nucleation control for batch crystallization: Crystal size control with reduced batch time,* Crystal Growth & Design **16**, 440 (2016).

[24] S. W. Young, *Mechanical stimulus to crystallization in super-cooled liquids,* Journal of American Chemical Society **33**, 148 (1911).

[25] F. C. Wen, T. McLaughlin, and J. L. Katz, *Photoinduced nucleation of supersaturated vapors in the presence of carbon disulftde,* Physical Review A **26**, 2235 (1982).

[26] A. Soare, R. Dijkink, M. R. Pascual, C. Sun, P. W. Cains, D. Lohse, A. Stankiewicz, and H. J. M. Kramer, *Crystal nucleation by laser-induced cavitation,* Crystal Growth & Design **11**, 2311 (2011).

[27] T. Sugiyama and H. Masuhara, *Laser-induced crystallization and crystal growth,* Chemistry - an Asian Journal **6**, 2878 (2011).

[28] B. A. Garetz, J. E. Aber, N. L. Goddard, R. G. Young, and A. S. Myerson, *Nonphotochemical, polarization-dependent, laser-induced nucleation in supersaturated aqueous urea solutions,* Physical Review Letters **77**, 3475 (1996).

[29] H. Y. Yoshikawa, Y. Hosokawa, and H. Masuhara, *Explosive crystallization of urea triggered by focused femtosecond laser irradiation,* Japanese Journal of Applied Physicis **45**, L23 (2006).

[30] R. Kacker, S. Dhingra, D. Irimia, M. K. Ghatkesar, A. Stankiewicz, H. J. M. Kramer, and H. B. Eral, *Multiparameter investigation of laser-induced nucleation of supersaturated aqueous kcl solutions,* Crystal Growth & Design **18**, 312 (2018).

[31] Y. Xiao, S. K. Tang, H. Hao, R. J. Davey, and T. Vetter, *Quantifying the inherent uncertainty associated with nucleation rates estimated from induction time data measured in small volumes,* Crystal Growth & Design **17**, 2852 (2017).

[32] B. Clair, A. Ikni, W. Li, P. Scouflaire, V. Quemener, and A. Spasojevic-de Bire, *A new experimental setup for high-throughput controlled non-photochemical laser-induced nucleation: application to glycine crystallization,* Journal of Applied Crystallography **47**, 1252 (2014).

[33] A. M. Ganan-Calvo, J. M. Mantanero, L. Martin-banderas, and M. Flores-mosquera, *Building functional materials for health care and pharmacy from microfluidic principles and flow focusing,* Advanced Druge Delivery Reviews **65**, 1447 (2013).

[34] Q. Feng, J. Sun, and X. Jiang, *Microfluidics-mediated assembly of functional nanoparticles for cancer-related pharmaceutical applications,* Nanoscale **8**, 12430 (2016).

[35] S. Sigiura, T. Oda, Y. Izumida, Y. Aoyagi, M. Satake, A. Ochiai, Y. Ohkohchi, and M. Nakajima, *Size control of calcium alginate beads containing living cells using micro-nozzle array,* Biomaterials **26**, 3327 (2005).

[36] L. H. Hung, K. M. Choi, W. Y. Tseng, Y. C. Tan, K. J. Shea, and A. P. Lee, *Alternating droplet generation and controlled dynamic droplet fusion in microfluidic device for cds nanoparticle synthesis,* Lab on a Chip , 174 (2006).

[37] L. Frenz, A. El Harrak, M. Pauly, S. Begin-Colin, A. D. Griffiths, and J. C. Baret, *Droplet-based microreactors for the synthesis of magnetic iron oxide nanoparticles,* Angewandte Chemie International Edition **47**, 6817 (2008).

[38] B. Zheng, J. D. Tice, L. Spencer Roach, and R. F. Ismagilov, *A droplet-based, composite pdms/glass capillary microfluidic system for evaluating protein crystallization conditions by microbatch and vapor-diffusion methods with on-chip x-ray diffraction,* Angewandte Chemie International Edition **43**, 2508 (2004).

[39] J. Ferreira, F. Castro, F. Rocha, and S. Kuhn, *Protein crystallization in a droplet-based microfluidic device: Hydrodynamic analysis and study of the phase behaviour,* Chemical Engineering Sciences **191**, 232 (2018).

[40] L. Li and R. F. Ismagilov, *Protein crystallization using microfluidic technologies based on valves, droplets, and slipchip,* Annual Review of Biophysics **39**, 139 (2010).

[41] T. Hua, O. Gowayed, D. Grey-Stewart, B. A. Garetz, and R. L. Hartman, *Microfluidic laser-induced nucleation of supersaturated aqueous kcl solutions,* Crystal Growth & Design **19**, 3491 (2019).

[42] T. Hua, C. valentin valentin, O. Gowayed, S. Lee, B. A. Garetz, and R. L. Hartman, *Microfluidic laser-induced nucleation of supersaturated aqueous glycine solutions,* Crystal Growth & Design **20**, 6502 (2020).

[43] A. Sun, B. A. Garetz, and A. S. Myerson, *Supersaturation and polarization dependence of polymorph control in the nonphotochemical laser-induced nucleation (nplin) of aqueous glycine solutions,* Crystal Growth & Design **6**, 684 (2006).

[44] J. F. Lutsko and G. Nicolis, *Theoretical evidence for a dense fluid precursor to crystallization,* Physical Review Letters **96**, 046102 (2006).

[45] J. W. Mullin, *Crystallization*, Vol. 4 (Butterworth-Heinemann, 2001) pp. 181–215.

[46] W. D. Callister and D. G. Rethwisch, *Materials Science and Engineering: An Introduction*, Vol. 10 (Wiley, 2018) pp. 1–90.

[47] S. Dhingra, *Understanding Non-Photochemical Laser Induced Nucleation*, Master's thesis, Delft University of Technology (2017).

[48] A. S. Myerson, D. Erdemir, and A. Y. Lee, *Handbook of Industrial Crystallization*, Vol. 1 (Cambridge University Press, 2019) pp. 1–31.

[49] A. S. Myerson and B. L. Trout, *Nucleation from solution,* Science **341**, 855 (2013).

[50] R. J. Davey, S. L. M. Schroeder, and J. H. ter Horst, *Nucleation of organic crystals — a molecular perspective,* Angewandte Chemie international edition **52**, 2166 (2013).

[51] D. Gebauer, A. Volkel, and H. Colfen, *Stable prenucleation calcium carbonate clusters,* Science **322**, 1819 (2008).

[52] W. Pan, A. B. Kolomeisky, and P. G. Vekilov, *Nucleation of ordered solid phases of proteins via a disordered high-density state: Phenomenological approach,* The Journal of Chemical Physics **122**, (2005).

[53] W. Pan, P. G. Vekilov, and V. Lubchenko, *Origin of anomalous mesoscopic phases in protein solutions,* The Journal of Physical Chemistry B **114**, 7620 (2010).

[54] A. Lewis, M. Seckler, H. Kramer, and G. van Rosmalen, *Industrial Crystallization - Fundamentals and Applications*, Vol. 1 (Cambridge University Press, 2015) pp. 14–19.

[55] K. Fang, S. Arnold, and B. A. Garetz, *Nonphotochemical laser-induced nucleation in levitated supersaturated aqueous potassium chloride microdroplets,* Crystal Growth & Design **14**, 2685 (2014).

[56] M. R. Ward and A. J. Alexander, *Nonphotochemical laser-induced nucleation of potassium halides: Effects of wavelength and temperature,* Crystal Growth & Design **12**, 4554 (2012).

[57] H. H. Shi, Y. Xiao, S. Ferguson, X. Huang, N. Wang, and H. X. Hao, *Progress of crystallization in microfluidic devices,* Lab on a Chip , 2167 (2017).

[58] Y. E. Yu, L. Zhu, S. Shim, and J. Eggers, *Time-dependent motion of a confined bubble in a tube: transition between two steady states,* Journal of Fluid Mechanics **857**, R4 (2018).

[59] L. Kou, D. Labrie, and P. Chylek, *Refractive indices of water and ice in the 0.65- to 2.5-μm spectral range,* Applied Optics **32**, 3531 (1993).

[60] J. Matic, X. Sun, B. A. Garetz, and A. S. Myerson, *Intensity, wavelength, and polarization dependence of nonphotochemical laser-induced nucleation in supersaturated aqueous urea solutions,* Crystal Growth & Design **5**, 1565 (2005).

[61] J. Zaccaro, J. Matic, A. S. Myerson, and B. A. Garetz, *Nonphotochemical, laser-induced nucleation of supersaturated aqueous glycine produces unexpected γ-polymorph,* Crystal Growth & Design **1**, 5 (2000).

[62] M. R. Ward, A. M. Mackenzie, and A. J. Alexander, *Role of impurity nanoparticles in laser-induced nucleation of ammonium chloride,* Crystal Growth & Design **16**, 6790 (2016).

[63] M. R. Ward, I. Ballingal, M. L. Costen, K. G. McKendrick, and A. J. Alexander, *Nanosecond pulse width dependence of nonphotochemical laser-induced nucleation of potassium chloride,* Chemical Physics Letters **481**, 25 (2009).

[64] A. J. Alexander and P. J. Camp, *Single pulse, single crystal laser-induced nucleation of potassium chloride,* Crystal Growth & Design **9**, 958 (2009).

[65] M. R. Ward, A. Rae, and A. J. Alexander, *Nonphotochemical laser-induced crystal nucleation by an evanescent wave,* Crystal Growth & Design **15**, 4600 (2015).

[66] J. A. Jacob, S. Sorgues, A. Dazzi, A. Mostafavi, and J. Belloni, *Homogeneous nucleation–growth dynamics induced by single laser pulse in supersaturated solutions,* Crystal Growth & Design **12**, 5980 (2012).

[67] I. S. Lee, J. M. B. Evans, D. Erdermir, A. Y. Lee, B. A. Garetz, and A. S. Myerson, *Nonphotochemical laser induced nucleation of hen egg white lysozyme crystals,* Crystal Growth & Design **8**, 4255 (2008).

[68] W. Li, A. Ikni, P. Scouflaire, X. Shi, N. El Hassan, P. Gemeiner, J. M. Gillet, and A. Spasojevic-de Bire, *Non-photochemical laser-induced nucleation of sulfathiazole in a water/ethanol mixture,* Crystal Growth & Design **16**, 2514 (2016).

[69] A. Ikni, B. Clair, P. Scouflaire, P. Veesler, J. M. Gillet, N. El Hassan, F. Dumas, and A. Spasojevic-de Bire, *Experimental demonstration of the carbamazepine crystallization from non-photochemical laser-induced nucleation in acetonitrile and methanol,* Crystal Growth & Design **14**, 3286 (2014).

[70] B. C. Knott, J. L. LaRue, A. M. Wodtke, A. M. Doherty, and B. Peters, *Communication: bubbles, crystals, and laser-induced nucleation,* The Journal of Chemical Physics **134**, 171102 (2011).

[71] M. R. Ward, W. J. Jamieson, C. A. Leckey, and A. J. Alexander, *Laser-induced nucleation of carbon dioxide bubbles,* The Journal of Chemical Physics **142**, 144501 (2015).

[72] N. Javid, T. Kendall, I. S. Burns, and J. Sefcik, *Filtration suppresses laser-induced nucleation of glycine in aqueous solutions,* Crystal Growth & Design **16**, 4196 (2016).

[73] B. A. Garetz, J. Matic, and A. S. Myerson, *Polarization switching of crystal structure in the non-photochemical light–induced nucleation of supersaturated aqueous glycine solutions,* Physical Review letters **89**, 175501 (2002).

[74] D. W. Oxtoby, *Crystals in a flash,* Nature **420**, 277 (2002).

[75] X. Sun, *Polymorph control in nonphotochemical light-induced nucleation and optical Kerr study*, Ph.D. thesis, Polytechnic University (2008).

[76] Y. Liu, M. H. van den Berg, and A. J. Alexander, *Supersaturation dependence of glycine polymorphism using laser-induced nucleation, sonocrystallization and nucleation by mechanical shock,* Physical Chemistry Chemical Physics **19**, 19386 (2017).

[77] D. Irimia, J. J. Shurley, A. S. Garg, D. P. A. Nijland, A. E. D. M. van der Heijden, H. J. M. Kramer, and H. B. Eral, *Influence of laser parameters and experimental conditions on nonphotochemical laser-induced nucleation of glycine polymorphs,* Crystal Growth & Design **21**, 631 (2021).

[78] B. C. Knott, M. F. Doherty, and B. Peters, *A simulation test of the optical kerr mechanism for laser-induced nucleation,* The Journal of Chemical Physics **134**, 154501 (2011).

[79] J. O. Osard, *Calculation of the influence of an electric field on the free energy of formation of a nucleus,* The Philosophical Magazine: A Journal of Theoretical Experimental and Applied Physics **35**, 817 (1977).

[80] V. B. Warshavsky and A. K. Shchekin, *The effects of external electric field in thermodynamics of formation of dielectric droplet,* Colloids and Surfaces A: Physicochemical and Engineering Aspects **148**, 283 (1999).

[81] M. Ildefonso, N. Candoni, and S. Veesler, *Heterogeneous nucleation in droplet–based nucleation measurements,* Crystal Growth & Design **13**, 2107 (2013).

[82] S. V. Akelka, A. Mowitz, M. Heymann, and S. Fraden, *Emulsion-based technique to measure protein crystal nucleation rates of lysozyme,* Crystal Growth & Design **14**, 4487 (2017).

[83] N. Candoni, R. Grossier, M. Lagaize, and S. Veesler, *Advances in the use of microfluidics to study crystallization fundamentals,* Annual review chemical biomolecular engineering **10**, 59 (2019).

[84] L. Li, D. Mustafi, Q. Fu, V. Tereshko, D. L. Chen, J. D. Tice, and R. F. Ismagilov, *Nanoliter microfluidic hybrid method for simultaneous screening and optimization validated with crystallization of membrane proteins,* Proceedings of the National Academy of Sciences of the United States of America **103**, 19243 (2006).

[85] J. U. Shim, G. Cristobal, L. D.R., T. Thorsen, and S. Fraden, *Using microfluidics to decouple nucleation and growth of protein crystals,* Crystal Growth & Design **7**, 2192 (2007).

[86] T. M. Squires and S. R. Quake, *Microfluidics: Fluid physics at the nanoliter scale,* Reviews of Modern Physics **77**, 977 (2005).

[87] J. Leng and J. B. Salmon, *Microfluidic crystallization,* Lab on a Chip **9**, 24 (2009).

[88] E. Candida dos Santos, G. M. Maggioni, and M. Mazzotti, *Statistical analysis and nucleation parameter estimation from nucleation experiments in flowing microdroplets,* Crystal Growth & Design **19**, 6159 (2019).

[89] C. N. Baroud, F. Gallaire, and R. Dangla, *Dynamics of microfluidic droplets,* Lab Chip **16**, 2032 (2010).

[90] G. Christoper and S. L. Anna, *Microfluidic methods for generating continuous droplet streams,* Journal of Physics D: Applied Physics **40**, R319 (2007).

[91] Y. M. Harshe, M. J. van Eijk, C. R. Kleijn, M. T. Kreutzer, and P. E. Boukany, *Scaling of mixing time for droplets of different sizes traveling through a serpentine microchannel,* RSC Advances **6**, 98812 (2006).

[92] B. M. A. Wolffenbuttel, T. A. Nijhuis, A. Stankiewicz, and J. A. Moulijn, *Novel method for non-intrusive measurement of velocity and slug length in two- and three-phase slug flow in capillaries,* Measurement Science and Technology **13**, 1540 (2002).

[93] A. Conlisk, *Introduction to microfluidics. by patrick tabeling. oxford university press, 2005. 312 pp. isbn 019 856864 9.* Journal of Fluid Mechanics **570**, 503 (2007).

[94] C. N. Baroud and H. Willaime, *Multiphase flows in microfluidics - Écoulements de fluides non miscibles dans des systèmes microfluidiques,* Comptes Rendus Physique **5**, 547 (2004).

[95] N. Convery and N. Gadegaard, *30 years of microfluidics,* Micro and Nano Engineering **2**, 76 (2019).

[96] Solvay, *Fomblin pfpe: Vacuum pump oils,* (2020), retrieved from `https://www.solvay.com/sites/g/files/srpend221/files/2018-10/Fomblin-PFPE-Lubes-for-Vaccum-Applications_EN-v2.7_0.pdf`.

[97] Darwin-Microfluidics, *Choosing the best oil and surfactant for droplet generation,* (2020), retrieved from `https://darwin-microfluidics.com/blogs/reviews/choosing-the-good-oil-for-microfluidics`.

[98] S. Y. Teh, R. Lin, L. H. Hung, and A. P. Lee, *Droplet microfluidics,* Lab on a Chip **2**, 198 (2008).

[99] R. M. Lorenz, G. S. Fiorini, G. D. M. Jeffries, D. S. W. Lim, M. He, and D. T. Chiu, *Simultaneous generation of multiple aqueous droplets in a microfluidic device,* Analytica Chimica Acta **630**, 124 (2008).

[100] T. W. Yu, *Kidnes Stones in μ-Reactors - Design/production of microfluidic devices for induction time experiments and a comparison between laboratory and micro scale reactors*, Master's thesis, Delft University of Technology (2019).

[101] S. M. Shor, *Effects of surfactants and inorganic additives on nucleation kinetics in mixed suspension crystallization*, Ph.D. thesis, Iowa State University (1970).

[102] D. Han, Y. Wang, Y. Yang, T. Gong, Y. Chen, and J. Gong, *Revealing the role of a surfactant in the nucleation and crystal growth of thiamine nitrate: experiments and simulation studies,* CrystEngComm **21**, 3576 (2019).

[103] B. N. Laboratory, *Chemical compatibility of the tubing materials,* (2020), retrieved from `https://www.bnl.gov/esh/shsd/PDF/Compressed_gas/Chem_Comp_Tubing_Material.pdf`.

[104] H. A. Technologies, *Masterflex tubing chemical compatibility tables,* (2020), retrieved from `https://www.hollandapt.com/Documents/Ctrl_Hyperlink/Masterflex_Tubing_Chemcial_Compatability_uid172010827381.pdf`.

[105] M. J. Goudie, J. Pant, and H. Handa, *Liquid-infused nitric oxide-releasing (linorel) silicone for decreased fouling, thrombosis, and infection of medical devices,* Scientific Reports **7**, 13623 (2017).

[106] Norell, *Ptfe tubing (polytetrafluoroethylene),* (2020), retrieved from `https://nmrtubes.com/ptfe-tubing.php`.

[107] Curbell-Plastics, *Ptfe tubing - chemically resistant, low coefficient of friction, with a broad temperature range -454 f to 500 f,* (2020), retrieved from `https://www.curbellplastics.com/Research-Solutions/Specialty-Products/Tubing-and-Hose/PTFE-Tubing`.

[108] A. R. Abate, D. Lee, T. Do, C. Holtze, and D. A. Weitz, *Glass coating for pdms microfluidic channels by sol–gel methods,* Lab on a Chip **4**, 516 (2008).

[109] L. Mazutis, J. Gilbert, W. L. Ung, D. A. Weitz, A. D. Griffiths, and J. A. Heyman, *Single-cell analysis and sorting using droplet-based microfluidics,* Nature Protocols **8**, 870 (2013).

[110] D. Sriramulu, E. L. Reed, M. Annamalai, T. V. Venkatesan, and S. Valiyaveettil, *Synthesis and characterization of superhydrophobic, self-cleaning nir-reflective silica nanoparticles,* Scientific reports **6**, 35993 (2016).

[111] M. Z. Khan, J. Militky, V. Baheti, J. Wiener, and M. Vik, *Development of durable superhydrophobic and uv protective cotton fabric via tio2/trimethoxy(octadecyl)silane nanocomposite coating,* The Journal of The Textile Institute **0**, 1 (2020).

[112] H. Salim, P. Kolpakov, D. Bonn, and N. Shahidzadeh, *Self-lifting nacl crystal,* The Journal of Physical Chemistry Letters **11**, 7388 (2020).

[113] S. Ambhorkar, *Ostwald Ripening in Elastic Media*, Master's thesis, Delft University of Technology (2019).

[114] M. U. Javaid, T. A. Cheema, and C. W. Park, *Analysis of passive mixing in a serpentine microchannel with sinusoidal side walls,* Micromachines **9**, 8 (2018).

[115] R. H. Liu, M. A. Stremler, K. V. Sharp, M. G. Olsen, J. G. Santiago, A. R. J., H. Aref, and D. J. Beebe, *Passive mixing in a three-dimensional serpentine microchannel,* Journal of Microelectromechanical Systems **9**, 190 (2000).

[116] N. R. Rosaguti, D. F. Fletcher, and B. S. Haynes, *Laminar flow and heat transfer in a periodic serpentine channel with semi-circular cross-section,* International Journal of Heat and Mass Transfer **49**, 2912 (2006).

[117] G. M. Hale and M. Querry, *Optical constants of water in the 200-nm to 200-μm wavelength region,* Applied Optics **12**, 555 (1973).

[118] N. Hidman, G. Sardina, D. Maggiolo, H. strom, and S. Sasic, *Numerical frameworks for laser-induced cavitation: Is interface supersaturation a plausible primary nucleation mechanism?* Crystal Growth & Design **20**, 7276 (2020).

[119] C. Li, *Nonlinear Absorption and Refraction of Light. In: Nonlinear Optics*, Vol. 1 (Springer, 2017) pp. 177–214.

[120] S. D. Shingte, *The study of the influence of mixing on the induction time in microfluidics*, Master's thesis, Delft University of Technology (2017).

[121] P. Laval, J. Salmon, and M. Joanicot, *A microfluidic device for investigating crystal nucleation kinetics,* Journal of Crystal Growth **303**, 622 (2007).

[122] X. Sun, B. A. Garetz, and A. S. Myerson, *Polarization switching of crystal structure in the non-photochemical laser-induced nucleation of supersaturated aqueous l-histidine,* Crystal Growth & Design **8**, 1720– (2008).

[123] Engineering-Toolbox, *Density of aqueous solutions of inorganic potassium salts,* (2021), retrieved from `https://www.engineeringtoolbox.com/density-aqueous-solution-inorganic-potassium-salt-concentration-d_1956.html`.

[124] W. Bogacz, M. H. Al-Rashed, M. Lemanowicz, and J. Wojcik, *A simple densimetric method to determine saturation temperature of aqueous potassium chloride solution,* Journal of Solution Chemistry **45**, 1071 (2016).

[125] H. L. Zhang and S. J. Han, *Viscosity and density of water + sodium chloride + potassium chloride solutions at 298.15 k,* Journal of Chemical & Engineering Data **41**, 516 (1996).

[126] Galden, *Data sheet galden sv110. cas-no. : 69991-67-9. version 1.03,* (2021), retrieved from SOLVAY SPECIALTY POLYMERS ITALY S.p.A. June 2019.

[127] Mercks, *Data sheet silicone oil viscosity 10 cst,* (2021), retrieved from `https://www.sigmaaldrich.com/catalog/product/aldrich/378321?lang=en&region=NL`.

[128] Schott-Duran, *Duran borosilicate glass 3.3 physical and chemical properties,* (2020), retrieved from private communication with `www.vitrocom.com`.

Appendices contents

A

Appendix A

This chapter starts off with presenting the dimensionless numbers used to characterize the previous and improved system, followed by the results of the tubing compatibility test and the hydrophobization protocols considered to hydrophobically coat the square borosilicate capillaries. The quality and hydrophobicity of these capillaries was tested. The results of which can be found after the presentation of the hydrophobization protocols. Ending this appendix with images of both the old and the improved desiccator, used to hydrophobically coat the capillaries, and an image showing an overview of the improved microfluidic system used within this study.

A.1. Dimensionless Numbers

This section presents the formulas of the dimensionless numbers together with their results, used to characterize both the the previously designed system as well as the improved system.

Table A.1: Dimensionless numbers, and their formulas, used to characterize both the previously designed system and the improved microfluidic system.

Dimensionless Number	**Formula**	**Previous System** [16]	**Improved System**
Re	$\frac{\rho v d}{\mu}$	3.02	2.92
Ca	$\frac{\mu v}{\gamma}$	$4.66 \cdot 10^{-4}$	$4.49 \cdot 10^{-4}$
Bo	$\frac{\Delta\rho g d^2}{\gamma}$	$6.54 \cdot 10^{-7}$	$5.19 \cdot 10^{-7}$
We	$\frac{\rho v^2 d}{\gamma}$	$1.41 \cdot 10^{-3}$	$1.31 \cdot 10^{-3}$

A.1.1. Dimensionless Numbers Parameters

Tables A.2 & A.3 display the parameters used in the calculations of the dimensionless numbers listed in Table A.1.

A.1.2. Previous System

Table A.2: Parameter values used in the calculation of the dimensionless numbers characterizing the designed microfluidic system [16].

Parameter	**Value**	**Unit**	**Obtained from**
$\rho_{\mathrm{KCl(aq)}}$	$1.275 \cdot 10^{-3}$	g/mm^3	Extrapolated from [123, 124]
v_{average}	2.547	mm/s	Average velocity in all measurements
d	0.9	mm	Capillary diameter
μ	$0.9662 \cdot 10^{-3}$	g/mm·s	Value at saturation [125]
γ	5.283	$mJ/m^2 = g/s^2$	Experimental result obtained by Ward et al. [56]
ρ_{PFPE}	$1.71 \cdot 10^{-3}$	g/mm^3	PFPE data sheet [126]
$\Delta\rho$	$4.35 \cdot 10^{-4}$	g/mm^3	ρ_{PFPE} - $\rho_{\mathrm{KCl(aq)}}$
g	$9.81 \cdot 10^{-3}$	mm/s^2	

A.1.3. Improved System

Table A.3: Parameter values used in the calculation of the dimensionless numbers characterizing the improved microfluidic system.

Parameter	Value	Unit	Obtained from
$\rho_{\text{KCl(aq)}}$	$1.275 \cdot 10^{-3}$	g/mm^3	Extrapolated from [123, 124]
v_{average}	2.457	mm/s	Average velocity all measurements
d	0.9	mm	Capillary diameter
μ	$0.9662 \cdot 10^{-3}$	g/mm·s	Value at saturation [125]
γ	5.283	mJ/m^2 = g/s^2	Experimental result obtained by Ward et al. [56]
$\rho_{\text{Silicon Oil}}$	$0.93 \cdot 10^{-3}$	g/mm^3	Silicon oil data sheet [127]
$\Delta\rho$	$3.25 \cdot 10^{-4}$	g/mm^3	$\rho_{\text{KCl(aq)}} - \rho_{\text{Silicon Oil}}$
g	$9.81 \cdot 10^{-3}$	mm/s^2	

A.2. Tubing Compatibility Test

The following sections presents the results of the tubing compatibility tests carried out with each of the tubing options. For each tubing option first the results after 3 hours are presented, followed by the results after 24 hours.

A.2.1. PTFE

Table A.4: Results of the experiment testing the compatibility of the PTFE tubing with PFPE after 3 hours.

Label	Mass start (g)	Mass end (g)	Mass increase (%)
A	0.19729	0.19796	0.3396
B	0.18442	0.18507	0.3525
C	0.17406	0.17478	0.4137
Average			0.3686

Table A.5: Results of the experiment testing the compatibility of the PTFE tubing with PFPE after 24 hours.

Label	Mass start (g)	Mass end (g)	Mass increase (%)
A	0.21609	0.21804	0.9024
B	0.19434	0.19616	0.9365
C	0.18173	0.18348	0.9630
Average			0.9340

A.2.2. Silicone Oil

Table A.6: Results of the experiment testing the compatibility of the PTFE tubing with Silicone oil after 3 hours.

Label	Mass start (g)	Mass end (g)	Mass increase (%)
A	0.19714	0.19749	0.1775
B	0.18702	0.18685	-0.0909
C	0.18628	0.19736	0.5798
Average			0.2221

Table A.7: Results of the experiment testing the compatibility of the PTFE tubing with Silicone oil after 24 hours.

Label	Mass start (g)	Mass end (g)	Mass increase (%)
A	0.21422	0.21457	0.1634
B	0.17066	0.17102	0.2109
C	0.19668	0.19688	0.1017
Average			0.1587

A.2.3. HFE

Table A.8: Results of the experiment testing the compatibility of the PTFE tubing with HFE after 3 hours.

Label	**Mass start (g)**	**Mass end (g)**	**Mass increase (%)**
A	0.18014	0.18087	0.4052
B	0.19739	0.19736	-0.0152
C	0.19669	0.19792	0.4874
Average			0.2925

Table A.9: Results of the experiment testing the compatibility of the PTFE tubing with HFE after 24 hours.

Label	**Mass start (g)**	**Mass end (g)**	**Mass increase (%)**
A	0.20209	0.20404	0.9649
B	0.19602	0.19798	0.9999
C	0.18459	0.18643	1.0185
Average			0.9944

A.3. Hydrophobization Protocols

In this section the three different protocols used to hydrophobically coat the capillaries used in the microfluidic set-up for NPLIN experiments are presented.

A.3.1. Trichloro(1H,1H,2H,2H-perfluoroctyl)-silane

The following steps were taken to hydrophobically coat the glass capillary for experimental use:

- Flush the inside of the capillary with 10 mL of 0.1M Sodium hydroxide (NaOH) solution.
- Rinse the the inside of the capillary with 20 mL of ultra pure water.
- Dry the capillary using a paper towel.
- Dry the inside of the capillary with pressurized nitrogen gas.
- Add 16 μL of trichloro(1H,1H,2H,2H-perfluoroctyl)-silane to a 1.5 mL glass vial and close it.
- Insert the capillary into the 1.5 mL glass vial trough a hole in its cap.
- Place the vial with the inserted capillary into the improvised desiccator.
- Close off the desiccator in the fume hood, reduce the pressure to <30 mbar and leave to sit overnight (>12 hours).
- Carefully return the desiccator to atmospheric pressure, open it in the fume hood and let it sit for a few minutes for any residual trichloro(1H,1H,2H,2H-perfluoroctyl)-silane to evaporate.
- Wipe the capillary with isopropanol, repeat with acetone and flush with pressurized nitrogen gas to ensure any residue of trichloro(1H,1H,2H,2H- perfluoroctyl)-silane is removed from the capillary.

A.3.2. Aquapell

Take the following steps for the preparation of the Aquapel water-repellent and subsequent coating of the glass capillary with the Aquapel solution:

- Aquapel solution is supplied in a glass ampule embedded in a plastic cartridge with a thick felt pad. Carefully cut the pad and remove the ampule.
- Transfer the glass ampule to a 50-mL Falcon-type conical plastic tube, carefully break the ampule inside it and close the top cap to avoid evaporation of the Aquapel solution.
- Transfer the Aquapel solution to a syringe for use in the hydrophobization procedure or carefully fill the 50-mL Falcon-type conical plastic tube with nitrogen and seal the tube with parafilm for storage.
- Connect a series of capillaries using silicone tubing, as to form a column of capillaries.
- Connect a syringe with Aquapell to this column of capillaries by use of a piece of silicone tubing and a microfluidic tip.
- Slowly inject the capillaries with Aquapel, such that the solution sits for a total of approximately 30-60 seconds in each capillary.
- Expel Aquapel from the capillaries by forcing air through it, using for example an empty syringe.
- Flush the capillaries with Fluorinert FC-40 oil to remove any residual Aquapel.
- Expel Fluorinert FC-40 oil, by forcing air through the capillaries using a syringe.
- Bake the capillaries at 65 °C for 20 minutes.
- Remove the capillaries from the oven and let cool to room temperature.
- Clean the outside of the capillaries with a paper towel and flush with pressurized nitrogen gas to ensure all solution is removed.

A.3.3. Trimethoxy(octadecyl)silane

The steps listed below were taken to hydrophobically coat the glass capillary by use of trimethoxy-(octadecyl)silane:

- Pour Roughly 5 mL toluene into a beaker and weigh.
- Add trimethoxy(octadecyl)silane, using a pipette, to the toluene beaker, such that the mass ratio between toluene and silane is 100:1.
- Swirl the beaker for roughly a minute and shortly stir with a spatula to manually mix its contents.
- Fill 2 1.5 mL glass vials to the top with the toluene/silane solution, close the vials off with a cap.
- Fill the capillary with the solution using a piece of silicone tubing, a needle and a syringe.
- Insert the capillary into the first 1.5 mL glass vial trough a hole in its cap, carefully ensuring no solution is lost from the capillary.
- Detach the silicone tubing without losing any solution and seal the other end of the capillary off with the second 1.5 mL vial.
- Let the filled and sealed capillary sit for approximately 1 hour.
- Remove the capillary from the 1.5 mL vials, empty its contents into an oven proof tray and place the capillary onto the tray.
- Place the tray in an 110 °C oven and let sit for 4 hours.
- Remove tray from the oven, wipe the outside of the capillary with a paper towel, flush the inside with methanol and dry using pressurized nitrogen gas to ensure all solution is removed.

A.4. Hydrophobization test - Contact Angle tests

This section begins with listing the preparation and testing procedure of the capillary for the contact angle tests, followed by a presentation of the results of these contact angle tests.

A.4.1. Preparation and Testing Procedure

Equipment set-up

- Fit a piece of 1 mm ID silicone tubing with a small inner capillary and insert this into the straight end of a T-junction, securing it in place using a ferrule and a microfluidic fitting. This produces the dispersed phase in the microfluidic set-up.
- Fit a microfluidic syringe tip the other side of the piece of 1 mm ID silicone tubing.
- Connect a second piece of 1 mm ID silicone tubing to the T-junction, securing it in place using a ferrule and a microfluidic fitting, and fit the other side of the tubing with a microfluidic syringe tip. This produces the continuous phase in the microfluidic set-up.
- Connect the last opening of the T-junction to a third piece of 1 mm ID silicone tubing, again securing it in place using a ferrule and a microfluidic fitting. This forms the outlet stream of the system. The outlet stream will be connected tot the square coated capillary to generate water droplets within it.
- Connect a 10 mL syringe filled with water to the inlet tip of the dispersed phase and place the syringe in a syringe pump.
- Connect a second 10 mL syringe filled with air to the inlet tip of the continuous phase and place the syringe in a second syringe pump.

Preparation Procedure:

- Set the flow rate of the dispersed phase to 20 μL/min and that of the continuous phase to 200 μL/min.
- Let the set-up run for approximately 5 minutes to stabilize and form droplets of constant volume.
- Connect the capillary to the outlet stream and let the set-up run until (at least) 5 droplets have formed within the capillary.
- Disconnect the capillary from the set-up and stop the syringe pumps.
- Carefully move the formed water droplets to approximately the middle of the capillary. using a piece of 1 mm ID silicone tubing, a microfluidic syringe tip and an empty syringe.
- Analyze the droplets using an optical contact angle measuring and contour analysis system and the accompanying software, by manually drawing a baseline and a tangent at the three phase point to define and calculate the contact angle.
- Repeat for each capillary.

A.4.2. Contact Angle Measurement Results

The following sections present the results of contact angle measurements performed on both unhydrophobized capillaries as well as capillaries coated using the protocols presented in the previous sections.

Unhydrophobized

Table A.10: Experimentally determined contact angles in three different unhydrophobized capillaries.

Measurement number	**Capillary 1 (°)**	**Capillary 2 (°)**	**Capillary 3 (°)**
1	47.4	50.5	48.7
2	37.5	45.0	42.4
3	45.1	53.6	50.0
4	44.8	48.3	54.8
5	47.8	44.8	50.8
6	53.3	45.1	47.2
7	41.7	54.8	48.9
8	42.7	51.7	47.9
9	41.2	41.7	49.6
10	38.8	55.5	48.1
Average	44.0 ± 4.7	49.1 ± 4.8	48.8 ± 8.5

Trichloro(1H,1H,2H,2H-perfluoroctyl)-silane

Table A.11: Experimentally determined contact angles (in degrees) in three different capillaries for capillaries coated using trichloro(1H,1H,2H,2H-perfluoroctyl)-silane.

Measurement number	**Capillary 1 (°)**	**Capillary 2 (°)**	**Capillary 3 (°)**
1	102.6	102.2	100.8
2	101.6	98.4	110.8
3	99.2	97.7	102.1
4	94.7	96.0	100.3
5	102.1	100.3	97.2
6	102.6	96.8	115.5
7	97.7	97.7	105.2
8	102.8	98.8	103.0
9	109.6	100.3	101.8
10	100.6	101.4	107.8
Average	101.3 ± 3.9	99.0 ± 2.0	104.5 ± 5.5

Aquapell

Table A.12: Experimentally determined contact angles (in degrees) in three different capillaries for capillaries coated using Aquapell.

Measurement number	**Capillary 1 (°)**	**Capillary 2 (°)**	**Capillary 3 (°)**
1	112.4	105.7	111.6
2	105.9	98.6	108.8
3	105.1	109.7	100.2
4	102.1	99.7	104.4
5	106.7	102.1	108.2
6	104.2	98.4	104.4
7	109.3	111.7	110.8
8	101.4	103	104.5
9	100.1	102.0	103.8
10	106.2	100.1	104.1
Average	105.3 ± 3.7	103.1 ± 4.6	106.1 ± 4.1

Trimethoxy(octadecyl)silane

Table A.13: Experimentally determined contact angles (in degrees) in three different capillaries for capillaries coated using Trimethoxy(octadecyl)silane.

Measurement number	**Capillary 1 (°)**	**Capillary 2 (°)**	**Capillary 3 (°)**
1	80.8	85.6	82.5
2	86.8	72.6	69.4
3	73.4	65.9	85.4
4	81.7	75.3	70.7
5	77.7	84.7	79.7
6	73.1	70.4	76.4
7	75.7	68.2	73.4
8	70.3	72.6	78.3
9	74.4	80.5	85.7
10	69.6	69.1	73.7
Average	76.4 ± 5.4	74.5 ± 6.9	77.5 ± 5.8

Fresh Aquapel

Table A.14: Experimentally determined contact angles (in degrees) in three different capillaries for capillaries coated using fresh Aquapel.

Measurement number	**Capillary 1 (°)**	**Capillary 2 (°)**	**Capillary 3 (°)**
1	103.2	103.3	110.5
2	101.3	98.4	102.9
3	113.0	103.7	111.1
4	109.3	110.4	105.2
5	108.9	100.6	103.2
6	106.9	104.9	106.4
7	98.7	110.6	106.0
8	109.7	106.7	109.8
9	96.1	97.3	104.2
10	102.3	107.1	104.3
Average	104.9 ± 5.4	104.3 ± 4.6	106.4 ± 4.4

A.5. Hydrophobization equipment - Improved Desiccator

This section presents a comparative image (Figure A.1) between the improvised desiccator used in the previous study (Figure A.1a) and the improved desiccator used within this study (Figure A.1b).

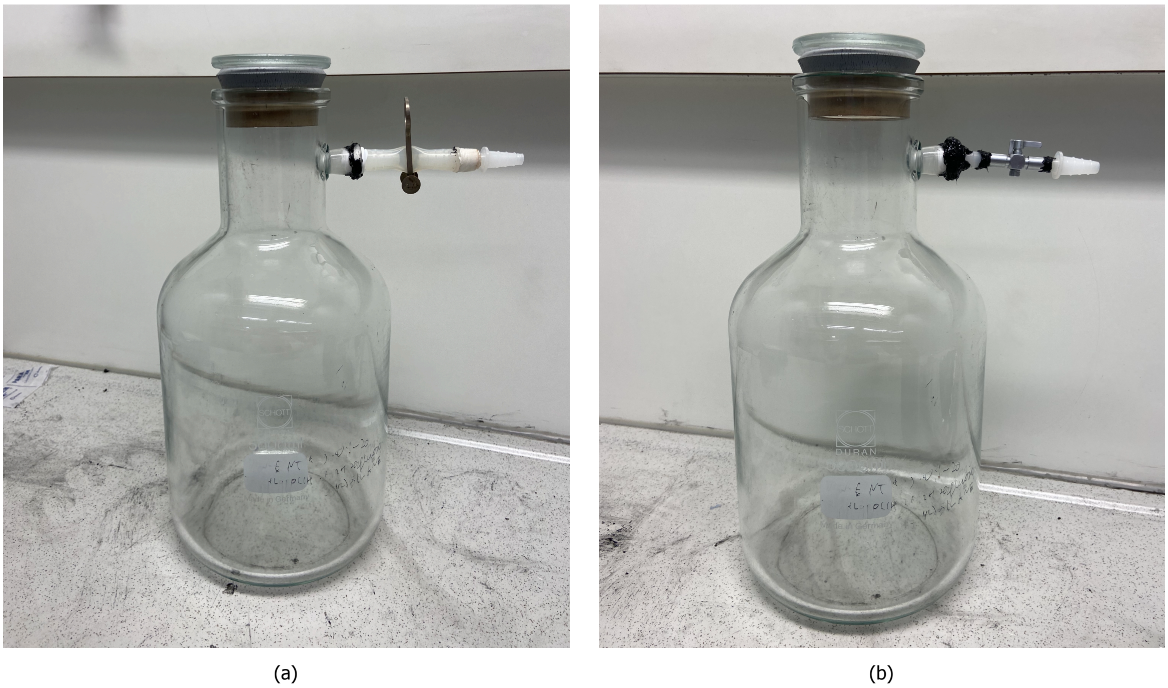
(a)

(b)

Figure A.1: (a) Improvised desiccator used in the previous study to hydrophobize capillaries. (b) Improved desiccator used within this study to to hydrophobize capillaries.

A.6. Overall Improved Microfluidic System

This section presents an overview image (Figure A.2) of the entire microfluidic system used within this study.

1. Continuous phase pump
2. Dispersed phase pump
3. Mixing Zone
4. T-junction
5. Temperature controlled environment
6. Arduino microcontroller – IR sensor
7. Part of the laser directing set-up
8. Square Capillary
9. Microscopic Camera & Objective
10. Led Light

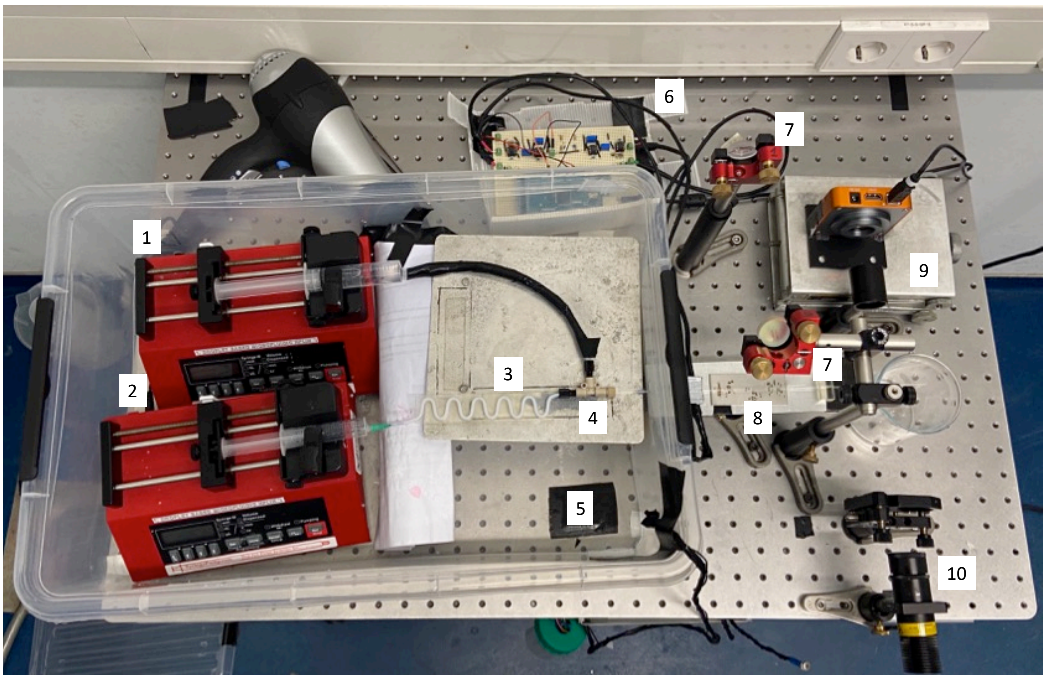

Figure A.2: Image of the overall improved system. Located on the top left is the continuous phase syringe pump, with the dispersed phase syringe pump on the bottom left. The dispersed phase is pumped into the mixing, connected to the t-junction. Droplet generation takes place directly within the square capillary, connected to the outlet of the t-junction. All of the aforementioned equipment's are located within the temperature controlled environment. Droplets generated in the square capillary traveled out of the temperature controlled environment and were irradiated with a laser beam by use of the mirrors and then imaged by the microscopic camera.

B

Appendix B

The chapter begins by presenting the testing procedures used within this study as well as the solution preparation data for the supersaturated solutions, followed by the calculations of power meter readings for the desired laser intensity. Subsequently, the results of the control cooling and laser irradiation experiments for all wavelengths are presented. The chapter is then ended by presentation of the capillary transmission spectrum and two Matlab codes used in the analysis of the IR and temperature sensor data.

B.1. Testing Procedures

This section presents both the procedure used to prepare and store the supersaturated solutions as well as the procedure used to start and run the microfluidic system. Followed by the solution preparation data for the supersaturated solutions used in the laser irradiation experiments.

B.1.1. Supersaturated Solution Preparation & Storage Procedure

- Clean glass bottle intended for storing the supersaturated solution and a stirring bar using iso-propanol, aceton and demi-water.
- Weigh out the glass bottle and re-calibrate the weighing scale with the weight of the glass bottle included.
- Weigh out the specified amount of demi-water needed for the supersaturated solution and close the glass bottle using a seal cap.
- Weigh out the specified amount of KCl and, slowly without spilling, add this to the glass bottle filled with water.
- Add a stirring bar and seal the glass bottle using a layer of parafilm and a seal cap. Sealing the glass bottle using two barriers minimizes the chances of solvent loss during storage and maintains the concentration (and therefore supersaturation) of the solution.
- Heat and stir the solution at 50 °C until all KCl has dissolved.
- Remove the stirring bar from the glass storage bottle, reseal the glass bottle with a layer of parafilm and a seal cap. Store the prepared solution in an oven at 50 °C to ensure all KCl remains dissolved.
- Minimize solvent loss to maintain a constant KCl concentration by minimizing the amount of time the bottle is opened as well as ensuring the bottle remains properly sealed.

B.1.2. Experimental Protocol

- Wrap a small piece of silicon tubing around the 0.9 mm inner diameter square borosilicate capillary, and insert this side into a ferrule. Subsequently, connect the square borosilicate capillary to a T-junction by use of a microfluidic fitting, ensuring the capillary lies completely flat to the T-junction to optimize imaging of the capillary as well as ensure the laser hits a flat service.
- Insert the inner capillary into the mixing zone outlet and connect this outlet to the T-junction by use of a ferule and a microfluidic fitting. Connect the continuous phase tubing in a similar manner.

- Guide the square borosilicate capillary through the outlet of the temperature controlled environment and connect it to the T-junction by use of a ferule and a microfluidic fitting. Ensure the square borosilicate capillary is pointed (slightly) downwards at the outlet of the temperature controlled environment, easing the flow of both the continuous and dispersed phase. This step seems to be critical for a consistent droplet distribution.
- Place the the square borosilicate capillary outside of the temperature controlled environment in both the IR sensor holder, placed roughly 3-4 cm from the wall of temperature controlled environment, as well as a second sensor holder, placed 2-3 cm from the end of the capillary platform. Using both sensor holders ensures the capillary remains as straight as possible over the course of the capillary platform, easing the flow through the capillary. Similar to the previous step, this step seems to be critical for a consistent droplet distribution.
- After connecting all tubing, hang a small soldering wire from the end of the capillary to ensure all fluid drips down smoothly, this avoids clogging of the capillary.
- Pre-heat the temperature controlled environment for 45-60 minutes before starting the measurement. Ensure the continuous phase silicon oil 20 mL syringe is placed in the syringe pump holder in the temperature controlled environment, during this pre-heat period. Also Place a 10 mL syringe filled with pre-heated demi-water in the dispersed phase syringe pump holder and allow it to fill the mixing zone by letting this syringe pump operate at 310 μL/min for 1 minute. This ensures the tubing at the dispersed phase inlet is properly pre-heated and pre-saturated with water, to avoid solvent loss during connection of the dispersed phase solution to the inlet port.
- Supersaturated aqueous KCl solutions were stored in glass bottles in an oven at 50 °C, sealed by parafilm and a sealed cap to minimize evaporation and solvent loss. Solutions should be shaken maximally 15-20 minutes before extracting.
- Remove the cap and the parafilm from the glass storage bottle and use a pre-heated 10 mL syringe with a pre-heated needle to extract the supersaturated aqueous KCl solution. Reseal the glass storage bottle after extracting the solution with a layer of parafilm and its seal cap. Place the bottle back into a 50 °C oven.
- Remove the needle from the pre-heated 10 mL syringe and wrap a small layer of parafilm over its outlet, sealing the solution in the syringe. Place the syringe back in the oven for 5 minutes to allow any solids possibly formed during solution extraction to redissolve.
- Retrieve the 10 mL syringe from the oven after 5 minutes, place it in the dispersed phase syringe pump holder, connect it to the pre-heated and saturated dispersed phase inlet port and wait 5 minutes to let the system stabilize. During this waiting period, wrap a small layer of parafilm around this connection point as to seal it. This avoids possible solvent loss and prevents air from possibly entering the dispersed phase channel.
- After the waiting period, start the continuous phase syringe pump at 500 μL/min for 2 minutes or until the continuous phase can be seen dripping from the capillary end. Doing so ensures that the capillary is properly wetted with the continuous phase before the dispersed phase solution enters the capillary.
- After the capillary is properly wetted, maintain the continuous phase at 500 μL/min and start the dispersed phase flow rate at 310 μL/min. Run the system at these high flow rates for 2 minutes, to ensure the entire mixing zone is filled with supersaturated aqueous KCl solution. Thus, droplets formed no longer consist of water but of supersaturated aqueous KCl solution.
- Decrease the dispersed phase flow rate to 10 μL/min, whilst maintaining the continuous phase flow rate at a high 500 μL/min for 1 minute to remove the large amount of droplets formed in the capillary from the system.
- Decrease the continuous phase flow rate to 100 μL/min, such that both flow rates are now at their desired rate for the experiment.
- Let the system run for 10-15 minutes to ensure a stable system is formed and any potential disruptions caused during the set-up are minimized before starting the measurement.

B.1.3. Supersaturated Solutions Data

This section presents the KCl and water quantities weighed out in the preparation of the supersaturated solutions used in the control and laser irradiation experiments. The supersaturation is calculated, by use of an expression for the saturation curve of KCl derived from a simulation in OLI Studio, using a KCl solubility of 358.69 g/Kg water at 25 °C as a reference. The calculated solubility values were comparable to data found in literature, confirming the validity of the expression [48].

1.05 Supersaturated solutions

Table B.1: Overview of the KCl and water quantities used to prepare the three different 1.05 supersaturated solutions used in the control and laser irradiation experiments.

Supersaturation at 25 °C	**Weight of KCl (g)**	**Weight of Water (g)**
1.050	26.36316	70.01
1.050	26.36359	70.01
1.050	26.36269	70.03

1.10 Supersaturated solutions

Table B.2: Overview of the KCl and water quantities used to prepare the three different 1.10 supersaturated solutions used in the control and laser irradiation experiments.

Supersaturation at 25 °C	**Weight of KCl (g)**	**Weight of Water (g)**
1.1000	27.61917	70.00
1.010	27.61945	70.02
1.099	27.61819	70.04

B.2. Laser Intensity Calculation

This section presents the calculation for the conversion of the laser Intensity to a laser power which can be measured in the lab by use of a power meter.

Table B.3: Overview of parameters used in the calculations of the laser intensities.

Parameter	**Value**	**Unit**	**Obtained from**
Original laser beam diameter (LD_O)	9	mm	
Focal length convex lens (F_+)	500	mm	
Focal length concave lens (F_-)	75	mm	
Focal length Ratio (FR)	0.15		F_+/F_-
Converged beam diameter (LD_C)	1.35	mm	Focal FR · LD_O
Converged laser beam Area (A_L)	0.01431	cm^2	$\frac{1}{4}\pi D^2$
Laser frequency (f_{laser})	10	Hz	
Laser pulse duration (t_{laser})	$7 \cdot 10^{-9}$	s	

Equation B.1 shows the commonly known equation for the calculation of the laser intensity, where I is the laser Intensity (W/cm^2), E_P the energy per pulse (J), A the laser beam area (cm^2) and t_{laser} the laser pulse duration (s). Equation B.1 is rewritten to Equation B.2 to calculate the energy per pulse and multiplied by the number of pulses per second to obtain a power meter reading which can be measured in the lab. Equations B.1 & B.2 are used in the calculations in Table B.4 to convert the specified laser intensities to power meter readings.

$$I = \frac{E_P}{A_L * t_{laser}} \tag{B.1}$$

$$E_P = I * A_L * S \tag{B.2}$$

Table B.4: Overview of the calculations of the laser intensities.

Laser intensity (MW/cm^2)	**Laser intensity (W/cm^2)**	**E_p(J) Eq B.2**	**Power meter (W) $f_{laser} \cdot E_p$**
10	$10 \cdot 10^6$	$1.0100 \cdot 10^{-3}$	$1.0100 \cdot 10^{-2}$
25	$25 \cdot 10^6$	$2.5040 \cdot 10^{-3}$	$2.5040 \cdot 10^{-2}$
50	$50 \cdot 10^6$	$5.0007 \cdot 10^{-3}$	$5.0007 \cdot 10^{-2}$
70	$70 \cdot 10^6$	$7.0100 \cdot 10^{-3}$	$7.0100 \cdot 10^{-2}$
100	$100 \cdot 10^6$	$10.015 \cdot 10^{-3}$	$10.015 \cdot 10^{-2}$

Values listed in the last column of Table B.4 are used to tune the YAG laser used in these experiments to the desired intensity. For experiments conducted at 532 and 1064 nm the power was measured before the telescopic set-up, since they have no significant interaction with the glass lenses. However, for experiments conducted at 355 nm the power was measured before the last mirror, since it is known that this wavelength is (slightly) absorbed by the glass lenses.

B.3. Control Cooling Experiments - Results

This section presents the results of the control cooling experiments, the average of all the results is also presented in Chapter 4 and served as a reference to the laser irradiation experiments. The volume normalized nucleation probabilities were determined by multiplying the (directly observed) nucleation probability with the ratio of the largest observed volume amongst all measurements (S = 1.05 - 532 - 50 MW/cm^2) and the average volume of a specific measurement.

B.3.1. 1.05 Supersaturated solutions

Table B.5: Results of control cooling experiments of 1.05 supersaturated KCl solution.

Measurement	**Supersaturation**	**Mean velocity (mm/s)**	**Mean volume (μL)**	**Number of droplets**	**Nucleation probability**	**Nucleation probability normalized volume**
1	1.0635 ± 0.0016	2.4013 ± 0.1543	0.9697 ± 0.1276	1448	0.00967 ± 0.00002	0.01590 ± 0.00209
2	1.0480 ± 0.0020	2.4378 ± 0.1558	0.9226 ± 0.1167	1217	0.00986 ± 0.00002	0.01704 ± 0.00216
3	1.0487 ± 0.0021	2.4300 ± 0.1475	0.8974 ± 0.1695	1585	0.00820 ± 0.00002	0.01417 ± 0.00268
Average	1.0534 ± 0.0011	2.4230 ± 0.0881	0.9299 ± 0.0807	1417	0.00924 ± 0.00001	0.01570 ± 0.00134

B.3.2. 1.10 Supersaturated solutions

Table B.6: Results of control cooling experiments of 1.10 supersaturated KCl solution.

Measurement	**Supersaturation**	**Mean velocity (mm/s)**	**Mean volume (μL)**	**Number of droplets**	**Nucleation probability**	**Nucleation probability normalized volume**
1	1.1101 ± 0.0034	2.3975 ± 0.1055	1.0377 ± 0.0951	1465	0.02116 ± 0.00002	0.03251 ± 0.00298
2	1.0987 ± 0.0019	2.3662 ± 0.1554	0.9618 ± 0.2202	1234	0.02991 ± 0.00002	0.04958 ± 0.01135
3	1.1049 ± 0.0032	2.4204 ± 0.2380	1.0273 ± 0.2125	1021	0.02547 ± 0.00003	0.03952 ± 0.00818
Average	1.1046 ± 0.0017	2.3947 ± 0.1011	1.0089 ± 0.1068	1241	0.02551 ± 0.00001	0.04054 ± 0.00477

B.4. Laser Irradiation Experiments - Results

This section presents the results of the laser irradiation experiments performed to study the effects of NPLIN parameters supersaturation, laser Intensity and laser wavelength on the nucleation probability. The results are presented as follows, the different laser wavelengths have been divided in sections, consisting of subsections based on supersaturation. In each subsection a table is presented, displaying the results in order of increasing laser Intensity. The volume normalized nucleation probabilities were determined by multiplying the (directly observed) nucleation probability with the ratio of the largest observed volume amongst all measurements (S = 1.05 - 532 - 50 MW/cm^2) and the average volume of a specific measurement.

B.4.1. 1064 nM

1.05 Supersaturated solutions

Table B.7: Results of laser exposure at 1064 nM of 1.05 supersaturated KCl solution.

Supersaturation	**Laser intensity (MW/cm^2)**	**Mean velocity (mm/s)**	**Number of Pulses per droplet**	**Mean volume (μL)**	**Number of droplets**	**Nucleation probability**	**Nucleation probability normalized volume**
1.0507 ± 0.0035	10	2.4233 ± 0.1371	10.46 ± 0.75	0.9596 ± 0.0916	1409	0.00497 ± 0.00002	0.00825 ± 0.00079
1.0481 ± 0.0013	25	2.2393 ± 0.1354	12.11 ± 1.06	1.2549 ± 0.1574	1053	0.01994 ± 0.00003	0.02534 ± 0.00318
1.0568 ± 0.0044	50	2.3911 ± 0.1671	11.09 ± 1.61	1.0540 ± 0.2736	1391	0.02301 ± 0.00002	0.03480 ± 0.00903
1.0522 ± 0.0018	100	2.3750 ± 0.1582	11.05 ± 1.66	1.0329 ± 0.2855	1360	0.03382 ± 0.00002	0.05221 ± 0.01443

1.10 Supersaturated solutions

Table B.8: Results of laser exposure at 1064 nM of 1.10 supersaturated KCl solution.

Supersaturation	**Laser intensity (MW/cm^2)**	**Mean velocity (mm/s)**	**Number of Pulses per droplet**	**Mean volume (μL)**	**Number of droplets**	**Nucleation probability**	**Nucleation probability normalized volume**
1.1009 ± 0.0018	10	2.5144 ± 0.2244	11.05 ± 3.15	1.1571 ± 0.6096	1475	0.04339 ± 0.00002	0.05979 ± 0.03150
1.1074 ± 0.0041	25	2.4082 ± 0.1409	10.47 ± 1.45	0.9484 ± 0.2567	1491	0.05366 ± 0.00002	0.09020 ± 0.02441
1.1075 ± 0.0017	50	2.3898 ± 0.1266	9.93 ± 1.05	0.8295 ± 0.1757	1006	0.05666 ± 0.00003	0.10891 ± 0.02307
1.0975 ± 0.0015	100	2.4392 ± 0.1676	10.37 ± 1.13	0.9552 ± 0.1739	1550	0.06774 ± 0.00002	0.11307 ± 0.02059

B.4.2. 532 nM

1.05 Supersaturated solutions

Table B.9: Results of laser exposure at 532 nM of 1.05 supersaturated KCl solution.

Supersaturation	**Laser intensity (MW/cm^2)**	**Mean velocity (mm/s)**	**Number of Pulses per droplet**	**Mean volume (μL)**	**Number of droplets**	**Nucleation probability**	**Nucleation probability normalized volume**
1.0498 ± 0.0052	10	2.4051 ± 0.4808	11.88 ± 4.29	1.2211 ± 0.6968	1704	0.00176 ± 0.00001	0.00230 ± 0.00131
1.0586 ± 0.0053	25	2.7414 ± 0.1897	9.56 ± 0.90	1.0294 ± 0.1355	1234	0.01053 ± 0.00002	0.01632 ± 0.00215
1.0414 ± 0.0013	50	2.3848 ± 0.1623	13.91 ± 2.14	1.5944 ± 0.3700	987	0.03141 ± 0.00003	0.03141 ± 0.00729
1.0442 ± 0.0048	100	2.8191 ± 0.3729	9.89 ± 1.45	1.1642 ± 0.1431	1632	0.02941 ± 0.00002	0.04028 ± 0.00495

1.10 Supersaturated solutions

Table B.10: Results of laser exposure at 532 nM of 1.10 supersaturated KCl solution.

Supersaturation	**Laser intensity (MW/cm^2)**	**Mean velocity (mm/s)**	**Number of Pulses per droplet**	**Mean volume (μL)**	**Number of droplets**	**Nucleation probability**	**Nucleation probability normalized volume**
1.1111 ± 0.0084	10	2.4043 ± 0.1884	10.94 ± 1.32	1.0370 ± 0.1966	1298	0.04700 ± 0.00002	0.07226 ± 0.01370
1.1177 ± 0.0066	25	2.4322 ± 0.1365	12.66 ± 1.01	1.4015 ± 0.1415	1044	0.07663 ± 0.00003	0.08718 ± 0.00880
1.0914 ± 0.0024	50	2.3706 ± 0.1283	10.80 ± 0.74	0.9797 ± 0.0871	1166	0.05918 ± 0.00003	0.09631 ± 0.00856
1.0954 ± 0.0036	100	2.4179 ± 0.1706	10.77 ± 1.72	1.0161 ± 0.3030	1264	0.09098 ± 0.00002	0.14276 ± 0.04257

B.4.3. 355 nM

1.05 Supersaturated solutions

Table B.11: Results of laser exposure at 355 nM of 1.05 supersaturated KCl solution.

Supersaturation	**Laser intensity (MW/cm^2)**	**Mean velocity (mm/s)**	**Number of Pulses per droplet**	**Mean volume (μL)**	**Number of droplets**	**Nucleation probability**	**Nucleation probability normalized volume**
1.0618 ± 0.0086	10	2.4859 ± 0.1566	11.79 ± 1.13	1.2809 ± 0.1707	1191	0.00756 ± 0.00002	0.00941 ± 0.00125
1.0448 ± 0.0052	25	2.5060 ± 0.1464	11.81 ± 1.27	1.3031 ± 0.2172	1179	0.01357 ± 0.00002	0.01660 ± 0.00277
1.0549 ± 0.0026	50	2.5148 ± 0.2261	10.09 ± 0.99	0.9650 ± 0.0835	1614	0.01797 ± 0.00002	0.02969 ± 0.00257
1.0368 ± 0.0022	70	2.4178 ± 0.2200	11.68 ± 4.14	1.1930 ± 0.7827	1510	0.02583 ± 0.00002	0.03452 ± 0.02265

1.10 Supersaturated solutions

Table B.12: Results of laser exposure at 355 nM of 1.10 supersaturated KCl solution.

Supersaturation	**Laser intensity (MW/cm^2)**	**Mean velocity (mm/s)**	**Number of Pulses per droplet**	**Mean volume (μL)**	**Number of droplets**	**Nucleation probability**	**Nucleation probability normalized volume**
1.0971 ± 0.0010	10	2.4091 ± 0.1722	11.03 ± 2.76	1.0580 ± 0.5162	1436	0.04427 ± 0.00002	0.06672 ± 0.03255
1.0954 ± 0.0012	25	2.4651 ± 0.1534	10.93 ± 2.99	1.0899 ± 0.5814	1429	0.05108 ± 0.00002	0.07473 ± 0.03986
1.0968 ± 0.0022	50	2.4683 ± 0.1395	11.37 ± 0.83	1.1797 ± 0.1052	1104	0.10960 ± 0.00003	0.14813 ± 0.01321
1.0898 ± 0.0009	70	2.3939 ± 0.1246	10.75 ± 0.68	0.9912 ± 0.0749	1223	0.15863 ± 0.00002	0.25516 ± 0.01928

B.5. Capillary Transmission Spectrum

This section displays the transmission spectrum of the square borosilicate capillaries comparable to the ones used in the cooling and laser irradiation experiments provided by the supplier [128]. It can be seen in the spectrum that the transmission rapidly decays around the 350 nm mark.

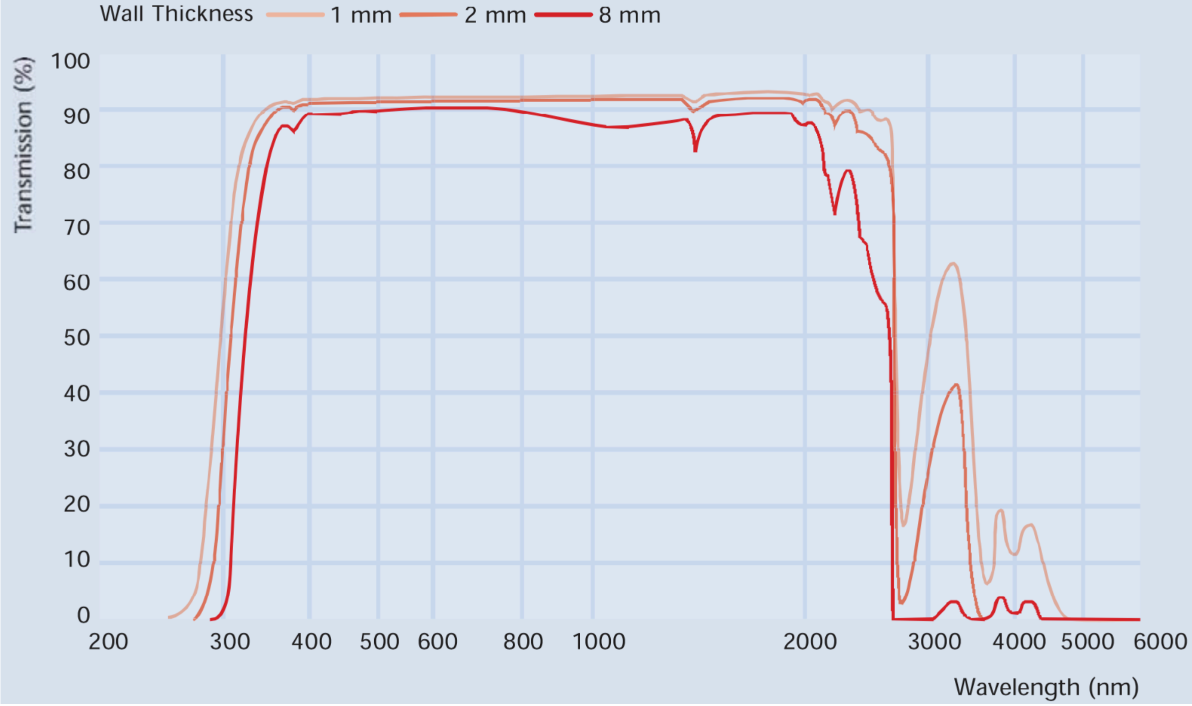

Figure B.1: Transmission spectrum of square borosilicate capillaries with wall thicknesses of 1, 2 and 8 mm [128].

B.6. Matlab - IR Data Analysis Code

This section posts the Matlab code used to analyze the data gathered by the set of IR sensors in the laser exposure zone. The code calculates important NPLIN influencing parameters such as size, volume and velocity. Velocity indirectly affects the number pulses per droplets as well as the detection time. The Matlab code is also available here.

```
clc; close all; clear all;

%Input data
D = readtable('1512-Blank-3-IR','Filetype','text');


V1 = table2array(D(:,1));
Time1 = table2array(D(:,2));
Vminarray1 = table2array(D(:,5));
Vmintime1 = table2array(D(:,6));
V2 = table2array(D(:,7));
Time2 = table2array(D(:,8));
Vmintime2 = table2array(D(:,12));
Vminarray2 = table2array(D(:,11));
Vlin = table2array(D(:,14));

%Adjusted Variables
%The Arduino microcontroller used a micros time counter to log and store
%the time associated with the IR sensor data. However, the Arduino micros
%time counter, resets automatically and randomly after a period of roughly
%70 minutes has ellapsed. The logging programme however will continue to
%store and save data, Thereby creating two datapoints for a single time value.

%Splitting of the needed to be done for proper data visualisation and in
% order to ensure proper functioning of the islocalmin command, correlating
% the correct minima with each other, and not excluding any data points
% which would lead to incorrect droplet counts and volume estimations.

%The so called "splitting point" (point at which the counter resets) needs
%to be found manually and can then be used as a cut off value in the
%variables below.


%Adjusted variables Sensor 1
%First part of the sensor 1 dataset untill the Arduino micros time counter resets
Time1_1 = Time1(1:150083);
V1_1 = V1(1:150083);

%Second part of the sensor 1 dataset after the Arduino micros time counter has
%resetted.
Time1_2 = Time1(150084:end);
V1_2 = V1(150084:end);


%adjusted variables Sensor 2
%First part of the sensor 2 dataset untill the Arduino micros time counter resets
Time2_1 = Time2(1:150083);
V2_1 = V2(1:150083);

%Second part of the sensor 2 dataset after the Arduino micros time counter has
%resetted.
Time2_2 = Time2(150084:end);
V2_2 = V2(150084:end);
```

```
close all; clc;

%part1
Nr_droplets = 1548;
%plot data to visualise it, but divid by 1e6 to go from micro seconds to seconds
%first part of the Data
figure
plot((Time1_1/1e6),V1_1)
title('Voltage data both sensors')
xlabel('time (s)')
ylabel('IR sensor signals (V)')
grid on
hold on
plot((Time2_1/1e6),V2_1)
legend('Vsensor1','Vsensor2');
hold off

%second part of the data
figure
plot((Time1_2/1e6),V1_2)
title('Voltage data both sensors')
xlabel('time (s)')
ylabel('IR sensor signals (V)')
grid on
hold on
```

```
plot((Time2_2/1e6),V2_2)
legend('Vsensor1','Vsensor2');
hold off


%adjusted time variables from microseconds to seconds, to ease further
%processing visualisation.
Time1_1s = Time1_1/1e6;
Time1_2s = Time1_2/1e6;
Time2_1s = Time2_1/1e6;
Time2_2s = Time2_2/1e6;

%Find and evaluate sensor minima
%Islocalmin - Finds and detects minima within a dataset, its search
%criteria can be adjusted to ensure it only detects one absolute minima
%per disturbance (see below).

%Prominence - The depth of the interval, can be adjusted to ensure the
%islocalmin command doesnt detect minima caused by noise in the data.

%Minseperation - The width of the interval, ensures only one minima is
%detected for any given interface causing the Ir sensor values to drop, can
%be adjusted if minima are located closer together or the width of the
%interval is larger than expected.


%Locate sensor1 minima
V1min_1 = islocalmin(V1_1,'MinProminence',0.04,'MinSeparation',0.12,'SamplePoints',Time1_1s);
V1min_2 = islocalmin(V1_2,'MinProminence',0.04,'MinSeparation',0.12,'SamplePoints',Time1_2s);

%Locate sensor2 minima
V2min_1 = islocalmin(V2_1,'MinProminence',0.04,'MinSeparation',0.12,'SamplePoints',Time2_1s);
V2min_2 = islocalmin(V2_2,'MinProminence',0.04,'MinSeparation',0.12,'SamplePoints',Time2_2s);

%Plot and visualize data with detected minima
%First part of both sensor datasets untill the Arduino microstime counter resets
figure
plot(Time1_1s,V1_1,Time1_1s(V1min_1),V1_1(V1min_1),'r*')
title('Plot voltage data and detected minima')
xlabel('Time (s)')
ylabel('Voltage (V)')
hold on
plot(Time2_1s,V2_1,Time2_1s(V2min_1),V2_1(V2min_1),'b*')

%Second part of both sensor datasets after the Arduino micros time counter has
%resetted.
figure
plot(Time1_2s,V1_2,Time1_2s(V1min_2),V1_2(V1min_2),'r*')
title('Plot voltage data and detected minima')
xlabel('Time (s)')
ylabel('Voltage (V)')
hold on
plot(Time2_2s,V2_2,Time2_2s(V2min_2),V2_2(V2min_2),'b*')


%Find the indices/datapoints attached to the minima in the original dataset.
V1min_idx_1 = find(V1min_1);
V1min_idx_2 = find(V1min_2);
V2min_idx_1 = find(V2min_1);
V2min_idx_2 = find(V2min_2);

%Only store the data coresponding to the minima and not all other datapoints
%that are of no use in the further data processing.

%First part of the sensor 1 dataset untill the Arduino micros time counter resets
t1min_1 = Time1_1(V1min_idx_1);
Vt1_1 = V1_1(V1min_idx_1);

%Second part of the sensor 1 dataset after the Arduino micros time counter has
%resetted.
t1min_2 = Time1_2(V1min_idx_2);
Vt1_2 = V1_2(V1min_idx_2);


%adjusted variables Sensor 2
%First part of the sensor 2 dataset untill the Arduino micros time counter resets
t2min_1 = Time2_1(V2min_idx_1);
Vt2_1 = V2_1(V2min_idx_1);

%Second part of the sensor 2 dataset after the Arduino micros time counter has
%resetted.
t2min_2 = Time2_2(V2min_idx_2);
```

```
Vt2_2 = V2_2(V2min_idx_2);



%Filter out (extreme) outliers, want to retain as much as possible of the
%original dataset, but remove any minima that are out of the trend and most
%probably correspond to either sensor misreadings, disturbances or even gas
%bubbles. Thus adjust the sensor threshold value based on the data found
%and values een in the previous data visualisation steps.

%Sensor 1
%First part of the sensor 1 dataset untill the Arduino micros time counter reset
indexdel1_1 = find(Vt1_1>4.25);
t1min_1(indexdel1_1)=[];
Vt1_1(indexdel1_1)=[];

%Second part of the sensor 1 dataset after the Arduino micros time counter has
%resetted.
indexdel1_2 = find(Vt1_2>4.25);
t1min_2(indexdel1_2)=[];
Vt1_2(indexdel1_2)=[];

%Sensor 2
%First part of the sensor 2 dataset untill the Arduino micros time counter resets
indexdel2_1 = find(Vt2_1>1.05);
t2min_1(indexdel2_1)=[];
Vt2_1(indexdel2_1)=[];

%Second part of the sensor 2 dataset after the Arduino micros time counter has
%resetted.
indexdel2_2 = find(Vt2_2>1.05);
t2min_2(indexdel2_2)=[];
Vt2_2(indexdel2_2)=[];


%Filter out air bubbles from the data, use the previously found voltage
%threshold value and previous study has found that velocities over 4 mm are
%due to disturbances in the IR sensors caused by air bubbles.
%The threshold time values can be adjusted later when a better indication of velocities has been
%obtained to further improve data processing.

%Sensor 1
%First part of the sensor 1 dataset untill the Arduino micros time counter reset
for o=2:(length(t1min_1)-2)
    tmiddle1_1 = 0.5*(t1min_1(o)+t1min_1(o+1));
    [d_1,ix1_1] = min(abs(Time1_1-tmiddle1_1));
    hmiddle1_1 = V1_1(ix1_1);
    if hmiddle1_1<4.25
        if (t1min_1(o)-t1min_1(o-1))>1632000           %4mm used as max droplet size
            t1min_1(o) = NaN;
            Vt1_1(o) = NaN;
        end
        if (t1min_1(o+2)-t1min_1(o+1))>1632000
            t1min_1(o+1)=NaN;
            Vt1_1(o+1) = NaN;
        end
    end
end
t1min_1 = t1min_1(~isnan(t1min_1));
Vt1_1 = Vt1_1(~isnan(Vt1_1));


%Second part of the sensor 1 dataset after the Arduino micros time counter has
%resetted.
for oj=2:(length(t1min_2)-2)
    tmiddle1_2 = 0.5*(t1min_2(oj)+t1min_2(oj+1));
    [d_2,ix1_2] = min(abs(Time1_2-tmiddle1_2));
    hmiddle1_2 = V1_2(ix1_2);
    if hmiddle1_2<4.25
        if (t1min_2(oj)-t1min_2(oj-1))>1632000           %4mm used as max droplet size, See if this is correct and works!!!!
            t1min_2(oj) = NaN;
            Vt1_2(oj) = NaN;
        end
        if (t1min_2(oj+2)-t1min_2(oj+1))>1632000
            t1min_2(oj+1)=NaN;
            Vt1_2(oj+1) = NaN;
        end
    end
end
t1min_2 = t1min_2(~isnan(t1min_2));
Vt1_2 = Vt1_2(~isnan(Vt1_2));
```

```
%Sensor 2
%First part of the sensor 2 dataset untill the Arduino micros time counter resets
for p=2:(length(t2min_1)-2)
    tmiddle2_1 = 0.5*(t2min_1(p)+t2min_1(p+1));
    [d_1,ix2_1] = min(abs(Time2_1-tmiddle2_1));
    hmiddle2_1 = V2_1(ix2_1);
    if hmiddle2_1<1.05
        if (t2min_1(p)-t2min_1(p-1))>1632000           %4mm used as max droplet size
            t2min_1(p) = NaN;
            Vt2_1(p) = NaN;
        end
        if (t2min_1(p+2)-t2min_1(p+1))>1632000
            t2min_1(p+1)=NaN;
            Vt2_1(p+1) = NaN;
        end
    end
end
t2min_1 = t2min_1(~isnan(t2min_1));
Vt2_1 = Vt2_1(~isnan(Vt2_1));


%Second part of the sensor 2 dataset after the Arduino micros time counter has
%resetted.
for pj=2:(length(t2min_2)-2)
    tmiddle2_2 = 0.5*(t2min_2(pj)+t2min_2(pj+1));
    [d_2,ix2_2] = min(abs(Time2_2-tmiddle2_2));
    hmiddle2_2 = V2_2(ix2_2);
    if hmiddle2_2<1.05
        if (t2min_2(pj)-t2min_2(pj-1))>1632000           %4mm used as max droplet size
            t2min_2(pj) = NaN;
            Vt2_2(pj) = NaN;
        end
        if (t2min_2(pj+2)-t2min_2(pj+1))>1632000
            t2min_2(pj+1)=NaN;
            Vt2_2(pj+1) = NaN;
        end
    end
end
t2min_2 = t2min_2(~isnan(t2min_2));
Vt2_2 = Vt2_2(~isnan(Vt2_2));



%Filter out data that is only detected by one sensor, previous study has
%shown that droplet sizes larger than 8mm are found the be caused by
%mismatches in the detection of sensors and thus need to be removed.

%Filter out data that is only detected by 1 sensor in the first part of the
%dataset before the micros counter resets
m = 1;
while (m <= length(t2min_1))
    if (t2min_1(m)-t1min_1(m))>6900000
        t1min_1(m)=[];
        Vt1_1(m)=[];
    elseif (t2min_1(m)-t1min_1(m))<0
        t2min_1(m)=[];
        Vt2_1(m)=[];
    else
        m=m+1;
    end
end

%Filter out data that is only detected by 1 sensor in the second part of
%the dataset after the micros countered has been resetted
n = 1;
while (n <= length(t2min_2))
    if (t2min_2(n)-t1min_2(n))>6900000
        t1min_2(n)=[];
        Vt1_2(n)=[];
    elseif (t2min_2(n)-t1min_2(n))<0
        t2min_2(n)=[];
        Vt2_2(n)=[];
    else
        n=n+1;
    end
end


%Resize datasets to ensure they are the same size, due to the start and
%stop times of experiments, droplets have sometime passed the first and not
%yet the second sensor or vice versa allready passed the first sensor
```

```
%before starting the measurement and appear in the dataset of the second
%sensor. These points cause mismatches in the detected minima and should
%therefore be removed.

%Ensure both sensor datasets are the same length in the first part of the
%dataset before the micros counter resets
N_2_1 = length(t2min_1)+1;
t1min_1(N_2_1:end) = [];
Vt1_1(N_2_1:end) = [];
N_1_1 = length(t1min_1)+1;
t2min_1(N_1_1:end) = [];
Vt2_1(N_1_1:end) = [];

%Ensure both sensor datasets are the same length in the second part of
%the dataset after the micros countered has been resetted
N_2_2 = length(t2min_2)+1;
t1min_2(N_2_2:end) = [];
Vt1_2(N_2_2:end) = [];
N_1_2 = length(t1min_2)+1;
t2min_2(N_1_2:end) = [];
Vt2_2(N_1_2:end) = [];



%Plot and visualize data with filtered minima
%First part of both sensor datasets untill the Arduino microstime counter resets
figure
plot((Time1_1/1e6),V1_1)
title('Sensor minima filtered')
xlabel('time (s)')
ylabel('IR sensor signals (V)')
grid on
hold on
plot((Time2_1/1e6),V2_1)
plot((t1min_1/1e6),Vt1_1, 'marker', 'x', 'linestyle' , 'none', 'Color', 'red');
plot((t2min_1/1e6),Vt2_1, 'marker', 'x', 'linestyle' , 'none', 'Color', 'blue');
legend('Vsensor1','Vsensor2');
hold off

%Second part of both sensor datasets after the Arduino micros time counter has
%resetted.
figure
plot((Time1_2/1e6),V1_2)
title('Sensor minima filtered')
xlabel('time (s)')
ylabel('IR sensor signals (V)')
grid on
hold on
plot((Time2_2/1e6),V2_2)
plot((t1min_2/1e6),Vt1_2, 'marker', 'x', 'linestyle' , 'none', 'Color', 'red');
plot((t2min_2/1e6),Vt2_2, 'marker', 'x', 'linestyle' , 'none', 'Color', 'blue');
legend('Vsensor1','Vsensor2');
hold off

%Determine time differences between minima detection and calculate velocity.
%First part of both sensor datasets untill the Arduino microstime counter resets
dt_1 = (t2min_1-t1min_1)./1e6;      %Calculate time period between peak detection sensor 1 and 2
v_1=8./dt_1;                        %Calculate velocity from the known distance between sensors and above found time period

%Second part of both sensor datasets after the Arduino micros time counter has
%resetted.
dt_2 = (t2min_2-t1min_2)./1e6;      %Calculate time period between peak detection sensor 1 and 2
v_2=8./dt_2;                        %Calculate velocity from the known distance between sensors and above found time period


%Remove velocities above 4 mm/s and below 1.5 mm/s, since previous study
%have shown these to be caused by either disturbances or mismatches in
%minima detection still present in the dataset.
%First part of both sensor datasets untill the Arduino microstime counter resets
t2minb_1 = t2min_1;
vdelhigh_1 = find(v_1>4);           %Remove velocities above 4 mm/s
v_1(vdelhigh_1) = [];
t2minb_1(vdelhigh_1) = [];
vdellow_1 = find(v_1<1.5);          %Remove velocities below 1.5 mm/s
v_1(vdellow_1) = [];
t2minb_1(vdellow_1) = [];


%Plot calculated and filtered velocities from the first part of the dataset
figure
plot(t2minb_1./1e6,v_1)
title('Linear velocity first part')
```

```
xlabel('time (s)')
ylabel('Droplet velocity (mm/s)')

v_av_1 = mean(v_1);                 %Calculate mean velocity
v_var_1 = var(v_1);                 %Calculate variance velocity

%Second part of both sensor datasets after the Arduino micros time counter has
%resetted.
t2minb_2 = t2min_2;
vdelhigh_2 = find(v_2>4);
v_2(vdelhigh_2) = [];               %Remove velocities above 4 mm/s
t2minb_2(vdelhigh_2) = [];
vdellow_2 = find(v_2<1.5);          %Remove velocities below 1.5 mm/s
v_2(vdellow_2) = [];
t2minb_2(vdellow_2) = [];


%Plot calculated and filtered velocities from the second part of the dataset
figure
plot(t2minb_2./1e6,v_2)
title('Linear velocity second part')
xlabel('time (s)')
ylabel('Droplet velocity (mm/s)')

v_av_2 = mean(v_2);                 %Calculate mean velocity
v_var_2 = var(v_2);                 %Calculate variance velocity


%Combine velocity data of both the first and the second part, in order to
%calculate total mean velocity as well as to use to calculate the total
%size and thus volume distribution.
vt = [v_1; v_2];
vt = vt(:)';
v = transpose(vt);
v_av = mean(v);                     %Calculate mean velocity
v_var = var(v);                     %Calculate variance velocity
v_std = std(v);                     %Calculate standard deviation



%Determine time differences between minima detection for further size
%calculations.
%First part of both sensor datasets untill the Arduino microstime counter resets
dt1_1 = zeros((length(Vt1_1)-1),1);
for i=1:(length(Vt1_1)-1)
    dt1_1(i)=t1min_1(i+1)-t1min_1(i);
end

dt2_1= zeros((length(Vt2_1)-1),1);
for j=1:(length(Vt2_1)-1)
    dt2_1(j) = t2min_1(j+1) - t2min_1(j);
end

%Second part of both sensor datasets after the Arduino micros time counter has
%resetted.
dt1_2 = zeros((length(Vt1_2)-1),1);
for i=1:(length(Vt1_2)-1)
    dt1_2(i)=t1min_2(i+1)-t1min_2(i);
end

dt2_2= zeros((length(Vt2_2)-1),1);
for j=1:(length(Vt2_2)-1)
    dt2_2(j) = t2min_2(j+1) - t2min_2(j);
end


%Calculate droplet sizes
%First part of both sensor datasets untill the Arduino microstime counter resets
ds1_1 = dt1_1 ./1e6 .* v_av_1;      %Calculate sizes between detected minima sensor 1
ds2_1 = dt2_1 ./1e6 .* v_av_1;      %Calculate sizes between detected minima sensor 2
nbins_1 = 100;
edges_1 = linspace(0,30,201);
edges2_1 = linspace(0,4,100);

%Second part of both sensor datasets after the Arduino micros time counter has
%resetted.
ds1_2 = dt1_2 ./1e6 .* v_av_2;      %Calculate sizes between detected minima sensor 1
ds2_2 = dt2_2 ./1e6 .* v_av_2;      %Calculate sizes between detected minima sensor 2
nbins_2 = 100;
edges_2 = linspace(0,30,201);
edges2_2 = linspace(0,4,100);
```

```
%Combine datasets above to yield the total size dataset and visualize the
%distributions below.
ds1t = [ds1_1; ds1_2];
ds1t = ds1t(:)';
ds1 = transpose(ds1t);              %Total size dataset determined by sensor 1
ds2t = [ds2_1; ds2_2];
ds2t = ds2t(:)';
ds2 = transpose(ds2t);              %Total size dataset determined by sensor 2
nbins = 100;
edges = linspace(0,30,201);
edges2 = linspace(0,4,100);

%Visualize total size dataset sensor 1
figure
histogram(ds1,edges)
title('Size distribution')
xlabel('size (mm)')
ylabel('count')

figure
histogram(ds1,edges2)
title('Size distribution droplets')
xlabel('size (mm)')
ylabel('count')

%Visualize total size dataset sensor 2
figure
histogram(ds2,edges)
title('Size distribution')
xlabel('size (mm)')
ylabel('count')

figure
histogram(ds2,edges2)
title('Size distribution droplets')
xlabel('size (mm)')
ylabel('count')


%Calculate mean overall length, as stated before the previous study found
%that size larger than 4 mm are caused by disturbances in the data
%detection caused by either the continious phase, air bubbles or sensor
%errors. These lengths will therefore be removed by finding the indicices
%coressponding to lengths smaller than 4 mm and only storing these in a
%separete array Ld used for the mean size calculation.
dropletidx = find(ds1<4);
Ld = ds1(dropletidx);
Ld_av = mean(Ld);                   %Calculate mean velocity
Ld_var = var(Ld);                   %Calculate variance velocity
Ld_std = std(Ld);                   %Calculate standard deviation


%Visualize droplet size evolution during experiment
figure
plot(Ld)
title('Droplet size evolution during experiment')
ylabel('Droplet size (mm)')
grid on

%Sort droplet sizes, such that the previously mentioned extremely larger
%droplets caused by sensor disturbances are excluded from the dataset.

Ldsorted = sort(ds1);
Ldn = Ldsorted(1:Nr_droplets);
Ldnr_av = mean(Ldn);
Ldnr_var = var(Ldn);
Ldn_std = std(Ldn);

%Visualize the sorted size distribution as the overall size distribution
%for the measurement.
figure
histogram(Ldn,edges2)
title('Size distribution droplets sensor 1')
xlabel('size (mm)')
ylabel('count')

%Volume calculations
width = 0.9;                        %Obtained from the known dimensions of the capillaries used in the experiments
heigth = 0.9;                       %Obtained from the known dimensions of the capillaries used in the experiments
Volume = width*heigth*Ld;           %Use known formula for volume combined with droplet sizes to calculate droplet volumes
Volume_av = mean(Volume);
```

```
Volume_var = var(Volume);
Volume_std = std(Volume);




%Comments
%Problems encountered previously during dataprocessing were:
%1. Nonfinite numbers (NaN) stored in the dataset, inhibiting data plotting and
%minima detection.
%2. Duplicate indices, inhibtting the working of islocalmin.
%3. Extremely high sensor value detections due to disruptions.


%1. use the below stated commands to detect any non finite numbers present
%in the dataset, ri will supply the index of the non finite number(s) and
%ci will give the number of non finite numbers in the dataset. Manually
%remove them from the dataset.
%[ri,ci] = find(~isfinite(Time1_1));

%2. Use either two of the below stated methods to detect duplicate indices.
%The second method (2.2) works most easily where it first tracks down all unique
%points, returns a unique vector and the indices. and by plugging this
%inthe the setdiff it;ll return you a vector with the indices of the
%duplicate values (last occurence) in the original vector so you can manually remove it.
%2.1
% TF1 = isfinite(Time1);
% duplicate_indices1 = setdiff( 1:numel(Time1), TF1 );
%
% %2.2
% [v, w] = unique(Time1_1,'last', 'legacy');
% duplicate_indices = setdiff( 1:numel(Time1_1), w );

%3 Sometimes, the dataset shows a sudden extremely larger peak (3 to 6
%orders of magnitude higher than standard data) due to disruptions use the
%max command in order to detect its index and manually remove it.
%[MaxV, maxi] = max(V2);
```

Published with MATLAB® R2020a

B.7. Matlab - Temperature Data Analysis Code

This section posts the Matlab code used to analyze the data gathered by the ambient temperature sensor. The code calculates the mean ambient temperature as well as converting the gathered temperature data, by use of an expression for the saturation curve of KCl derived from a simulation in OLI Studio, to a mean supersaturation. The Matlab code is also available here

```
clc; close all; clear all;

D = readtable('measurement_1_05_blank3','Filetype','text');

V1 = table2array(D(:,2));
T = V1;


%remove NaN from dataset
ind = find(isnan(T));
T(ind) = [];
```

```
close all; clc;


%temperature data analysis
T_av = mean(T);
T_std = std(T);
T_var = var(T);

%Use the following values to detect if the sensor observed an abnormal Temperature (usually abnormally high --> Order 10^6) and remove if needed.
T_max = max(T);
T_min = min(T);

%Conversion of temperature to supersaturation data
%solubilitylim calculations
A = 2.989166216; %(Simulation yielded a value of 0.04 Mol KCl / L H20, this was converted to g KCl / Kg H20)
B = 283.9707905; %(Simulation yielded a value of 3.8 Mol KCl / L H20, this was converted to g KCl / Kg H20)
Solubilitylimtot  = A * T + B;

%Dissolved Salt
DS = 26.36316; % S = 1.05, Salt contents in grams!
%DS = 27.61917;  %S = 1.10, Salt contents in grams!

%Water Weight of the solution
DW = (70.01/1000); % S = 1.05, water weight in grams!
%DW = (70.00/1000); %S = 1.10, water weight in grams!

%KCl solubilitylim in the solution based on the weight of water in the solution
Solubilitylim = DW * Solubilitylimtot;

%Supersaturation calculation
Supersat = DS./Solubilitylim;
Supersat_av = mean(Supersat);
Supersat_std = std(Supersat);
Supersat_var = var(Supersat);
```

Published with MATLAB® R2020a

C

Appendix C

This section presents the outcomes of analyzing the experimental data presented and discussed in Chapter 4 in light of both the Classical Nucleation Theory as well as the Dielectric Polarization model.

C.1. Classical Nucleation Theory (CNT)

In this section the calculated nucleation rates for all of the separate cooling experiments are presented as well as the averages which were displayed in Chapter 5.

C.1.1. Control Cooling Experiments - Nucleation rates

1.05 supersaturated solutions

Table C.1: Nucleation rate (*J*) values calculated from the nucleation probabilities determined in the NPLIN experiments listed in Appendix B.4 for 1.05 supersaturated solutions.

Measurement	***J*** **(μL^{-1} h^{-1})**
1	0.5413 ± 0.0793
2	0.5891 ± 0.0835
3	0.5018 ± 0.0966
Average	0.5441 ± 0.0507

1.10 supersaturated solutions

Table C.2: Nucleation rate (*J*) values calculated from the nucleation probabilities determined in the NPLIN experiments listed in Appendix B.4 for 1.10 supersaturated solutions.

Measurement	***J*** **(μL^{-1} h^{-1})**
1	1.1118 ± 0.1130
2	1.6810 ± 0.4004
3	1.3674 ± 0.3132
Average	1.3867 ± 0.1736

C.1.2. Interfacial Tension - Calculation Parameters

1.10 supersaturated solutions

Table C.3: Parameters used in the determination of the interfacial tension between the nucleus and the solution in 5.1.

Parameter	**Value**	**Unit**
v	$6.2397218 \cdot 10^{-29}$	m^3
k_B	$1.38 \cdot 10^{-23}$	$m^2 \cdot kg \cdot s^{-2} \cdot K^{-1}$
T	25	°C

C.2. Dielectric Polarization (DP) Model

The following sections present the lability parameter estimations obtained by fitting the data from the laser irradiation experiments to the Dielectric Polarization model. First, the estimations obtained by use of the Matlab curve fitting toolbox are presented, followed by parameters describing the quality of the fitting. Second, the estimations of the lability parameter obtained by averaging the lability parameter determined at each individual point are presented. For each section, the value of the parameter directly determined from the data (m), the value corrected for the bulk volume employed in bulk studies (m_V) and the value corrected for both the bulk volume as well as the observed laser intensity threshold (m_{VI}) are presented.

C.2.1. Lability parameters estimation - Matlab curve fitting toolbox

The following sections present estimations of the lability parameter obtained by use of the Matlab curve fitting toolbox. First the estimations of the 1.05 supersaturated solutions are presented for each wavelength under all conditions, followed by the the estimations for the 1.10 supersaturated solutions.

1.05 supersaturated solutions

Table C.4: Lability parameter (m) values, lability parameter (m_V) values corrected for the bulk volume used in literature [64] and lability parameter (m_{VI}) values corrected for both the bulk volume and laser intensity literature encountered in the literature [64] for S = 1.05 determined from fitting the data from the NPLIN experiments listed in Appendix B.4 to the expression in Equation 5.7 by use of the Matlab curve fitting toolbox.

Lability parameter (cm^2/MW)	**1064 nm**	**532 nm**	**355 nm**
m	0.00060 ± 0.00022	0.00047 ± 0.00019	0.00055 ± 0.00014
m_V	0.1311 ± 0.0524	0.1023 ± 0.0464	0.1212 ± 0.0409
m_{VI}	0.1427 ± 0.0759	0.1120 ± 0.0689	0.1374 ± 0.0649

1.10 supersaturated solutions

Table C.5: Lability parameter (m) values, lability parameter (m_V) values corrected for the bulk volume used in literature [64] and lability parameter (m_{VI}) values corrected for both the bulk volume and laser intensity literature encountered in the literature [64] for S = 1.10 determined from fitting the data from the NPLIN experiments listed in Appendix B.4 to the expression in Equation 5.7 by use of the Matlab curve fitting toolbox.

Lability parameter (cm^2/MW)	**1064 nm**	**532 nm**	**355 nm**
m	0.00162 ± 0.00151	0.00182 ± 0.00137	0.00381 ± 0.00120
m_V	0.3550 ± 0.3400	0.3997 ± 0.3054	0.8364 ± 0.3329
m_{VI}	0.3747 ± 0.4255	0.4245 ± 0.3987	0.9488 ± 0.4409

C.2.2. Lability parameters estimation - Matlab curve fitting toolbox - Quality of the fit

In this section the parameters used to describe the quality of the data fit for both the value directly determined from the data (m) as well as the volume and laser intensity threshold correct estimations are presented (m_{VI}).

1.05 supersaturated solutions

Table C.6: The following parameters to describe the quality of the estimation obtained by use of the Matlab curve fitting toolbox for each wavelength are presented: the coefficient of determination (R^2), sum of squared estimate of errors (SSE) and mean squared error (MSE).

Lability parameter (cm^2/MW)	**1064 nm**			**532 nm**			**355 nm**		
	R^2	**SSE**	**MSE**	**R^2**	**SSE**	**MSE**	**R^2**	**SSE**	**MSE**
m	0.8238	$1.78\cdot10^{-4}$	0.0077	0.8506	$1.26\cdot10^{-4}$	0.0065	0.8977	$4.12\cdot10^{-5}$	0.0037
m_{VI}	0.6819	$3.22\cdot10^{-4}$	0.0104	0.7824	$1.83\cdot10^{-4}$	0.0078	0.7194	$1.13\cdot10^{-4}$	0.0061

1.10 supersaturated solutions

Table C.7: The following parameters to describe the quality of the estimation obtained by use of the Matlab curve fitting toolbox for each wavelength are presented: the coefficient of determination (R^2), sum of squared estimate of errors (SSE) and mean squared error (MSE).

Lability parameter (cm^2/MW)	**1064 nm**			**532 nm**			**355 nm**		
	R^2	**SSE**	**MSE**	**R^2**	**SSE**	**MSE**	**R^2**	**SSE**	**MSE**
m	-2.8272	0.0068	0.0475	-0.9491	0.0054	0.0425	0.9037	0.0022	0.0271
m_{VI}	-4.0572	0.0089	0.0546	-1.7797	0.0077	0.0507	0.8509	0.0034	0.0337

C.2.3. Lability parameters estimation - Averaged results

The following sections present the lability parameter estimations obtained by averaging the lability parameter determined for each wavelength at each individual laser intensity.

1.05 supersaturated solutions

Table C.8: Lability parameter (m) values, lability parameter (m_V) values corrected for the bulk volume used in literature [64] and lability parameter (m_{VI}) values corrected for both the bulk volume and laser intensity literature encountered in the literature [64] for S = 1.05 determined by inverting the expression in Equation 5.7 and calculating the average of the values found.

Lability parameter (cm^2/MW)	**1064 nm**	**532 nm**	**355 nm**
m	0.00049 ± 0.00018	0.00038 ± 0.00027	0.00049 ± 0.00012
m_V	0.1564 ± 0.0680	0.1061 ± 0.0795	0.1442 ± 0.0431
m_{VI}	0.2205 ± 0.1494	0.1385 ± 0.1778	0.2200 ± 0.0828

1.10 supersaturated solutions

Table C.9: Lability parameter (m) values, lability parameter (m_V) values corrected for the bulk volume used in literature [64] and lability parameter (m_{VI}) values corrected for both the bulk volume and laser intensity literature encountered in the literature [64] for S = 1.10 determined by inverting the expression in Equation 5.7 and calculating the average of the values found.

Lability parameter (cm^2/MW)	**1064 nm**	**532 nm**	**355 nm**
m	0.00220 ± 0.00001	0.00255 ± 0.00002	0.00294 ± 0.00001
m_V	0.7501 ± 0.2610	0.7987 ± 0.1120	0.9620 ± 0.2895
m_{VI}	1.2773 ± 0.5712	1.3920 ± 0.2392	1.5626 ± 0.6145